COMPUTER SIMULATIONS OF AMORPHOUS SEMICONDUCTORS

Printed by:

UNIVERSAL PRESS - SCIENCE PUBLISHERS
Veenendaal

ISBN: 90-393-3207-X

COMPUTER SIMULATIONS OF AMORPHOUS SEMICONDUCTORS

COMPUTER SIMULATIES VAN
AMORFE HALFGELEIDERS

(met een samenvatting in het Nederlands)

PROEFSCHRIFT

TER VERKRIJGING VAN DE GRAAD VAN DOCTOR AAN DE UNIVERSITEIT UTRECHT OP GEZAG VAN DE RECTOR MAGNIFICUS, PROF. DR. W.H. GISPEN, INGEVOLGE HET BESLUIT VAN HET COLLEGE VOOR PROMOTIES IN HET OPENBAAR TE VERDEDIGEN OP MAANDAG 2 DECEMBER 2002 DES MIDDAGS TE 12:45 UUR

DOOR

RICHARD LEVINUS CHRISTOPHER VINK

GEBOREN OP 13 JANUARI 1975, TE PORTCHESTER

Promotor: Prof. Dr. Ir. W. Lourens

Co-promotor: Dr. G.T. Barkema

Faculteit Natuur- en Sterrenkunde
Universiteit Utrecht

Contents

Chapter 1

Introduction and Motivation

The subject of this thesis is the class of materials known as disordered solids. These solids are also referred to as non-crystalline solids, or amorphous solids or glasses. What these materials have in common is that their structure is not crystalline on any significant scale. The aim of this thesis is to provide insight into the atomic structure of disordered solids via computer simulation. Simply put, we try to find out where the atoms are located with respect to each other. For these materials, experimental techniques alone are not sufficient to determine the structure. As a result, computer simulations are often used.

There is considerable confusion in the literature regarding the terms disordered, amorphous or glassy. We therefore begin by providing some definitions. Next, we discuss some of the physical properties of disordered materials. As it turns out, these properties make disordered solids ideal candidates for many applications. We then move on to discuss a number of general experimental techniques frequently used to probe the atomic structure of materials. More importantly, we show that these techniques are only moderately successful in the case of disordered materials. Finally, we point out that computer simulations can be a powerful tool in unraveling the structure of amorphous materials.

1.1 Definitions

A disordered material can be defined as one which does not exhibit the long-range translational order or periodicity characteristic of crystals, see Figure 1.1. Within this definition, such materials could be either solid or liquid, and this distinction is one of timescale. We consider here only solids: a material is considered a solid when it is rigid; i.e. it does not flow when subjected to moderate forces. A common criterion for rigidity is when the shear viscosity exceeds $\eta_s = 10^{13.6}$ N s m^{-2} [1].

The disorder exhibited by the network shown in the lower frame of Figure 1.1

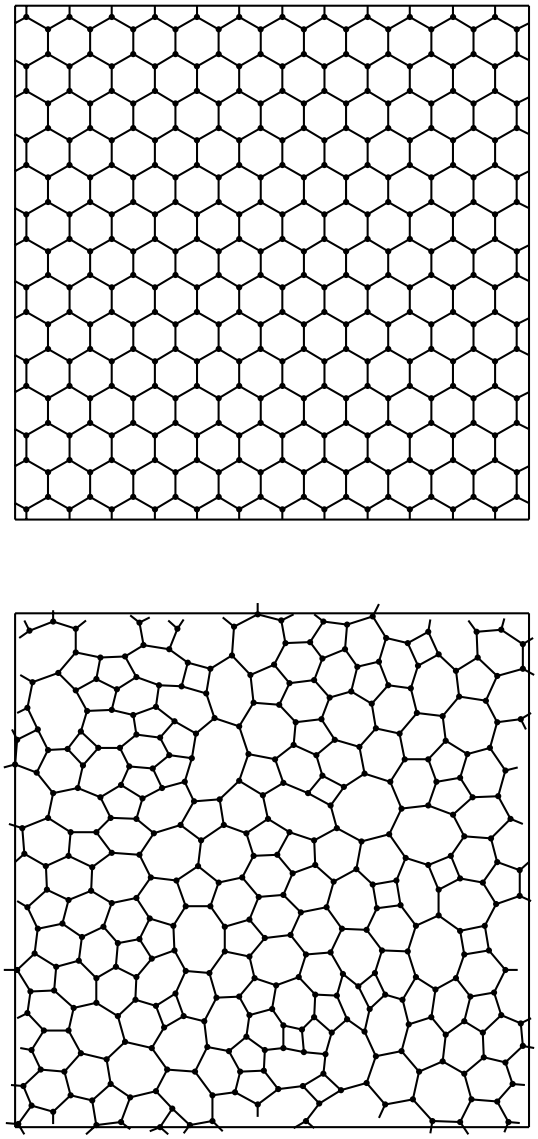

Figure 1.1: Schematic diagrams of 2D atomic structures. Atoms are represented by dots, bonds between atoms by lines. Each atom is three-fold coordinated. The top frame shows a hexagonal crystal structure, the bottom frame an amorphous structure.

is called topological or geometric disorder; this type of disorder is characterized by the absence of translational periodicity. Other types of disorder also exist, for example, spin or magnetic disorder. In this case the underlying crystalline structure is preserved, but each atom possesses a magnetic moment with random orientation. In this thesis, we concern ourselves with topological disorder only. Moreover, we focus on a special class of materials with topological disorder called the *network forming materials*. In this case the structure is determined by the set of bonds between the particles and to a lesser extend by their lengths and orientations.

A special subset of disordered materials are the glasses. A glass is a disordered material that exhibits a glass transition. The glass transition is marked by a change in slope of some extensive thermodynamic quantity (for example volume or entropy) as a function of temperature. Thus, by definition, all glasses are disordered, but not all disordered solids are necessarily glassy. An example of a glassy material is vitreous silica, see Figure 1.2.

1.2 Preparation, properties and applications

Disordered materials have interesting properties not always seen in their crystalline counterparts. In this section we discuss some of these properties. We also mention a number of technological applications and we briefly explain how disordered materials are prepared experimentally.

1.2.1 Melt-quenching

The oldest method of producing an amorphous solid is to cool the molten form of the material sufficiently quickly. This process is called melt-quenching. Amorphous materials produced in this way are often called glasses because many such materials show a glass transition, though not all. This naming convention has been the source of confusion for many years.

When a liquid is cooled, either a crystal will form or an amorphous solid. The distinguishing feature of producing amorphous materials is that the amorphous solid is formed by the continuous hardening (increase in viscosity) of the melt as a whole. An essential criterion for producing amorphous materials is therefore that the cooling process be fast enough to preclude crystal growth [1]. The crystalline phase is thermodynamically more stable and will dominate if allowed to take place. The cooling rate is a critical factor in the production of amorphous solids and has been intensely studied [2].

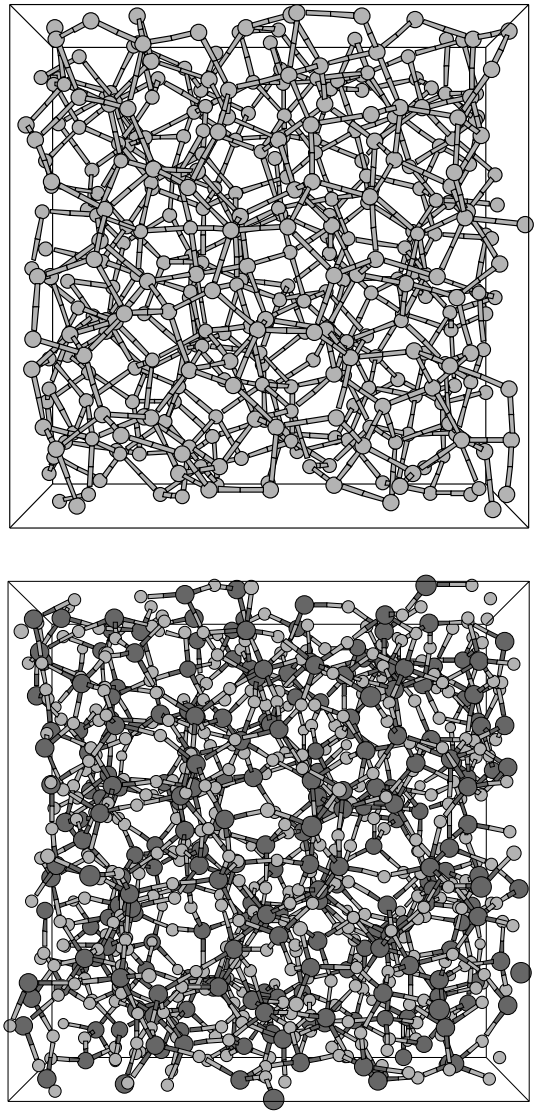

Figure 1.2: Structure of amorphous silicon (top) and vitreous silica (bottom). In amorphous silicon, each silicon atom is bonded to four other silicon atoms with preferred bond lengths and bond angles of 2.35 Å and 109.47 degrees, respectively. In vitreous silica, each silicon atom is bonded to four oxygen atoms and each oxygen atom to two silicon atoms. In both materials, long range order is absent.

1.2.2 Short range order

While amorphous materials do not show the regular, periodic structure of crystals, they are by no means random. In many cases, the structure is governed by strict rules, especially on small length scales. For example, amorphous silicon (see Figure 1.2) consists mostly of four-fold coordinated silicon atoms and the Si-Si bond length and the Si-Si-Si bond angle are close to the crystalline values of 2.35 Å and 109.47 degrees, respectively.

The presence of short-range order is best illustrated with the radial distribution function (RDF). The RDF $g(r)$ is the local number density of atoms at a distance r from a reference atom, averaged with respect to the choice of this atom. In Figure 1.3 we show the RDF of amorphous and crystalline silicon. The RDF of the crystal consists of a series of sharp peaks located at the first-neighbor distance, the second-neighbor distance, and so forth. In contrast, for amorphous silicon, the characteristic features are a number of peaks that become broader and less distinct with increasing r. The position of the first peak is an estimate for the average first-neighbor distance r_1, the position of the second peak an estimate for the average second-nearest-neighbor distance r_2 and so forth. Moreover, these estimates can also be used to estimate the mean Si-Si-Si bond angle:

$$\theta = 2 \arcsin\left(\frac{r_2}{2r_1}\right), \tag{1.1}$$

and from the width of the first- and second-neighbor peaks, the variation in the bond angle can be estimated (under the assumption that there are no correlations between bond length variations in neighboring bonds). At larger distances, the RDF tends to a constant value, which indicates disorder.

In retrospect, amorphous materials are not random but contain some degree of short-range order. In contrast to crystalline materials, long-range order is absent. The absence of long-range order in amorphous materials turns out to have dramatic effects on their vibrational, thermal and electronic properties.

1.2.3 Vibrational properties

Atomic vibrations in a solid have a profound effect on its properties. For example, heat is transported via atomic vibrations and the specific heat of a material is determined mostly by the spectrum of allowed vibrational modes. Furthermore, under certain conditions, electro-magnetic radiation can interact with atomic vibrations (for example in Raman scattering), thereby directly determining the optical properties of the material. In crystals, vibrational modes can be classified in terms of the wavevector because of lattice periodicity [5]. This gives rise to a number of dispersion relations which describe the dependence of the vibrational frequency on the

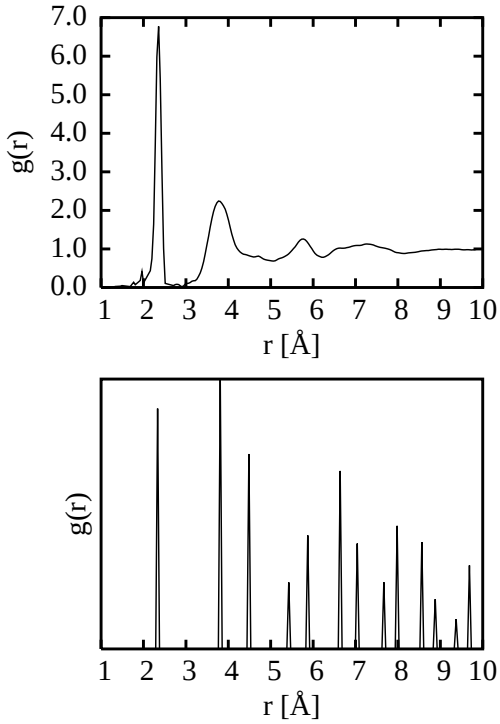

Figure 1.3: Radial distribution function $g(r)$ for amorphous silicon (top) and crystalline silicon (bottom). The RDF for amorphous silicon was obtained experimentally via x-ray diffraction by Laaziri *et al.* in 1999 [3, 4]. The RDF for crystalline silicon was obtained from a computer generated crystal structure; distances are in Å.

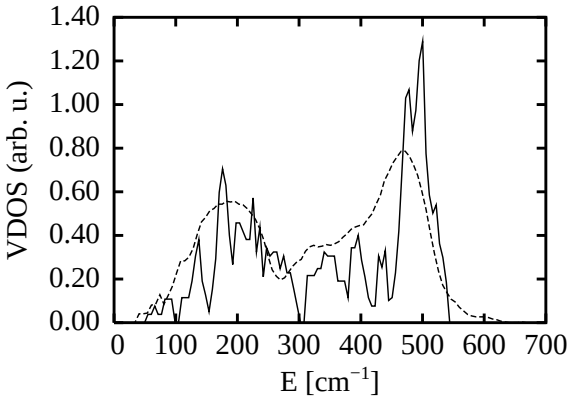

Figure 1.4: Vibrational density of states for crystalline silicon (solid line) and amorphous silicon (dashed line). These curves were obtained from two computer generated structures containing 1000 atoms. We used the Stillinger-Weber potential [6] to describe the atomic interactions. The frequency is given in inverse cm and the VDOS is area normalized.

wavevector. For amorphous solids this classification is not possible [1]. Vibrations in this case are usually described in terms of the vibrational density of states $\rho(\omega)$ or VDOS. The quantity $\rho(\omega)d\omega$ equals the number of states with frequencies between ω and $\omega + d\omega$.

The VDOS of a crystal exhibits Van Hove singularities [5], which are discontinuities in the slope of $\rho(\omega)$, see Figure 1.4. In the same figure, we also show the VDOS of an amorphous solid. It can be seen that the curves are similar. The features unique to the VDOS of the crystal, namely the Van Hove singularities (which result from periodicity) are smeared out in the amorphous case. The correspondence of the peaks however is very close, although they are broadened in the amorphous case. This suggests that short-range order (which is the same in both the crystalline and the amorphous form) determines the vibrational properties [1]. In Chapter 6 we explicitly show that short-range order directly influences the shape of the VDOS. In other words, the VDOS can be used to probe the structure of an amorphous material in experiments.

1.2.4 Electronic properties

Theory for the electronic properties of crystals is greatly simplified by the lattice periodicity of such systems. In this case, the electron states can be written as Bloch waves which extend through the entire crystal [5]. The interaction between the electrons and the atomic cores situated at each lattice site gives rise to a number of band

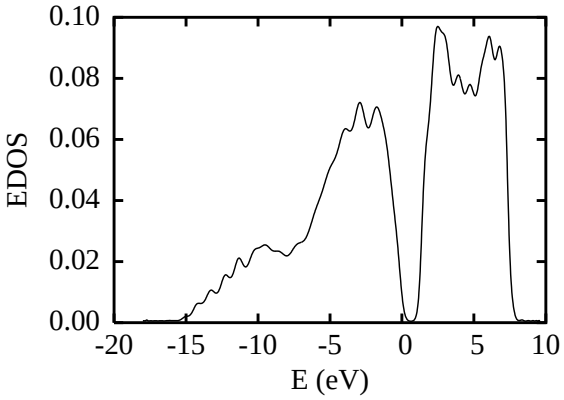

Figure 1.5: Electronic density of states for amorphous silicon. Note the presence of the band gap at $E = 0.60$ eV. This EDOS was obtained from a computer generated amorphous structure containing 10,000 silicon atoms. The structure was generated by us [7], the EDOS was calculated by David Drabold [8].

gaps. The band gap structure is important because it determines whether the crystal is a conductor or an insulator. In amorphous materials the electron states cannot be written as Bloch waves because periodicity is absent [1]. Analogous to lattice vibrations, a valid quantity to describe the electronic properties in this case is the electronic density of states (EDOS). In Figure 1.5 we show the EDOS of amorphous silicon. Note the presence of a band gap at approximately $E = 0.60$ eV which is characteristic of a semiconductor. The EDOS shown in Figure 1.5 was obtained from a computer-generated structure containing 10,000 silicon atoms [7]. This structure was then used as input for a tight-binding calculation to determine the EDOS [8].

1.2.5 Technological applications

Disordered materials have numerous technological applications, ranging from diodes to x-ray lenses. Here we briefly discuss the industrial significance of amorphous silicon and vitreous silica. In the remainder of this thesis, we will frequently return to these materials.

Amorphous silicon

Amorphous silicon is a disordered material which is not a glass [1]. Although cheap, pure amorphous silicon has a high defect concentration. This makes it virtually useless for industrial applications. Hydrogenation of the material can solve most of the problems associated with defects and in this form it has become a low-cost solar

panel material [9]. The application of hydrogenated amorphous silicon in solar cells offers a major advantage over its crystalline counterpart: the absorption coefficient for visible light is much higher than that of the crystalline form [9]. Consequently, the thickness of an amorphous silicon solar cell is only a fraction of that of a crystalline silicon cell. The only drawback of the material is its degradation under illumination, also called the Staebler-Wronkski effect. The nature of this effect is to this day debated. Amorphous silicon is also used in the fabrication of high-resolution computer screens and in the construction of image sensors such as those found in facsimile (fax) machines.

Vitreous silica

Vitreous silica is an example of a glass. The transition to the glassy phase occurs at around $T = 1453$ K [1]. Almost all silicon atoms are bonded to four oxygen atoms and almost all oxygen atom are bonded to two silicon atoms. Vitreous silica is by far the most common glass: sand and window panes are for a large part formed by it. It also has many industrial applications. Today silica is widely used in the manufacturing of electronic devices such as computer chips. It also plays a vital role in the photo-copying process. An exciting recent application is the use of vitreous silica in the construction of three-dimensional storage memory [10].

1.3 Experimental approach

At the end of the 19th century, scientists started to turn their attention to the internal structure of matter. Knowledge of the underlying atomic structure of a material is essential for understanding its properties. For crystalline materials, it is sufficient to determine the structure of the unit cell. The unit cell contains a relatively small number of atoms; the structure of the crystal as a whole is generated by repeating the unit cell periodically in space [5]. The unit cell of a crystal can be determined experimentally through the use of x-ray diffraction, a technique which became available at the beginning of the 20th century. For a single crystal, the x-ray diffraction pattern consists of a number of sharp peaks [5]; an example of such a pattern is shown in the top frame of Figure 1.6[1]. From the positions and the intensities of the peaks, the atomic positions in the unit cell can be determined.

The x-ray diffraction pattern of an amorphous material is strikingly different from that of a crystal: the pattern in this case consists of broad *diffuse* rings [1], see the lower frame of Figure 1.6. This result indicates that the structure does not contain

[1] In the case of *randomly* oriented crystals (for example a crystal in powder form) the x-ray diffraction pattern consists of a number of *sharp* concentric rings [1].

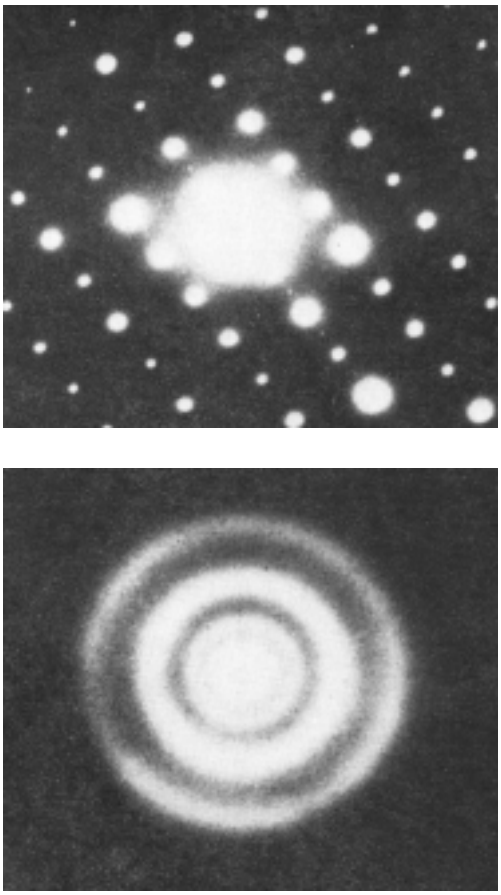

Figure 1.6: x-ray diffraction patterns of As_2Se_3 in crystalline form (top) and amorphous form (bottom). These images were reproduced with permission from Ref. [1].

a repeating unit cell. The only quantity which can be determined from the diffraction pattern in this case is the RDF (via a Fourier transform) [1]. Unfortunately, the RDF alone provides insufficient information to reconstruct the atomic coordinates: two topologically different amorphous structures can reproduce the same RDF. Consequently, x-ray scattering techniques alone are not sufficient to uniquely determine the structure of amorphous materials.

Vibrational spectroscopy is another frequently used technique to probe the structure of amorphous materials. In these experiments, vibrational modes in the material are excited optically, for example with laser light, and the spectrum of scattered light is recorded. These experiments do not provide direct structural information (unlike x-ray scattering). Instead, calculated vibrational properties of assumed structures can be compared to experiment [1]. In Chapter 6, a detailed application of this method will be discussed.

1.4 Theoretical approach

It is difficult to determine the structure of amorphous materials through experiments alone. As a result, these materials have received a great deal of attention from theorists. Theoretical work on the structure of amorphous materials began in the beginning of the 20th century. In 1932, Zachariasen proposed a number of rules with which amorphous networks could be constructed [11]. These networks are called continuous random networks or CRNs. The CRN was a breakthrough in our understanding of amorphous materials.

To this day, some of the best computer generated amorphous networks are based on the CRN model. High quality CRNs, for instance, can accurately reproduce the structural and electronic properties of amorphous silicon observed in experiments [7, 12].

1.4.1 Continuous random networks

In the CRN approach, the atomic structure is determined by the bonds between the atoms. The structure obeys the following rules:

1. The coordination of an atom is defined as the number of atoms it is bonded to. In the CRN model, each atom is perfectly coordinated to fulfill its bonding needs. For four-valent materials such as amorphous silicon perfect coordination requires each atom to be bonded to four others.

2. The atoms form a disordered network without long-range order.

3. The structure is uniform: crystalline regions and voids are absent.

With these few rules, it is possible to construct a wide range of structures with different relevance to physical systems. This relevance can be assessed from energetic considerations, which often involve the widths of bond length and bond angle distributions. To this day, a large number of CRNs have been generated. The first models were built by hand using balls and sticks made of wood [13, 14]. These early models contained a large fraction of atoms at the surface and therefore cannot be expected to accurately describe bulk properties. Moreover, the size of a hand-built model is limited and the building process is somewhat subjective.

1.4.2 The role of computer simulations

Clearly, the construction of large, high-quality CRNs by hand is not practical. Nowadays, the generation of CRNs is carried out on computers. In this way larger samples can be constructed and surface effects can be diminished through the use of periodic boundary conditions. In this case, atoms on the edge of the simulation volume interact with atoms on the opposite edge and vice versa. This way there are no special surface atoms which have different properties from the others. In practice this considerably improves the quality of the simulation of bulk properties [15]. In this thesis we focus on the bulk properties of amorphous materials so periodic boundary conditions are always used.

The first computer-generated networks, which date back to the sixties and seventies, typically contained a few hundred particles [16]. More advanced algorithms and faster computers have increased the size of the networks that can be handled to a few thousand atoms, with simulation cells of up to $40 \times 40 \times 40$ Å^3. As the simulation cells increase in size, actual devices have decreased in size. In certain solar cells, the thickness of the amorphous silicon layer (which forms the bulk of the cell) can be as low as 1000 Å [17]. To model this layer one could use periodic boundary conditions in the two extended directions. In these directions, a length-scale of 30 Å is sufficient to capture the randomness of the material (see Figure 1.3). A reasonable model of the layer would thus require a simulation volume of $30 \times 30 \times 1000$ Å^3, containing approximately 45,000 atoms. We are currently able to generate well-relaxed networks of this size by using a highly optimized algorithm (described in Chapter 4). This achievement paves the way for the generation of realistic device-size atomic networks. An exciting application of these networks would be the simulation of an entire electronic device (such as a solar cell or a transistor) at the atomic level.

Chapter 2

Computer Simulation Techniques

In this chapter we discuss three techniques to simulate amorphous materials: molecular dynamics, the activation-relaxation technique and Monte Carlo based methods. We also devote one section to the WWW algorithm—a Monte Carlo algorithm proposed by Wooten, Winer and Weaire [18]—which will play an important part in the remainder of this thesis. Although the various techniques are very different, they share one common feature, namely: a potential energy function to describe the atomic interactions. The choice of the potential is often crucial and will be discussed first.

2.1 Interaction potentials

In principle, any material structure can be obtained from the quantum mechanical Schrödinger equation. Solving the Schrödinger equation for an entire solid presents an enormous computational task and is not practical for our purposes: a number of approximations have to be made. Fortunately, the problem of modeling atomic structures is simplified because the mass of the electrons is much smaller than that of the nucleus, while the forces exerted on both are similar. As a result, the motion of the atomic nuclei is much slower than that of the electrons. This justifies the use of the Born-Oppenheimer approximation: within this approximation, the Hamiltonian is expressed as a function of the positions of the nuclei only, the rapid motion of the electrons having been averaged out [19]. Furthermore, we make the approximation that a classical description for the motion of the nuclei is adequate. Only for very light nuclei (such as hydrogen), or nuclear vibrations with a frequency ω such that $\hbar\omega \geq k_B T$ do quantum mechanical effects become important, where k_B is the Boltzmann constant and where $\hbar$ is the reduced Planck constant. In the materials considered here, the classical description is valid [20]. Within this classical description, the evolution of a system of particles follows from the Lagrangian: $L = K - V$, where K and V are the total kinetic and the total potential energy of the system,

respectively. The potential energy term, which is a function of the positions of the particles, contains the interesting information regarding the atomic interactions. Assuming such a potential can be constructed, the computational techniques presented later on proceed in different ways with determining the underlying atomic structure.

The potential energy function is thus a vital ingredient of every computer simulation. A great number of potentials have been developed over the years, many of which have been optimized for a particular material or purpose [21]. For amorphous materials, choosing the most suitable potential is a delicate matter. The consideration to be made is usually one of speed versus accuracy: the higher the accuracy of the potential, the more time is required to compute it. We discuss here two extremes of the spectrum: empirical potentials and *ab-initio* potentials.

2.1.1 Empirical potentials

Empirical potentials are the most simple potentials around. These potentials are not designed to describe the atomic bonding process in all its details. Instead, they merely try to reproduce some of the bonding properties. These properties could be derived from experimental observations, or stem from more advanced quantum-mechanical calculations. Empirical potentials are computationally cheap to evaluate; this makes them attractive candidates for simulations involving many particles. We discuss here the Keating potential and the Stillinger-Weber potential. Both of these potentials are frequently used in amorphous material research and will also play an important role in the remainder of this thesis.

Keating potential

The Keating potential [22] was originally designed to describe tetrahedrally bonded crystals, such as crystalline silicon or crystalline carbon. For these materials, the mean bond length is equal to d and the mean bond angle is equal to the tetrahedral angle $\Theta_0 = \arccos(-1/3)$. In the Keating potential, bonding geometries which deviate from these equilibrium crystal values are assigned an energy penalty:

$$E = \frac{3}{16}\frac{\alpha}{d^2}\sum_{<ij>}\left(\vec{r}_{ij}\cdot\vec{r}_{ij} - d^2\right)^2 + \frac{3}{8}\frac{\beta}{d^2}\sum_{<jik>}\left(\vec{r}_{ij}\cdot\vec{r}_{ik} + \frac{1}{3}d^2\right)^2, \qquad (2.1)$$

where $\vec{r}_{ij}$ is the vector pointing from atom i to j. The bond stretching and bond bending force constants α and β are usually obtained from a fit to the elastic properties of the crystal observed in experiments. For silicon, usual values are $d = 2.35$ Å, $\alpha = 2.965$ eV Å^{-2} and $\beta = 0.285\alpha$.

In the above equation, the symbol $\langle ij\rangle$ denotes a bonded pair of atoms $i - j$; the symbol $\langle jik\rangle$ denotes a bonded triple of atoms with atom i in the middle $j-i-k$. The

summations thus involve bonded particles only, so this potential has the additional (unphysical) requirement that an explicit list of bonds is provided. For a four-fold coordinated network, the number of bonds equals $2N$ and the number of triples equals $6N$. The time required for one energy evaluation thus grows linearly with the number of atoms N in the system.

One drawback of an explicit list of bonds is that two atoms only interact when a bond is present between them. This can lead to the undesirable situation of overlapping atoms: if no explicit bond is present in the list of bonds, two atoms can approach each other arbitrarily close without any increase in energy.

The list of bonds also disqualifies the Keating potential from studying dynamical processes or the diffusion of atoms. These processes involve the crossing of energy barriers, where the system moves from one local energy minimum to another via a first-order saddle point. In practice, for a given list of bonds, the Keating potential is a single harmonic well, with only one minimum: the bottom of this well. The Keating potential allows only for a rather artificial kind of dynamics: a new energy minimum can be constructed by making explicit changes in the list of bonds. This limitation is serious for methods such as molecular dynamics and the activation-relaxation technique. These methods ultimately depend on a potential energy landscape containing many local minima: the Keating potential will not work for these methods. In Monte Carlo based techniques however the Keating potential will prove to be extremely useful.

Stillinger-Weber potential

A more realistic empirical potential for amorphous silicon, which does not require an explicit list of bonds, is the Stillinger-Weber (SW) potential [6]. It is given by:

$$V = \epsilon A \left[\sum_{<ij>} v_{ij}^{(2)}(r_{ij}) + \frac{\lambda}{A} \sum_{<jik>} v_{jik}^{(3)}(\vec{r}_{ij}, \vec{r}_{ik}) \right], \tag{2.2}$$

where the two-body part is given by:

$$\begin{aligned} v_{ij}^{(2)}(r_{ij}) &= \left[B \left(\frac{r_{ij}}{\sigma} \right)^{-p} - 1 \right] \\ &\quad \times \exp\left(\frac{1}{r_{ij}/\sigma - a} \right) \Theta(a - r_{ij}/\sigma), \end{aligned} \tag{2.3}$$

and the three-body part by:

$$\begin{aligned} v_{jik}^{(3)}(\vec{r}_{ij}, \vec{r}_{ik}) &= \exp\left[\frac{\gamma}{r_{ij}/\sigma - a} + \frac{\gamma}{r_{ik}/\sigma - a} \right] \\ &\quad \times \left(\cos\theta_{jik} - \cos\Theta_0 \right)^2 \\ &\quad \times \Theta(a - r_{ij}/\sigma)\Theta(a - r_{ik}/\sigma). \end{aligned} \tag{2.4}$$

Table 2.1: Stillinger-Weber potential parameters as originally proposed in Ref. [6]. This set of parameters gives a valid description of the crystalline and liquid phases of silicon, but not of the amorphous phase.

ϵ (eV)	A	B	σ (Å)	p	a	λ	γ
2.16826	7.049556277	0.6022245584	2.0951	4	1.80	21.0	1.20

Here, $\Theta(x)$ is the Heaviside step function; $\vec{r}_{ij}$ is the vector pointing from atom i to atom j with $r_{ij} = |\vec{r}_{ij}|$; θ_{jik} is the angle between vectors $\vec{r}_{ij}$ and $\vec{r}_{ik}$; Θ_0 is the tetrahedral angle given by $\Theta_0 = \arccos(-1/3)$. The potential parameters are summarized in Table 2.1. The summations in Eq. (2.2) include all pairs $i-j$ and all triples $j-i-k$ of atoms in the system. In practice, only a small subset of these pairs and triples is actually computed because atoms interact only when their separation is less than $a\sigma$.

The potential parameters were fitted to the crystalline and liquid phases of silicon [6]. One important component of the fitting procedure was to ensure that the potential would correctly reproduce the crystalline structure of silicon at low pressure in a molecular dynamics simulation. Also included in the fitting procedure were the melting point and the liquid structure of silicon. Not included was the amorphous phase, for the simple reason that realistic computer-generated amorphous structures were not available at that time.

In its original form, the SW potential thus cannot be expected to accurately describe the amorphous phase. Meanwhile, realistic computer-generated amorphous structures have become available [7, 23–25]. In one study carried out by us, the SW potential was fitted directly to the amorphous phase [25]. The description of the amorphous phase improved dramatically. As it turned out, the strength of the three-body interaction must be boosted by approximately 50% to describe the amorphous phase correctly. The details of this fitting procedure are discussed in Chapter 5.

2.1.2 Ab-initio potentials

The problem associated with the SW potential outlined above is a general problem of many empirical potentials: most empirical potentials are fitted to a limited set of properties and usually give a poor description of the properties they were not explicitly fitted to. Moreover, empirical potentials do not provide any electronic structure information. A possible way out of this dilemma is offered by the *ab-initio* potentials. These potentials provide the most accurate way to calculate atomic forces, electronic properties and vibrational properties. The majority of these methods make use of the local density approximation within the limits of the density functional theory (DFT). A detailed description of this methodology is beyond the scope of this thesis: for

details see the paper of Payne *et al.* [26]

Since *ab-initio* potentials are computed from quantum mechanical first principles they are transferable to different material phases without any additional fitting. These potentials can also be used for modeling materials for which no experimental (fitting) data is available. However, substantial computational effort is required thus limiting the applicability of *ab-initio* methods to relatively small systems, in practice up to 100 atoms. The simulations discussed in this thesis involve many more particles. In order to simulate an entire electronic device the number of atoms that must be handled is approximately 45,000. For this reason we resort to the use of empirical potentials.

Empirical methods can sometimes be used as starting points for more accurate *ab initio* methods. An example of this approach is the EDOS shown in Figure 1.5. Here, the atomic structure was generated using the (empirical) Keating potential. This structure was then used as input for a more accurate tight-binding calculation to obtain the EDOS [8].

2.2 Molecular dynamics

One of the principal tools in the study of disordered materials is molecular dynamics simulations (MD). This computational method calculates the time-dependent behavior of a system. In this section, we explain the basic concepts of MD simulations and we discuss the application of MD to amorphous systems.

2.2.1 Basic MD concepts

Consider a system of N particles. Let $\vec{r}_i(t)$ and $\vec{v}_i(t)$ denote the position and the velocity of the i-th particle at time t, respectively. Assume that the particles interact with each other via some potential energy function $V(\vec{r}_1, \ldots, \vec{r}_N)$. The potential depends on the positions of the particles but contains no explicit time dependence. The classical equations of motion for such a system can be derived in the Lagrangian formalism and in this case reduce to Newton's equation of motion: $d^2\vec{r}_i/dt^2 = \vec{f}_i/m_i$, where m_i is the mass of the i-th particle and $\vec{f}_i$ the force acting on this particle. The forces are obtained from the gradient of the potential energy: $\vec{f}_i = -\vec{\nabla}_i V$.

The aim of MD is to solve Newton's equation of motion. To start the simulation, initial positions and velocities are assigned to each particle. Next, the general scheme is as follows:

1. Calculate the positions of the particles at time $t + \Delta t$ using the positions, velocities and forces at previous times.

2. Calculate the forces and velocities of the particles at their new positions.

3. Return to (1) for the next step and repeat.

One common choice to predict the positions of the particles at time $t + \Delta t$ from the positions at previous times is through the velocity Verlet algorithm [20, 27, 28]. This is one of the simplest, but also one of the most effective MD integration schemes. In this case, the positions at time $t + \Delta t$ are obtained using:

$$\vec{r}_i(t + \Delta t) = \vec{r}_i(t) + \vec{v}_i(t)\Delta t + \frac{\vec{f}_i(t)}{2m_i}(\Delta t)^2, \tag{2.5}$$

with velocities given by:

$$\vec{v}_i(t + \Delta t) = \vec{v}_i(t) + \frac{\vec{f}_i(t + \Delta t) + \vec{f}_i(t)}{2m_i}\Delta t. \tag{2.6}$$

Many other integration schemes exist, see for instance Ref. [28].

At any time t, the instantaneous temperature T is determined by the velocities of the particles:

$$3(N - 1)k_B T = \sum_{i=1}^{N} m_i |\vec{v}_i|^2, \tag{2.7}$$

where k_B is the Boltzmann constant and the factor $N - 1$ accounts for momentum conservation. The initial velocity distribution will in general not be Maxwellian. The simulation must first undergo an equilibration phase before thermal equilibrium is reached. During equilibration, there is a significant drift in the macroscopic observables of the system such as the total kinetic energy or pressure. By monitoring these observables as a function of time one can determine when equilibrium has been reached. After equilibration, the macroscopic observables will fluctuate around their equilibrium values. At this point one usually begins to calculate variables of interest (such as pressure or energy) for the accumulation of time averages. The simulation is continued until the statistical error in the averages becomes small.

MD enables us to simulate materials at the atomic level without the need for extensive theory. The only requirement is that a potential energy function must be provided. If the potential is realistic enough and if the pure classical approximation is valid, MD reproduces the dynamical processes that occur in the real substance. The problem of MD is mostly one of time scale. Atomic processes in solids, such as vibrations, typically occur on a timescale of a fraction of a picosecond. This puts an upper bound on the MD integration time step Δt in the order of a few femtoseconds. For processes that last longer than microseconds MD is not practical.

2.2.2 MD and amorphous materials

To generate amorphous structures via MD, one usually tries to imitate the melt-quenching process described in the introduction [2]. This immediately presents a

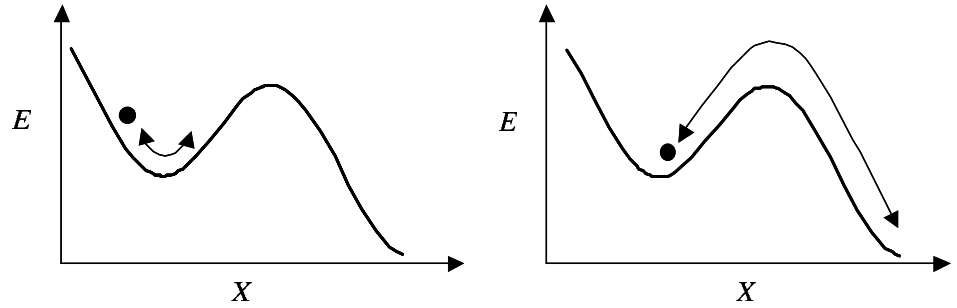

Figure 2.1: Schematic one-dimensional representation of the energy landscape of an amorphous material. Plotted is the potential energy E as a function of the degree of freedoms X. In real systems, X is a high dimensional quantity but for the purpose of this graph it is shown as a single parameter. The left frame illustrates the typical behavior of the system in MD: the system oscillates back and forth around one local minimum and the probability of crossing energy barriers is low. The behavior typical for ART is shown in the right frame. In this case, the system is actively pushed towards a first-order saddle point which enables the sampling of many local minima.

problem. Typical experimental cooling rates range from 10^{-2} to 10^{3} K s^{-1}. Even a moderate cooling trajectory spanning 100 K would soon require seconds (real time) which is clearly beyond the scope of MD. In MD simulations one is therefore forced to use much higher cooling rates of the order 10^{12} to 10^{15} K s^{-1}.

It is questionable if such high cooling rates truly describe the melt-quenching process and lead to realistic structures. For instance, MD prepared structures of amorphous silicon all suffer from the presence of a large number of defects, mostly overcoordinated atoms, which are not observed in experiments [29–31]. Moreover, the RDF often displays a shoulder on the left side of the second-neighbor peak. This indicates that these models retain a strong liquid-like structure.

Another measure for the quality of a structure is its strain. Unlike crystals, amorphous structures are strained because bond lengths and bond angles deviate from their equilibrium crystal values. Highly strained structures have poor electronic properties so one tries to keep the strain as low as possible. One important measure for strain in amorphous networks is the rms variation $\Delta\theta$ in the mean bond angle θ. Experimentally, this quantity can be inferred from the RDF: for amorphous silicon it ranges from 9.4 to 11.0 degrees. In computer simulations, strain is also measured by the potential energy: the lower the potential energy, the lower the strain.

Whether low-strain structures can be generated via MD may be judged by the ability of MD to minimize the potential energy. Unfortunately, in the case of amorphous materials MD is poorly suited for this purpose. This is related to the energy

landscape of amorphous materials. These energy landscapes consist of a large number of local minima separated by barriers that are high compared to $k_B T$. MD tends to bring the system into one of these local minima from which it rarely escapes: the simulation freezes, see Figure 2.1. Consequently, MD is not the optimal algorithm to generate amorphous structures.

2.3 Activation relaxation technique

One attempt to overcome the problem of "getting stuck" in a local energy minimum is the Activation Relaxation Technique (ART). It was developed by Barkema and Mousseau and has been applied to systems as diverse as amorphous silicon [23, 24, 32, 33], Lennard-Jones clusters [34] and proteins [35]. In contrast to MD, ART does not attempt to reproduce the details of the atomic motion. Instead, it focuses on finding significant structural changes in the material called events (which involve the crossing of energy barriers, see also Figure 2.1). For amorphous systems, this event-based approach allows the study of relaxation on much longer time scales.

2.3.1 Basic ART concepts

In ART simulations, the evolution of the system consists of following trajectories in the energy landscape connecting one local minimum to another. The underlying idea is that the potential energy surface defines the events. ART is a two-step process:

1. *Activation*: starting in a local energy minimum, the system is pushed to a nearby first-order saddle point.

2. *Relaxation*: the system is gently pushed over the saddle point and relaxed to a new minimum with a straightforward minimization scheme such as steepest descent or conjugate gradients.

The potential energy V is a function of the positions of the particles. For a system of N particles in three dimensions the potential thus depends on $3N$ distinct variables. Let $\vec{P}$ be a $3N$-dimensional vector containing all these variables in some order. In ART, the state of the system is uniquely determined by the positions of the particles and $\vec{P}$ is therefore called the state vector. In this framework, the potential energy can be written as a function of the state vector: $V = V(\vec{P})$. In a similar spirit, we define a $3N$-dimensional force vector $\vec{F} \equiv -\vec{\nabla} V(\vec{P})$ which acts on $\vec{P}$, where $\vec{\nabla}$ is the $3N$-dimensional gradient operator. In $3N$-dimensional space, local minima and first-order saddle points are easily identified as points for which $|\vec{F}| = 0$; with the additional constraint that all hessian eigenvalues be positive for energy minima, and all positive but one for first-order saddle points.

By defining the evolution of the system in $3N$-dimensional space, ART removes any constraint on the type of real space moves allowed. This is particularly important in amorphous systems where events can involve very complex local or global re-arrangements of atoms that are hard to foresee.

The most delicate phase in ART is the activation stage: starting from a local energy minimum $\vec{P}_0$ we wish to locate a nearby first-order saddle point. To this end, we draw a random $3N$-dimensional vector $\vec{X}$, normalized to unity. Next, we apply iteratively the equation:

$$\vec{P}_1 = \vec{P}_0 + \epsilon_a \vec{X}, \tag{2.8}$$

with ϵ_a a small step size, until after n iterations we obtain a state vector $\vec{P}_n$ with one negative hessian eigenvalue. At this point we are sufficiently far away from the initial minimum to start the second phase of the activation. Continuing with $\vec{P}_n$, we apply iteratively the equation:

$$\vec{P}_{n+1} = \vec{P}_n + \epsilon_b \vec{\lambda}_n, \tag{2.9}$$

where ϵ_b is again a small step size, and $\vec{\lambda}_n$ is the eigenvector corresponding to the lowest negative hessian eigenvalue at $\vec{P}_n$. For each eigenvector $\vec{\lambda}$, the vector $-\vec{\lambda}$ with reversed orientation is also an eigenvector: the orientation still has to be determined. The orientation of $\vec{\lambda}_n$ in Eq. (2.9) is chosen such that its inner product with the force is negative:

$$\vec{F}_n \cdot \vec{\lambda}_n < 0, \tag{2.10}$$

to ensure that the energy of the system increases initially. The orientation of consecutive eigenvectors $\vec{\lambda}_i$ with $i > n$ is chosen such that $\vec{\lambda}_i \cdot \vec{\lambda}_{i-1} > 0$. This ensures that we steadily walk uphill in the energy landscape, away from the initial minimum.

In general this procedure will converge to a first-order saddle point in the energy landscape. Convergence is obtained when the norm of the force becomes sufficiently small or when the inner product $\vec{\lambda}_i \cdot \vec{F}_i$ changes sign from negative to positive. The latter occurs when the barrier is just crossed. Some tuning is required to obtain optimal values for ϵ_a and ϵ_b; these optimal values vary from system to system. For the calculation of the eigenvectors we use Lanczos' method [36] to obtain the lowest eigenvalues and corresponding eigenvectors. Lanczos' method is a computationally cheap way to obtain these eigenvalues and eigenvectors, as compared to a full diagonalization of the hessian.

2.3.2 ART applications

ART naturally lends itself for two purposes: (1) it is an efficient energy minimization scheme for systems with many local minima and (2) it can be used to identify atomic re-arrangements that may occur in materials. In this section we discuss both applications, applied to amorphous silicon.

Structural relaxation

The ability of ART to easily locate minima in the energy landscape, in combination with a properly chosen accept/reject scheme, makes it a powerful relaxation method. Here we discuss the generation of well-relaxed (i.e. low energy) amorphous structures via ART. The general approach is as follows:

1. The N particles are assigned random positions drawn from a cubic simulation cell with periodic boundary conditions.

2. With a local minimization scheme (such as conjugate gradients), the initial system of step (1) is brought to a local energy minimum at zero pressure. The latter means that we also let the volume relax as one additional degree of freedom; i.e. the simulation cell remains cubic but is allowed to fluctuate in size.

3. Proceeding with the local minimum found in step (2), we use ART to locate another (nearby) energy minimum. The new minimum is accepted with the Metropolis probability [37]:

$$P = \min\left[1, \exp\left(\frac{E_0 - E_1}{k_B T}\right)\right], \tag{2.11}$$

   where T is some fictitious temperature, and E_0 and E_1 are the energies of the initial and final local minimum, respectively.

4. We repeat step (3) and continue to simulate until we obtain a configuration with good structural properties. In practice, this requires about 5 ART moves per atom.

ART prepared amorphous structures are of high quality [23]. In Chapters 5 and 6, we use ART to generate a large number of 1000-atom amorphous silicon structures. Unlike MD, ART generated structures correctly reproduce the RDF. These structures also display near perfect four-fold coordination and angular deviations below ten degrees.

Identifying events

ART provides a convenient way to find paths in the energy landscape connecting two local energy minima via a first-order saddle point. An event can thus be characterized by counting how many atoms are displaced significantly in going from one minimum to the next. In one study carried out by Barkema and Mousseau, events in amorphous silicon were identified via ART [24]. The potential used was a modified version of the Stillinger-Weber potential where the three-body interaction was boosted by 50%.

This modification significantly improves the description of the amorphous phase for this potential, see Chapter 5.

First, a well-relaxed 1000-atom structure was generated via ART using the approach outlined in the previous section. The RDF of the resulting structure was in good agreement with experiment and so were the average coordination of 3.97 and the angular deviation of 9.97 degrees. Next, many additional ART moves were generated eventually leading to a database of over 8000 events. For each event, the initial minimum, the saddle point and the final minimum were stored. The probability of occurrence of events in the database depends on the biases of ART and cannot be given a physical meaning at this point; there is numerical evidence however that these biases are Boltzmann-like [34].

Examination of the database showed that the number of atoms involved in each event ranged from 1 to 80, with a peak at about 25. A more remarkable observation was that a significant number of events in the database were topologically equivalent. The dominant type of event is illustrated in Figure 2.2. Surprisingly, this event also forms the basis of another algorithm to generate amorphous structures: the WWW algorithm [18].

2.4 Monte Carlo techniques

Monte Carlo (MC) methods are traditionally used to solve problems in statistical mechanics although they can also be used to study amorphous materials. In this section we describe the general principle of a MC simulation.

2.4.1 Basic MC concepts

For a system in thermal equilibrium at temperature T, the probability p_μ of finding the system in a state μ with energy E_μ is given by the Boltzmann distribution:

$$p_\mu = \frac{1}{Z} \exp\left(-\frac{E_\mu}{k_B T}\right), \tag{2.12}$$

with normalization constant Z:

$$Z = \sum_\mu \exp\left(-\frac{E_\mu}{k_B T}\right), \tag{2.13}$$

where the sum is over all states μ accessible to the system. Within this framework, the expectation value $\langle Q \rangle$ of some observable Q can be written as a weighted average:

$$\langle Q \rangle = \sum_\mu Q_\mu p_\mu, \tag{2.14}$$

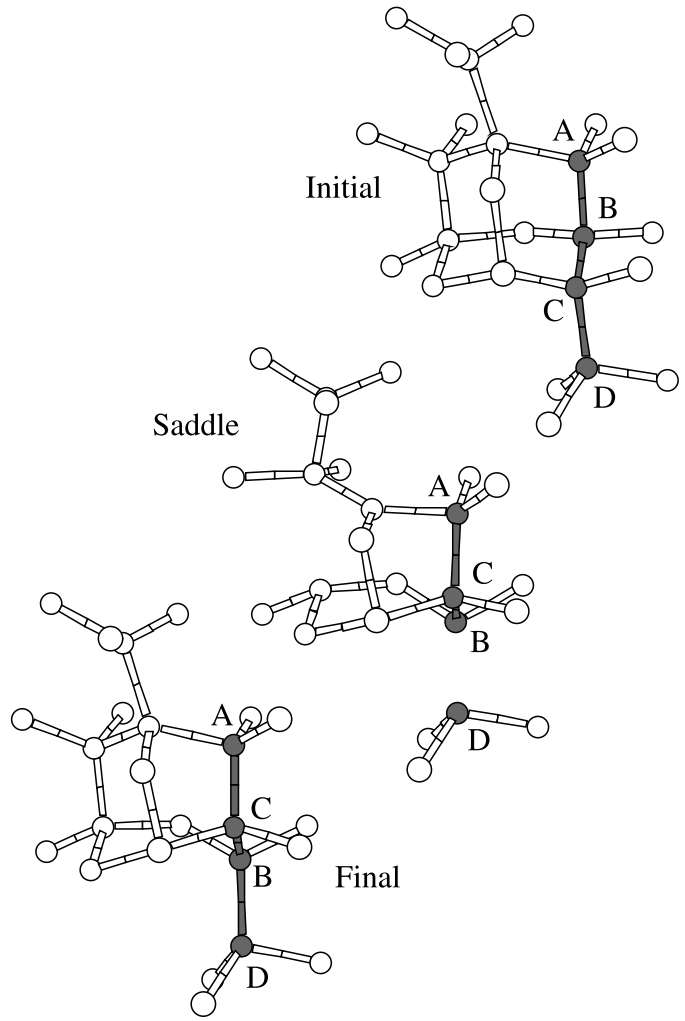

Figure 2.2: Diagram showing the most common event in the ART database for amorphous silicon. Only the four atoms labeled $\{A, B, C, D\}$ change their list of nearest neighbors in going from the initial to the final state: bonds $A-B$ and $C-D$ are broken and two new bonds $A-C$ and $B-D$ are created. Atoms are considered bonded when their separation is less than $r_c = 2.75$ Å, where r_c is taken at the minimum of the RDF between the first and second-neighbor peaks. The above event is exactly the bond transposition used in the WWW algorithm [18].

where Q_μ is the value of the observable in state μ. The quantity Z is called the partition function. It is a powerful quantity because virtually all macroscopic properties of a system, like pressure and specific heat, can be derived from it. For sufficiently simple systems, such as the ideal gas, the partition function can be determined exactly. Of course, in the case of a continuous system, the summation over states is replaced by an integration over phase-space. In many cases, the partition function cannot be calculated exactly and other methods must be used.

MC methods try to estimate the partition function by replacing the summation over all states with a summation over a subset of these states only. Suppose we pick M such states: $\{\mu_1, \mu_2, \ldots, \mu_M\}$ and in the picking procedure state μ_i has probability g_{μ_i} of being selected. Within this subset the best estimates for the partition function and the expectation values are given by:

$$Z \approx \sum_{i=1}^{M} \frac{1}{g_{\mu_i}} \exp\left(-\frac{E_{\mu_i}}{k_B T}\right), \tag{2.15}$$

and:

$$\langle Q \rangle \approx \frac{1}{Z} \sum_{i=1}^{M} \frac{1}{g_{\mu_i}} Q_{\mu_i} \exp\left(-\frac{E_{\mu_i}}{k_B T}\right). \tag{2.16}$$

The delicate part in an MC simulation is picking the M states. The most simple approach is to pick them with equal probability. In this case the selection probabilities g_{μ_i} cancel out and the estimate for the expectation value becomes:

$$\langle Q \rangle \approx \frac{\sum_{i=1}^{M} Q_{\mu_i} e^{-E_{\mu_i}/k_B T}}{\sum_{j=1}^{M} e^{-E_{\mu_j}/k_B T}}. \tag{2.17}$$

In most cases this turns out to be a poor choice. In many cases, only a small fraction of the states contribute significantly to the partition function. The total number of states is usually very high. If we select states with equal probability, the chance of mostly picking the states that contribute significantly is slim. A much better choice is to select states with the Boltzmann probability: $g_{\mu_i} \propto \exp(-E_i/k_B T)$. The estimate for the expectation value then becomes:

$$\langle Q \rangle = \frac{1}{M} \sum_{i=1}^{M} Q_{\mu_i}. \tag{2.18}$$

This is the common choice in MC methods. It is efficient because equilibrium systems often spend most time in only a relatively small number of states. By picking states with the Boltzmann probability, precisely these states will be selected.

Generating states such that each one appears with its Boltzmann probability can be accomplished using a Markov process. Given an initial state μ the Markov process

generates a new state ν. It will do so randomly: the probability of generating state ν from state μ is called the transition probability and is denoted by $P(\mu \to \nu)$. These probabilities should not depend on time nor on the history of the system. They should also obey the constraint:

$$\sum_{\nu} P(\mu \to \nu) = 1, \tag{2.19}$$

since the Markov process must always generate some new state ν.

If the Markov process satisfies ergodicity and detailed balance, it will generate states according to the Boltzmann distribution. Ergodicity means that the Markov process should be able to reach any state of the system from any other state, provided it is allowed to run long enough. Detailed balance puts an additional constraint on the transition probabilities to ensure that, in equilibrium, the Markov process samples the Boltzmann distribution:

$$\exp\left[-E_\mu/(k_B T)\right] P(\mu \to \nu) = \exp\left[-E_\nu/(k_B T)\right] P(\nu \to \mu). \tag{2.20}$$

It is allowed for the Markov process to, given a state μ, generate the same state μ. In other words, the transition probability $P(\mu \to \mu)$ does not have to be zero. This is extremely useful if we wish to avoid states in the Markov process with undesirable properties (for instance states with high energy). If the Markov process would generate such a state ν from a state μ, we can immediately go back to state μ, forget state ν was ever generated and try again. In this case, the transition probability becomes:

$$P(\mu \to \nu) = g(\mu \to \nu) A(\mu \to \nu), \tag{2.21}$$

where $g(\mu \to \nu)$ is the probability of generating state ν from state μ and $A(\mu \to \nu)$ is the acceptance probability. If the Markov process generates state ν from state μ, the acceptance probability tells us we should accept this state ν a fraction of the time $A(\mu \to \nu)$. The condition for detailed balance may be rewritten:

$$\frac{g(\mu \to \nu) A(\mu \to \nu)}{g(\nu \to \mu) A(\nu \to \mu)} = \exp\left(\frac{E_\mu - E_\nu}{k_B T}\right). \tag{2.22}$$

A good MC algorithm is one in which the acceptance probability is of order one. As an example we consider a system of N particles which interact via some potential energy function. We generate states by selecting one of the particles at random, followed by a random displacement of this particle. The probability of generating state ν from state μ is thus determined by the probability of selecting a certain atom: $g(\mu \to \nu) = 1/N$. The condition for detailed balance now reduces to:

$$\frac{A(\mu \to \nu)}{A(\nu \to \mu)} = \exp\left(\frac{E_\mu - E_\nu}{k_B T}\right). \tag{2.23}$$

Suppose we generate state ν from state μ and that state μ has the lower energy. As a result, the rhs of Eq. (2.23) is smaller than one and hence $A(\nu \to \mu) > A(\mu \to \nu)$. To maximize the acceptance probability, it would be ideal to set $A(\nu \to \mu)$ equal to unity and to adjust $A(\mu \to \nu)$ in order to satisfy Eq. (2.23). In this case $A(\mu \to \nu)$ should be set to $\exp\left[(E_\mu - E_\nu)/k_B T\right]$. The optimal algorithm is thus one in which:

$$A(\mu \to \nu) = \min\left[1, \exp\left(\frac{E_\mu - E_\nu}{k_B T}\right)\right]. \tag{2.24}$$

This is the Metropolis probability [37] which has become the method of choice in the majority of MC studies.

2.4.2 MC and amorphous materials

MC methods have not received much attention in the material science community where MD is usually the method of choice. As we already pointed out MD is not optimally suited to study amorphous materials. MC offers a number of advantages. In particular, it is flexible in how one chooses to generate the Markov process. In Chapter 3, MC techniques are used to study the structure of polysilane and polysilyne, two silicon based organic compounds. In Chapter 4 we use MC to generate large structures of amorphous silicon and vitreous silica. This application is based on the WWW algorithm [18] which forms the subject of the next section.

2.5 The WWW algorithm

In 1985, Wooten, Winer and Weaire proposed a Monte Carlo scheme for the generation of tetrahedrally bonded, four-fold coordinated, amorphous structures [18]. The scheme was used to generate networks of amorphous silicon but has since then also been applied to other materials. The method — from here on called the WWW algorithm — was one of the first attempts to study amorphous materials outside the framework of MD. In this section, we discuss the WWW algorithm in its original form. In this form it can be used to generate structures containing up to a few thousand atoms. A number of modifications have been proposed recently by us to improve the scaling of the algorithm [7,12]. These modifications allow well-relaxed structures containing tens of thousands of atoms to be generated, see Chapter 4.

2.5.1 Original WWW algorithm

The purpose of the WWW algorithm is to generate high-quality CRNs [11]. As already pointed out in the introduction, the structure of amorphous materials is believed to be well described by the CRN model. The quality of a CRN is determined by its

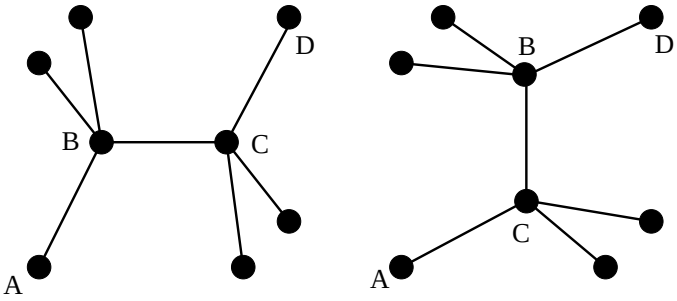

Figure 2.3: Diagram depicting the WWW bond transposition. Four atoms $\{A, B, C, D\}$ are selected following the geometry shown left. Next, bonds $A - B$ and $C - D$ are broken and bonds $A - C$ and $B - D$ are created, resulting in the geometry shown right.

strain, which is measured by the deviations of bond lengths and bond angles from their crystalline values. The ideal CRN is thus one with a low spread in the bond length and bond angle distributions.

In the WWW approach, a CRN consists of the positions of N atoms and an explicit list of the $2N$ bonds between them. The structural evolution of the network is formed by a sequence of Monte Carlo moves called bond transpositions, see Figure 2.3. In this way we sample topologically distinct configurations without changing the coordination of any atom. There are indications that the WWW bond transposition is also the mechanism preferred by nature, see for instance Figure 2.2. Note that realistic moves are not a requirement here since the WWW algorithm is primarily used as a relaxation technique.

The generation of a CRN starts with a cubic diamond structure which is randomized by a large number of bond transpositions. The randomization phase is important because contamination of the final amorphous structure by some memory of the crystal must be avoided. After randomization, the network is relaxed through a sequence of bond transpositions, accepted with the Metropolis acceptance probability [37]:

$$P = \min\left[1, \exp\left(\frac{E_b - E_f}{k_B T}\right)\right], \tag{2.25}$$

where k_B is the Boltzmann constant, T is the temperature, and E_b and E_f are the total *minimized* energies of the system before and after the proposed bond transposition. With an explicit list of bonds, it is possible to use a simple interaction such as the Keating potential [22] to calculate energy and forces, see Eq. (2.1). The list of bonds thus determines the atomic positions uniquely, since the energy is kept minimized at all times.

Table 2.2: Comparison of MD, ART and WWW amorphous silicon structures. For each model we show its reference, the number of atoms N it contains, the variation in the bond angle $\Delta\theta$ in degrees and the average coordination n_c. Note that the WWW structure has $n_c \equiv 4$ per definition since it uses an explicit list of bonds .

	MD	ART	WWW
Ref.	[38]	[23]	[39]
N	1728	1000	4096
$\Delta\theta$	14.0	9.97	10.51
n_c	4.054	3.97	4

Using the approach described above, Wooten and Weaire generated a 216-atom model with an angular distribution as low as 10.9 degrees [16]. A decade later, using the same approach but more computing power, Djordjević, Thorpe, and Wooten produced two large 4096-atom networks of even better quality, with a bond angle distribution of 11.02 degrees for configurations without four-membered rings and 10.51 degrees when these rings were allowed [39].

In Table 2.2 we compare MD, ART and WWW generated structures of amorphous silicon. The MD structure was prepared by Justo *et al.* in 1998 [38] and its properties are representative of what can be obtained in MD; the ART structure was prepared by Barkema and Mousseau [23]; the WWW structure was prepared by Djordjević, Thorpe, and Wooten [39]. The angular deviation of the MD structure is outside the experimental range of 9.4 to 11.0 degrees; ART and WWW produced structures display lower angular deviations in agreement with experiment. For large simulations involving many atoms the WWW algorithm is the method of choice.

2.6 Outline of this thesis

In Chapter 1 we provided some background information on amorphous materials. We discussed their physical properties and we mentioned their technological importance. In this chapter we have reviewed the computational techniques most commonly used to study these materials. The topics discussed in these two chapters serve as a preparation for the work presented in the remainder of this thesis. This work is devoted to the study of amorphous materials via computer simulations and can be split up into two parts:

1. **Structure generation**: In this part we present techniques that can be used to generate large and realistic structures of amorphous materials. We study

polysilanes and polysilynes in Chapter 3 and amorphous silicon and vitreous silica in Chapter 4.

2. **Properties**: In this part we use computer-generated structures to study the physical properties of amorphous materials. In Chapters 5 and 6 we study the vibrational properties of amorphous silicon. In Chapter 7 we determine the configurational entropy of amorphous silicon and vitreous silica.

Chapter 3

Polysilane and Polysilyne Simulations

In this chapter we present Monte Carlo simulations of the formation and structure of polysilane and polysilyne networks. Polysilanes and polysilynes are silicon based organic compounds. Traditionally, these compounds were studied using *ab initio* techniques, thereby limiting the size of the structures that could be handled to a few particles. These small units provide little information about the structure over longer length scales. The simulation technique described here allows for the investigation of large systems, containing up to 10000 monomers. Our results show that ring formation is an important factor for both materials. For polysilyne networks, a random structure is found incorporating cyclic substructures, linear chains and branching points.

This chapter is based on R.L.C. Vink, G.T. Barkema, C.A. van Walree, and L.W. Jenneskens, *Simulation of polysilane and polysilyne formation and structure*, J. Chem. Phys. **116**, 854 (2002).

3.1 Introduction

The electronic and optical properties of silicon-based materials are strongly related to the structure of the silicon skeleton and the size and surface properties of the materials [40]. Crystalline silicon, which consists of a three-dimensional silicon framework, is an indirect semi-conductor with a band gap of around 1.10 eV. In other forms of three-dimensional silicon, such as nano-crystalline and porous silicon the band gap is somewhat larger and quasi-indirect, so that rather efficient photo- and electroluminescence have been observed. In contrast, one-dimensional polysilanes $(\text{-SiR}_2\text{-})_n$, which are linear polymers consisting of a backbone of silicon atoms to which two organic side groups R are bonded [41, 42], exhibit well-defined, intense absorption

and emission bands in the UV spectral region. An interesting aspect of the electronic spectra of polysilanes is that both in the solid state and in solution they are often strongly temperature dependent. This thermochromism finds its origin in conformational changes of the silicon backbone, which is said to be σ-conjugated. Polysilanes are usually synthesized by polymerization of SiR_2Cl_2 monomers, employing alkali metals as coupling agent. The heterogeneous polymerization process is rather complicated, but is proposed to involve both silyl radicals and silyl anions as reactive intermediates [43]. It is noteworthy that in the alkali metal-mediated polymerization there is a tendency to form cyclic oligosilane oligomers.

Organic side chain appended silicon-based materials with a higher dimensionality than polysilanes can be obtained by polymerization of trichlorosilanes $RSiCl_3$ [44, 45]. This yields so-called polysilynes, in which each silicon atom is bonded to three other silicon atoms and to one organic side group R. Polysilynes exhibit a broad indirect semiconductor-like absorption which tails into the visible region [45–47]. The fluorescence, emanating from trapped excitons, is situated in the visible region and has a broad appearance.

Since their discovery, the structure of polysilyne networks has been the subject of debate. Polysilynes were initially assumed to consist of a rigid network of interconnected ring-like structures [45], but it was also argued that they form essentially two-dimensional sheetlike networks [46]. According to another point of view it was reasoned that the growth of a polysilyne preferably occurs at the termini of the polymer chain, which leads to a hyper-branched, dendritic morphology [48]. Cleij *et al.* used PM3 calculations on silyl radicals and silyl anions to show that linear chain propagation is more likely to occur than branching [49]. It furthermore appeared that formation of silicon ring structures is also an aspect to take into account. Hence, the PM3 calculations led to the idea that polysilynes possess a predominant one-dimensional structure with small branches and incorporated rings.

A number of experimental observations also indicates that polysilyne networks may be viewed as linear structures. For a series of *n*-hexyl substituted hybrid polysilyne/polysilane networks thermochromism (both in the solid state and in solution), fluorescence and a degree of exciton delocalization were observed which resembled the properties of linear polysilanes [50]. Even more surprising, for a polysilyne with oligo(oxyethylene) side chains in aqueous environment thermoresponsive behavior very similar to that of related linear polysilanes was found [49]. This thermoresponsive behavior has to originate from folding and unfolding processes of the silicon framework. These results imply that the silicon backbone of polysilynes is to a certain extent flexible and behaves much like one-dimensional systems. Similar conclusions can be drawn from the photophysical properties of well-defined oligosilane dendrimers [51, 52].

In this chapter, we present computer simulations of the formation of polysilane

and polysilynes, and study the properties of the resulting networks. There are three essential characteristics that we included in these simulations:

1. The starting point is a random mixture without any polymerization.
2. Monomers diffuse, and when they meet they can form stable bonds.
3. Conglomerations of bonded monomers are not stationary and rigid, but they show some diffusion and flexibility.

More specifically, in our simulations we implemented the time evolution by means of Monte Carlo dynamics (since the dynamics is overdamped because of the solvent), and the elastic properties of conglomerations were described by an empirical interaction potential featuring bond stretching and bond bending, with parameters chosen to match experimental properties of crystalline silicon. It is anticipated that a thorough knowledge of the structure of polysilanes and polysilynes gives more insight in the properties of these silicon-based materials.

3.2 Model of polysilane and polysilyne

The simulations are started without any trace of polymer present. The only bonds initially present in the system are therefore the internal Si-R bonds shown in Figure 3.1. However, in the course of the simulation, as monomers react with each other, Si-Si bonds form. In these simulations, both the silicon atoms and the alkyl groups are treated as hard spheres with radii r_S and r_R, respectively, see Figure 3.1. In the ground state, the Si-R distance is set to r_{RS} and the R-Si-R bond angle to the tetrahedral angle Θ_0, with $\cos(\Theta_0) = -1/3$. During the simulation, as the monomers diffuse and react, distances and angles are allowed to fluctuate around their ground state values.

In the model, all non-bonded particles interact according to hard-sphere potentials. Bonded particles interact according to a Keating-like potential [22], which describes the stiffness of the network with respect to bond length and bond angle distortions. This potential requires an explicit list of all bonds, and is given by:

$$\begin{aligned} V &= \frac{3\alpha}{16} \sum_{\langle ij \rangle} \frac{1}{d_{ij}^2} \left(\vec{r}_{ij} \cdot \vec{r}_{ij} - d_{ij}^2 \right)^2 \\ &\quad + \frac{3\beta}{8} \sum_{\langle jik \rangle} \frac{1}{d_{ij} d_{ik}} \left(\vec{r}_{ij} \cdot \vec{r}_{ik} + \frac{1}{3} d_{ij} d_{ik} \right)^2 , \end{aligned} \tag{3.1}$$

where the summations include all pairs and triples in the system; α and β are the bond stretching and bond bending force constants, respectively; $\vec{r}_{ij}$ is the vector pointing

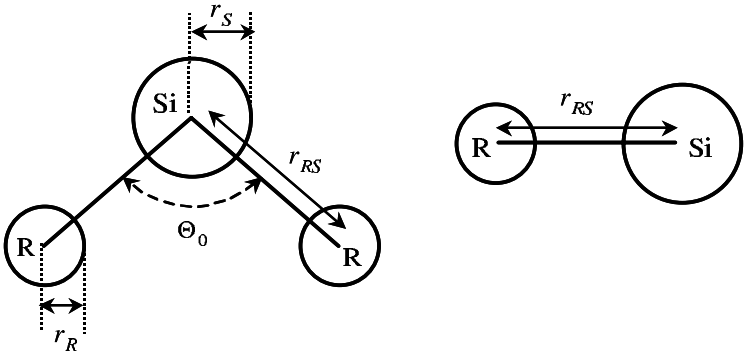

Figure 3.1: Diagrammatic representation of SiR_2 (left) and SiR fragments (right). Silicon atoms are labeled **Si** and alkyl groups are labeled **R**. Their respective radii are r_S and r_R. The ground state Si-R distance is set r_{RS} and the ground state R-Si-R angle to the tetrahedral angle $\Theta_0 = \arccos(-1/3)$.

from particle i to particle j and d_{ij} is the ground-state distance between particles i and j; if these are both silicon atoms, d_{ij} equals r_{SS}, otherwise one particle is a silicon atom and the other an alkyl fragment, and d_{ij} equals the equilibrium Si-R distance r_{RS} in that case. The values for the parameters used in the simulation are listed in Table 3.1.

3.3 Simulation dynamics

The simulation starts with a configuration of 10000 SiR_2 or 10000 SiR monomers, placed at random positions and with random orientations in a periodic box, under the constraint of the hard-sphere interactions. The size of the box is chosen such that the particle density equals $2.0 \cdot 10^{-4}$ monomers per $Å^3$, matching the experimental conditions where typically 20 mmol of monomer is put into a reaction volume of 60 ml [50]. The nature of the dynamics is two-fold: monomer diffusion and reactions between monomers. We simulate this with the approach of rare-event dynamics [53]. In this approach, the two types of events are monomer displacements, which occur with a rate r_1, or bond formation between two silicon atoms, which occur with a rate r_2. This reaction can only occur when (1) both Si atoms are not saturated, i.e., they have less than four bonds to either alkyl-groups or other silicon atoms, (2) the silicon atoms are separated less than a cut-off distance r_c, and (3) the silicon atoms are not mutually bonded already. We continue to simulate until reactions become rare. This occurs when approximately 80% of all possible Si-Si bonds have formed. On a fast workstation (21264 Alpha processor, 667 MHz), using standard link-cell

Table 3.1: Values of parameters used in the simulation: r_{RS} and r_{SS} are the ground state Si-R and Si-Si distances, respectively, and r_S and r_R are the radii of a silicon atom and an alkyl group, respectively; values for these four parameters were adapted from an MM2-calculated structure of dodecamethycyclohexasilane. Reactions between two silicon atoms can occur only when their separation is less than r_c; r_m is the maximum particle displacement during a diffusion step; α and β are the standard Keating parameters [22]; T is the temperature; r_1 and r_2 are the rates of diffusion and reaction, respectively. Distances are in Å, the Keating parameters in ev Å^{-2} and the temperature in Kelvin.

r_{RS}	r_{SS}	r_S	r_R	r_c	r_m	α	β	T	$r_1 : r_2$
1.89	2.35	1.20	1.10	2.50	0.30	2.965	0.8450	293.0	5 : 1

and neighbor table methods, one such simulation takes about one week of processing time. We then investigate the structure of the final network.

When concentrating on the final structure, the overall scaling of the rates r_1 and r_2 is irrelevant, since it only affects the time scale of the simulation. The networks presented here were generated using $r_1 : r_2 = 5 : 1$. To the best of our knowledge, no experimental data on the reaction rates r_1 and r_2 are reported. However, we have established that the networks are insensitive to the ratio of rates. For $r_1 : r_2 = 1 : 2$ and $1 : 10$, we obtained similar results.

We recall that polysilanes consist of silicon atoms bonded to two alkyl groups, and polysilynes by silicon atoms bonded to one alkyl group. Therefore, the state of a system consisting of 10000 SiR_2 (SiR) monomers is specified by a total number N of 30000 (20000) locations in three-dimensional space. We denote the total number of pairs of silicon atoms that are able to react as P, a quantity that varies during the simulation. In terms of N and P, the total diffusion rate R_1 can be written as $R_1 = r_1 N$, the total reaction rate R_2 as $R_2 = r_2 P$, and the total rate of events as $R_1 + R_2$. Events are selected one-at-a-time. To each event, a time-increment of $\Delta t = 1/(R_1 + R_2)$ is attributed. The likelihood that this event is a diffusion event or a reaction event, is equal to $R_1 \Delta t$ and $R_2 \Delta t$, respectively.

To describe the diffusion process, we introduce the following event:

1. We select randomly one silicon atom or alkyl group.

2. For this silicon atom or alkyl group, a displacement is proposed, drawn randomly from within a sphere with radius r_m.

3. If the hard-sphere constraints are violated, the proposed displacement is rejected. Otherwise, the displacement is accepted with the Metropolis acceptance

probability [37]:

$$P_m = \min\left[1, \exp\left(\frac{E_b - E_f}{k_b T}\right)\right], \tag{3.2}$$

where k_b is the Boltzmann constant, T is the temperature, and E_b and E_f are the total (Keating) energies of the system before and after the random displacement.

Since we displace single silicon atoms and alkyl groups, the above procedure also allows for the vibration and rotation of monomers.

To describe reactions in the simulation, we introduce the following reaction event:

1. We select randomly one of the P pairs of silicon atoms able to react.

2. A bond is placed between the two silicon atoms constituting the selected pair.

3.4 Results

Polysilanes and polysilynes networks are obtained using the simulation techniques described above. Each system contains a total of 10000 monomers. To characterize the structure of these networks, we proceed as follows. First, we identify clusters, defined as a group of connected monomers. For each cluster, we calculate its genus g given by $g = 1 + e - n$, where e is the number of Si-Si bonds in the cluster and n the number of silicon atoms in the cluster. The genus helps to identify the topology of the cluster: it measures the number of bonds that can be cut before the cluster loses its connectivity. For example, if $g = 0$, the cluster is a chain of connected monomers, i.e. a polymer, and if $g = 1$, the cluster is a ring, possibly with a number of side-chains attached. Networks with high values of g have a complicated topology.

3.4.1 Polysilane

We performed one simulation containing 10000 SiR_2 fragments at a density of $2.0 \cdot 10^{-4}$ monomers per Å^3. At the end of the simulation 80.4% of all possible Si-Si bonds were formed. Since silane is bifunctional, only two types of structure exist in this case: chains (polymers) with $g = 0$ and rings with $g = 1$. The system consists of 2814 separate clusters, ranging in size from one up to 14 silicon atoms. The clusters are distributed randomly through space. Of these clusters, 1961 are chains, the remainder are rings. Polymer length and ring size statistics are shown in Figure 3.2. In the simulation, 58.0% of the silane monomers form linear structures; a substantial fraction of 42.0% of the monomers is found in rings. The Si-R and the Si-Si bond lengths are 2.09 ± 0.12 Å and 2.31 ± 0.12 Å. The R-Si-R and Si-Si-Si bond angles were found to be 109.8 ± 7.6 and 106.0 ± 12.3 degrees, respectively.

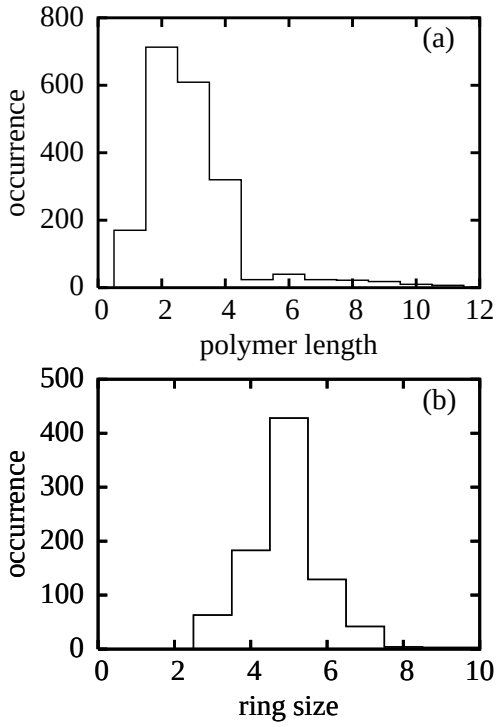

Figure 3.2: Histograms showing polymer length (a) and ring size distribution (b) for a polysilane consisting of 10000 monomers at density $2.0 \cdot 10^{-4}$ fragments per $Å^3$.

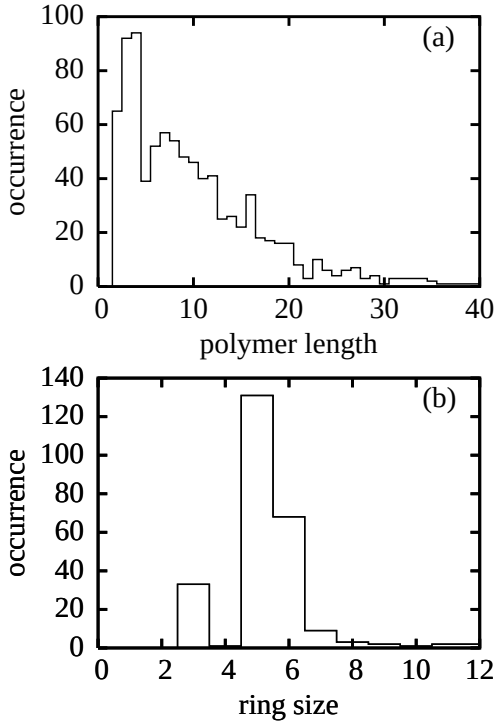

Figure 3.3: Histograms showing polymer length (a) and ring size statistics (b) for a polysilane consisting of 10000 monomers at density $5.0 \cdot 10^{-3}$ monomers per Å^3.

To study the effect of the monomer density, an additional polysilane is generated at an increased density of $5.0 \cdot 10^{-3}$ monomers per Å^3. For this network, 91.3% of all Si-Si bonds were formed. In this case, the system contains 1125 separate clusters, ranging in size from two up to 47 monomers. The clusters are again distributed randomly through space. Of these clusters, 872 are linear structures, the remainder are rings. Figure 3.3 shows the polymer length and ring size distributions. For this system, the Si-R and the Si-Si bond lengths are 2.09 ± 0.08 Å and 2.32 ± 0.08 Å. The R-Si-R and Si-Si-Si bond angles are 107.2 ± 5.0 and 111.1 ± 7.6 degrees, respectively.

3.4.2 Polysilyne

We also performed one simulation involving 10000 SiR monomers at a density of $2.0 \cdot 10^{-4}$ monomer fragments per Å^3. At the end of the simulation 81.0% of all possible Si-Si bonds were formed. Since silyne is trifunctional, the genus of the structures can

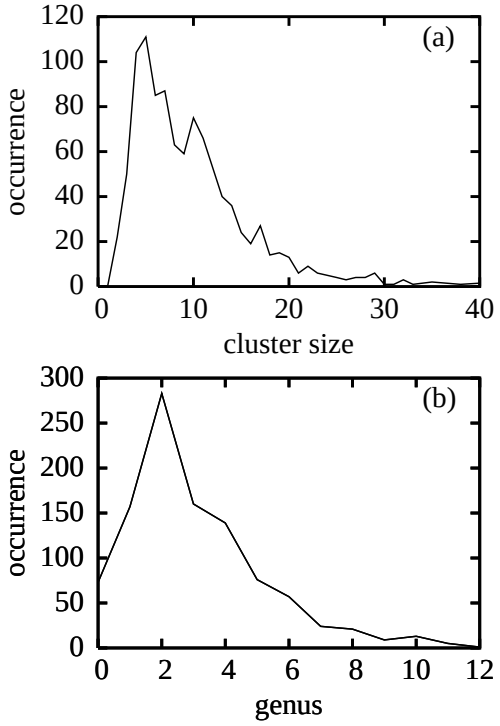

Figure 3.4: Histogram of cluster size (a) and genus number (b) of a polysilyne consisting of 10000 monomers at density $2.0 \cdot 10^{-4}$ monomers per Å^3.

now reach large values. The final network consists of 1023 separate clusters, ranging in size from one up to 46 monomers. Figure 3.4a shows a histogram of the cluster sizes. Of these clusters, only 2.1% are chains, 8.6% possess a monocyclic structure and the remaining clusters are structures with $g > 1$. Fig 3.4b shows a histogram of the genus numbers found. The structure is not dendritic: by far the largest fraction of monomers are part of rings; the fraction of monomers in chains or side-chains is 7.0% only. Moreover, the chains and side-chains are short, consisting at most of three monomers. For this network, the Si-R and the Si-Si bond lengths are 2.09 ± 0.08 Å and 2.28 ± 0.14 Å, respectively. The Si-Si-Si bond angle is 101.5 ± 18.2 degrees.

To study the effect of the monomer density, an additional silyne network is generated at an increased density of $8.0 \cdot 10^{-3}$ monomers per Å^3. The network is shown in Figure 3.5. In this case, 89.9% of all possible Si-Si bonds are formed. The vast majority of monomers (99.7%) form one large cluster with a genus of 3472. This cluster consists mostly of connected rings; 96.8% of the monomers are part of rings.

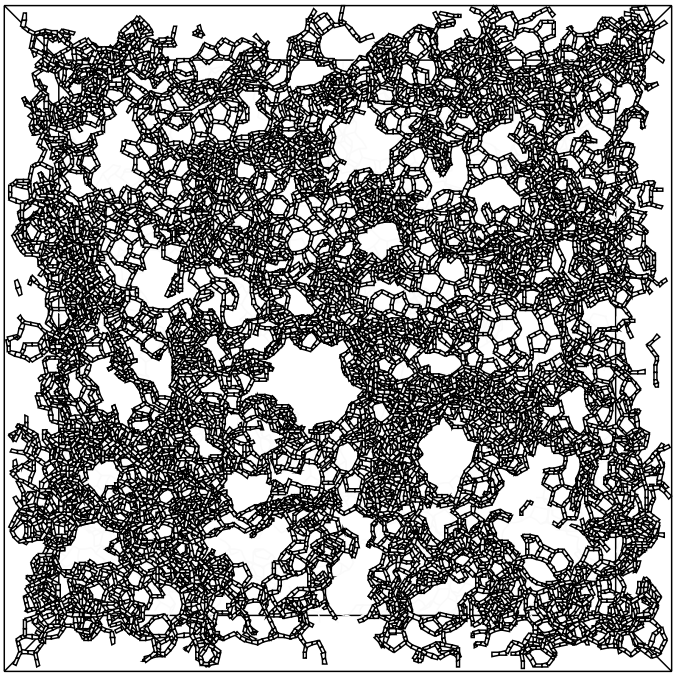

Figure 3.5: Polysilyne network at a density of $8.0 \cdot 10^{-3}$ monomers per $Å^3$. For clarity, the alkyl groups are not shown.

The ring statistics are shown in Figure 3.6.

3.5 Discussion and conclusion

The Wurtz-type polymerization of dichlorodialkylsilanes and trichloroalkylsilanes is a complex process [41–43]. The polymerization proceeds by a chain growth process at the alkali metal surface, which plays an essential role in the formation of polymers of high molecular weight. This is for instance indicated by the fact that employment of homogeneous coupling agents leads to formation of only oligomeric materials [42, 54]. Which products actually are obtained also depends on parameters as the nature of the alkali metal, the solvent and the type of organic side chain. Moreover, after the initial stages of the formation of linear polymers, secondary reactions including depolymerization, backbiting by silyl anions and redistribution of chain lengths are known to occur [41–43]. For polysilynes, secondary reactions such as ring opening reactions (by analogy with spirosilanes [48]), ring-size redistribution and coupling to linear moieties may be of interest. It is a virtually impossible task to perform a

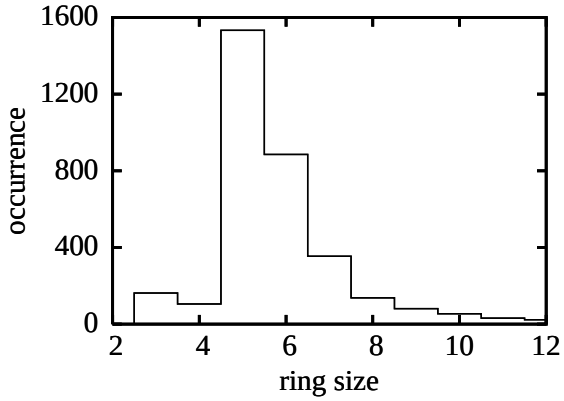

Figure 3.6: Ring size histogram for a polysilyne network consisting of 10000 monomers. This cluster was generated at a density of $8.0 \cdot 10^{-3}$ monomers per $Å^3$.

simulation of a Wurtz-type polymerization at a metal surface, hereby also taking all these contributing factors into account. Nevertheless, as the approach we used led to results which adequately reflect experimental findings, we believe that our results are sound and provide insight into the structure and properties of polysilanes and polysilynes.

For polysilane, for instance, the simulations adequately predict the effect of the monomer density on the nature of the silicon compounds formed. At low density, the system has a strong tendency to form predominantly five-membered rings, see Figure 3.2b. This finding is in accordance with the experimental observation that formation of cyclic silicon-based compounds is favored by slow addition of the monomer to the alkali metal, i.e. by maintaining a low monomer concentration [55, 56]. The ring size distribution shown in Figure 3.2b, which indicates that five-membered rings are formed in excess, is in agreement with the experimental distribution such as obtained upon reaction of a dialkyldichlorosilane under kinetic control [41]. It is noteworthy that in an equilibrium distribution, which arises from redistribution of the kinetic mixture upon use of excess alkali metal, the six-membered ring dominates. As expected, the amount of long linear fragments increases strongly when the monomer density is increased, see Figures 3.2a and 3.3a. At low density the chains have more time to close and form rings, whereas at high density chain catenation is faster. At the higher concentration relatively more six-membered rings are formed. Furthermore, the length of the linear fragments is rather moderate, which may support the idea that the presence of an alkali metal surface is essential for the formation of high molecular weight polymers [42, 54].

For the polysilyne, the simulations also predict the formation of cyclic structures.

At low concentration virtually all monomers are incorporated into rings. The number of mutually bonded rings is already considerable. At high monomer density, a very complex network of genus 3472 is obtained. Of the monomers, 96.8% is incorporated in rings, which mainly contain five or six silicon atoms. Thus, whereas in the linear case a higher concentration leads to a larger amount of long linear structures, for the polysilynes the silicon atoms are still virtually exclusively found in cyclic structures. A few linear fragments are however also present. The simulated structure is in close agreement with the characteristics of the material that was isolated after the first stage of a polymerization of trichloroalkylsilanes [57]. Our simulations indicate that the structure of polysilynes can be viewed as a network of silicon atoms comprising fused cyclic structures and cyclic structures mutually connected by a single Si-Si bond. There is neither indication of formation of a regular sheetlike arrangement of silicon atoms [46] nor of a dendritic structure [48], at least in our simulations where there is no difference in reactivity between Si-SiCl-Si groups and terminal SiCl groups.

An interesting question is to what extent the structure of the polysilyne depicted in Figure 3.5 is consistent with the flexibility of polysilynes such as indicated by its thermal properties, i.e. whether the structure allows for conformational changes affecting the degree of σ-conjugation. Although at first sight the network of fused cyclic structures seems to be quite rigid, there are a number of features which suggest a certain degree of flexibility. Firstly, some (short) linear fragments and extended cyclic structures, both of which imply conformational flexibility, are distinguishable in Figure 3.5. Secondly, there is also a number of rings which are interconnected by a single Si-Si bond. This should give the possibility for rings to rotate with respect to each other; i.e., the structure depicted in Figure 3.5 is not rigid. A third factor which may contribute to the flexibility of the networks is that silicon rings are known to be highly flexible. In this context it is of interest that even in the solid state dodecamethylcyclohexasilane Si_6Me_{12} undergoes a rapid ring inversion [58]. While it is not likely that ring inversions occur for fused ring systems, they might be possible for rings connected to linear chains or connected to other rings by a single Si-Si bond.

Hence, the networks obtained in our simulations are already flexible. However, there are a number of reasons why experimentally prepared polysilynes can even more easily undergo conformational changes. A preferred polymer extension at the termini of already formed polymer, as discussed above, will enhance chain growth rather than branching. This will have the consequence that polysilynes in reality may contain more linear chains and larger cyclic structures than depicted in Figure 3.5. Another factor is the size of the organic side group R. While in the simulations R has the dimensions of a methyl group, much more bulky side groups such as hexyl, isobutyl and phenyl substituents have been used in experimental studies [46, 50]. If bulky side groups are present the network is expected to be less dense and to incor-

porate more linear fragments than in the present case.

A question left to be answered is whether polysilynes obtained by a Wurtz-type condensation should be regarded as one, two or three-dimensional silicon materials. At first sight, the silicon network in Figure 3.5 percolates in three dimensions. However, the description of the simulated polysilyne networks by $g = 1 + e - n$, which is Euler's equation for two-dimensional networks [59], implies that topologically the silicon backbones of these materials are best regarded as two-dimensional systems. This is consistent with the electronic spectra which approach that of an indirect band gap semiconductor [45–47].

In summary, we have shown that the formation and structure of polysilanes and polysilynes can be adequately described by a simulation based on rare event dynamics of diffusion and reaction steps. The simulations indicate that ring formation is an important factor for both types of materials. Insight has been obtained in the conformational flexibility of polysilynes such as inferred from experimental studies. It is anticipated that simulations can provide an even more comprehensive picture when variation of the size of the organic substituent R and differences in reactivity of different types of Si-Cl functionalities are implemented. Also the structure of hybrid polysilane/polysilyne systems can be investigated with this computational approach. This would be the subject of further work.

Chapter 4

A Scalable WWW Algorithm

In this chapter we present an algorithm for the generation of large, high-quality continuous random networks. As already pointed out in the introduction, the atomic structure of amorphous materials is believed to be well described by the continuous random network model. The algorithm is a variation of the algorithm introduced by Wooten, Winer, and Weaire [18]. By employing local relaxation techniques, local atomic rearrangements can be tried in times that scale almost independently of system size. This scaling property of the algorithm paves the way for the generation of realistic device-size atomic networks.

The work presented here is based on R.L.C. Vink, G.T. Barkema, M.A. Stijnman, and R.H. Bisseling, *Towards device-size atomistic models of amorphous silicon*, Phys. Rev. B **64**, 245214 (2001).

4.1 Introduction

The structure of amorphous semiconductors is believed to be well represented by the continuous random network (CRN) model introduced by Zachariasen more than sixty years ago [11]. As a result, the generation of high quality CRNs has been the subject of investigation for many years. The first CRNs were built by hand, see for instance the work of Polk [14]. Nowadays, the generation of CRNs is mostly carried out on computers.

The first computer-generated networks, which date back to the sixties and seventies, typically contain a few hundred particles. More advanced algorithms and faster computers have increased the size of the networks that can be handled to a few thousand atoms, with simulation cells of up to $40 \times 40 \times 40$ Å^3. As the simulation cells increase in size, actual devices have decreased in size. For example, the thickness of the amorphous silicon layer in certain solar cells can be as low as 1000 Å; and because in-plane periodicity after approximately 30 Å is expected to be a good ap-

proximation of the macroscopic lateral size, a reasonable model of this layer would require a simulation cell of $30 \times 30 \times 1000$ Å^3, containing approximately 45,000 atoms. This is only one order of magnitude larger than currently feasible. For other electronic devices, lithography on 0.1 μm (=1000 Å) technology is expected to be reached in the coming decade.

We present a computational approach to generating large CRNs, and discuss the properties of high-quality networks containing up to 60,000 particles. This achievement shows that the generation of device-size atomic configuration networks is within reach. Our algorithm is similar in spirit to the algorithm of Wooten, Winer, and Weaire (WWW), which has been the basis of the best CRNs generated to date [18,39]. The original WWW algorithm was described in Chapter 2. Another method to generate CRNs is reverse Monte Carlo, see for example Ref. [60] for results of a CRN consisting of 1728 atoms.

We begin to describe a number of improvements made to the original WWW algorithm by Barkema and Mousseau in 1999 [12]. These improvements accelerate the relaxation by two orders of magnitude or more. Both the original and the improved WWW algorithm, however, scale poorly with system size, since the computational effort per attempted local atomic rearrangement increases linearly with system size. We introduce local force and energy evaluations and improve the scaling of computation time with system size N significantly, namely to a constant per attempted move plus $O(N)$ per accepted move. The significance of these improvements is demonstrated by generating 10,000-atom and 20,000-atom CRNs for amorphous silicon and one 60,000-atom CRN for vitreous silica. We then discuss the structural and electronic properties of these models and conclude with an outlook on future research, aiming towards the generation of device-size atomic networks.

4.2 The improved WWW algorithm

The WWW algorithm in its original form is capable of producing high-quality amorphous networks containing of the order of a thousand atoms; it is not well suited to generate much larger networks. This is mostly due to the fact that for each proposed bond transposition, about one hundred energy and force calculations are required, each scaling as $O(N)$ with system size N. These $O(N)$ operations are the bottleneck of the algorithm.

In 1999, Barkema and Mousseau (BM) presented a number of modifications to the original WWW algorithm, partially aimed at resolving these poor scaling properties [12]. Their modifications are summarized below:

1. Starting point for the relaxation in this case is a truly random configuration whereby the atoms are placed at random locations in a periodic box at the

crystalline density. This guarantees that the resulting network is not contaminated by some memory of the crystalline state. The details of this procedure are described in Section 4.4.

2. After a bond transposition in the original WWW approach, the structure is always completely quenched, i.e., all the atomic coordinates are fully relaxed. After the quench, the bond transposition is either accepted or rejected based on the Metropolis probability. In contrast, BM determine a threshold energy before quenching. During the quench the final quenched energy is continuously estimated. Relaxation is stopped when it becomes clear that the threshold energy cannot be reached so that the bond transposition will eventually have to be rejected. This leads to a large reduction in the number of force evaluations associated with rejected bond transpositions.

3. A local relaxation procedure is used whenever possible. Immediately after a bond transposition, only a small cluster of atoms in the model experiences a significant force. This cluster consists of the atoms directly involved in the bond transposition (marked $\{A, B, C, D\}$ in Figure 2.3) and of nearby atoms, typically up to the fourth neighbor shell of the four transposition atoms. The number of atoms in such a cluster is about 80. It therefore suffices to calculate the force *locally* (i.e., only for the 80 or so atoms inside the cluster) rather than *globally* (i.e., for all the atoms in the model).

   Calculating the force on a cluster of atoms is an $O(1)$ operation, which means that it is independent of the total system size. Local force calculations are therefore much cheaper than global $O(N)$ force calculations. By using a local relaxation scheme BM increased the efficiency of the algorithm significantly. Still, to make the final accept/reject decision on the proposed move, the total Keating energy of the system has to be calculated, which is again an $O(N)$ operation. In practice, a switch must be made from local to global relaxation, usually after about ten local relaxation steps.

4. The zero temperature case is treated specifically.

Using the improved WWW algorithm, Barkema and Mousseau generated two 1000-atom models with bond angle deviations as low as 9.20 degrees [12]. Furthermore, using the same algorithm they generated a 4096-atom model with an angular deviation of 9.89 degrees. Also, Nakhmanson *et al.* generated paracrystalline models [61], which are amorphous structures with embedded crystalline grains. All models show structural and electronic properties in excellent agreement with experiments.

4.3 A scalable WWW algorithm

While the improved WWW algorithm can successfully generate networks containing several thousand particles, it does not deal well with systems of 10,000 particles or more. Each attempted bond transposition still requires one or more $O(N)$ operations. In this section, we present an algorithm for attempting bond transpositions that is local, i.e., free of $O(N)$ operations for unsuccessful bond transpositions.

4.3.1 Local energy and force evaluations

To exploit the local nature of the bond transpositions, we need to introduce the concept of local energy: we assign to each atom i an energy ϵ_i such that $E = \sum_{i=1}^{N} \epsilon_i$ with E the Keating energy of the system given by Eq. (2.1). One way to achieve this is to divide the energy due to two-body interactions equally between the two participating atoms and to assign the energy of three-body interactions to the central atom of the corresponding triple. Thus, we obtain:

$$\epsilon_i \equiv \sum_{j=1}^{4} \left[\frac{1}{2} \frac{3}{16} \frac{\alpha}{d^2} \left(\vec{r}_j \cdot \vec{r}_j - d^2 \right)^2 + \sum_{k=j+1}^{4} \frac{3}{8} \frac{\beta}{d^2} \left(\vec{r}_j \cdot \vec{r}_k + \frac{1}{3} d^2 \right)^2 \right]. \tag{4.1}$$

Here, the constants α, β, and d are defined as in Eq. (2.1); $\vec{r}_j$ represents the vector pointing in the direction of the j-th bond away from atom i with atom i in the origin. The energy E_C of a cluster C of atoms can now be calculated using:

$$E_C = \sum_{i \in C} \epsilon_i . \tag{4.2}$$

The force on the atoms inside the cluster is obtained from the derivatives of the Keating energy with respect to the atomic coordinates. Care has to be taken for atoms on the edge of the cluster since these atoms also interact with atoms outside the cluster: due to the two- and three-body terms in the Keating potential, all atoms interact with their first and second nearest neighbors; for atoms located on the edge of the cluster, some of these neighbors are outside the cluster.

4.3.2 Local WWW moves

Starting point is a random configuration generated using one of the methods described in Ref. [12] or Section 4.4. This guarantees that the resulting configurations are not contaminated by some memory of the crystalline state. Assuming that the total Keating energy of the initial configuration is known and equals E, WWW moves can be attempted locally as follows:

1. A threshold energy E_t is determined by using the equation:

$$E_t = E - k_B T \ln(1 - r), \tag{4.3}$$

where r is a random number uniformly drawn from the interval $[0, 1\rangle$. The move is accepted if the attempted bond transposition leads to a configurational energy below the threshold energy; otherwise it is rejected.

2. The four atoms involved in the attempted bond transposition and all atoms up to the fourth neighbor shells of these four atoms are grouped into a cluster. These atoms, about 80, are allowed to move. Also the atoms in the fifth neighbor shell are included in the cluster since their local energies may change. These atoms, about 70, are not allowed to move. Note that atoms in the sixth neighbor shell do not contribute to the energy of the cluster, only to the force on some atoms in the cluster.

3. A list is constructed of all the bonds that contribute to the force on the atoms inside the cluster. As was explained above, some of these bonds involve atoms outside the cluster. For each bond we store the labels of the two atoms constituting the bond, the x, y, and z components of the bond vector (taking care of the periodic boundary conditions), and the square of the bond length. We then calculate the cluster energy E_C using Eq. (4.2). In the calculation of the cluster energy most bonds are encountered more than once. To increase efficiency, a bond (i.e., its set of three components) is calculated only once during an energy or force evaluation; once a bond has been calculated the bond information is stored. Later references to the same bond are then retrieved from memory.

   We also store the energy of the atoms that remain outside the cluster: $E_r \equiv E - E_C$. We then perform the bond transposition to obtain the geometry shown in the right frame of Figure 2.3.

4. The system is relaxed locally, i.e., only atoms inside the cluster are allowed to move. At each relaxation step we use Eq. (4.2) to calculate the energy of the cluster E_C and the atomic forces, again making sure each bond is calculated only once, and perform structural relaxation as in the original and improved WWW algorithms. At each relaxation step the total energy of the system is equal to $E = E_r + E_C$. Local relaxation is continued until the energy has converged or until it becomes clear that the threshold energy cannot be reached.

In the local relaxation procedure above, the computational effort per attempted bond transposition does not grow with the system size. Local relaxation alone, however, is not sufficient and we also have to relax globally to relieve any strain that may have built up between atoms on the edge of a cluster and non-cluster atoms. For

clusters extending up to the fourth neighbor shell around the atoms directly involved in the bond transposition we find that global relaxation can lower the configurational energy typically by less than 0.1 eV. We therefore switch from local to global relaxation when, during local relaxation, the energy comes to within 0.1 eV of the threshold energy. In most cases, this leads to the move being accepted.

4.4 Random initial configurations

It is important that the starting configuration for any of the WWW algorithms (original, improved or scalable) is random. In the original WWW algorithm, a random configuration is obtained from the crystalline structure which is randomized by a large number of bond transpositions. This essentially means using a high temperature in the Metropolis probability such that each proposed bond transposition is accepted. Although easy to implement, this method has the disadvantage that the resulting network may have some memory of the crystalline phase left if not randomized long enough. It is not altogether clear how long randomization should continue in order to erase the crystal structure completely. This is a serious problem because realistic amorphous structures should be free from any crystalline regions by definition.

The method used in the improved WWW algorithm [12] starts with a structure that is truly random, i.e. not derived from the crystalline phase. To generate such a structure, the atoms are placed at random locations in the cubic simulation volume at the crystalline density with periodic boundary conditions, under the constraint that no two atoms be closer than 2.3 Å. The tricky part is then to generate the list of bonds in order to obtain a four-fold coordinated network. Ideally, if two atoms are close together, a bond should be present between them in the list of bonds. This is achieved by constructing a loop visiting four atoms such that each pair of neighbors along the loop is not separated by more than a distance r_c. The loop is then gradually expanded until it visits each atom exactly twice; the edges of the loop are then the bonds in the network. The expansion of the loop is achieved by randomly selecting a group of three atoms $\{A, B, C\}$, such that A is at most two-fold coordinated and within a distance r_c of B and C but not bonded to either, while B and C are bonded. Next, bond $B-C$ is replaced by bonds $A-B$ and $A-C$. The procedure is illustrated in Figure 4.1. This process typically leads to a CRN with rms angular deviation in the order of 30 degrees after one single minimization of the energy.

We have investigated one additional method to generate initial random configurations. This approach is based on the Voronoi diagram [62] of a set of points. In three dimensions, the Voronoi diagram of a set of points in general position is a four-fold coordinated network, which is exactly the bonding requirement for silicon atoms. The method we propose to generate an initial random structure is therefore to randomly select a number of positions in the simulation volume and to determine the

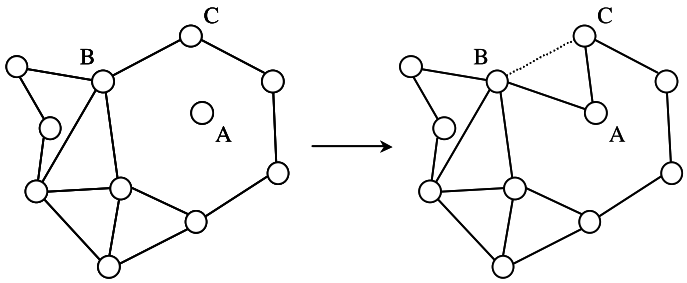

Figure 4.1: One step in the loop expansion. Three atoms $\{A, B, C\}$ are selected, of which B and C are bonded, while A is bonded to neither B nor C, and of which A is not four-fold coordinated. The bond $B - C$ is then replaced by bonds $A - B$ and $A - C$, resulting in the geometry shown right.

corresponding Voronoi diagram of these positions.

Periodic boundary conditions are imposed following the procedure outlined in Figure 4.2. For ease of illustration we show here the two-dimensional variant. In two dimensions, the Voronoi diagram yields a three-fold coordinated network. To generate a random three-fold coordinated network we select N random locations in the simulation cell. We then generate a super-cell consisting of the simulation cell itself plus its nearest periodic images. The top frame of Figure 4.2 shows the super-cell for $N = 5$ points; the simulation cell itself is marked **A**, the random points are marked with crosses. In two dimensions, the super-cell thus contains a total of $9N$ points; in three dimensions it would contain $27N$ points. Next, we determine the Voronoi diagram of the super-cell using existing software, see for example Refs. [63, 64]. In the lower frame of Figure 4.2 we show the Voronoi diagram of the super-cell in the region around **A**. The original random points are again marked as crosses but note that they are no longer required. After all, the network is formed by the Voronoi vertices. Periodic boundary conditions are imposed by identifying the neighbors of each Voronoi vertex inside **A**. In Figure 4.2, for example, vertex a is bonded to the vertices b, c and d. However, vertex c is *outside* the simulation cell **A**. Therefore, a is instead bonded to the periodic image of c *inside* **A**, which is labeled c'. In a similar fashion we find that vertex e is bonded to f'.

The above approach allows for the generation of an initial network that is completely random. It has the additional advantage over the other two methods that the unphysical "crossing" of bonds does not occur. An example of a two dimensional random network generated in this way is shown in the lower frame of Figure 1.1. Although harder to visualize, the method is equally applicable in three dimensions. In this case, four-fold coordinated CRNs with angular deviations in the order of 23 degrees (after a single minimization of the energy) are readily produced.

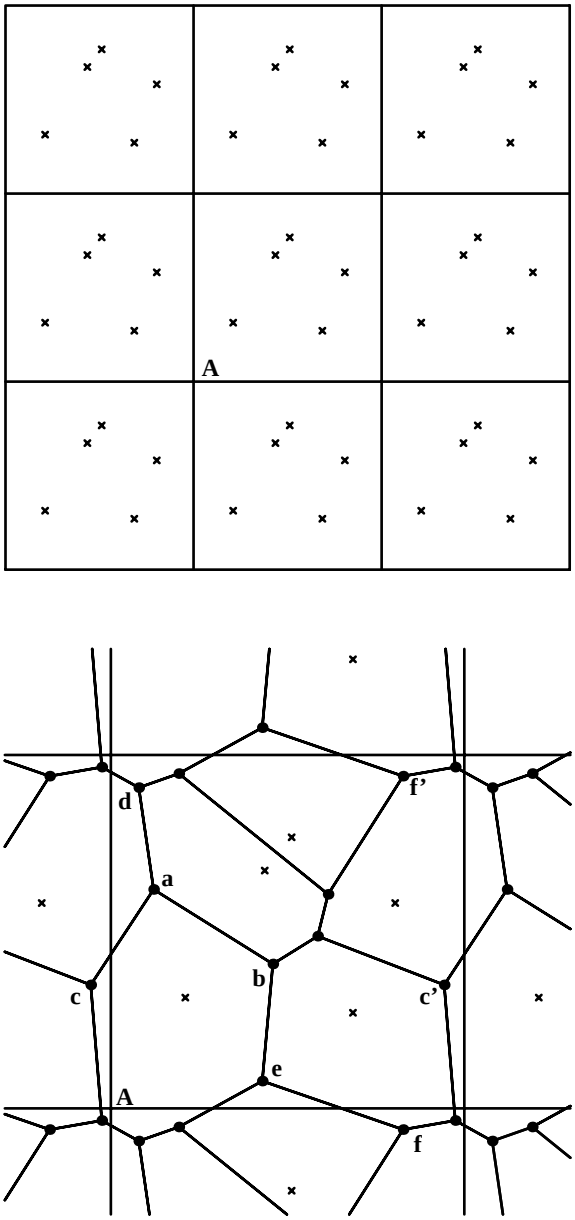

Figure 4.2: Imposing periodic boundary conditions in two dimensions. The top frame shows the simulation super-cell constructed following the method described in the text. The lower frame shows the Voronoi diagram of the super-cell around the region labeled **A**.

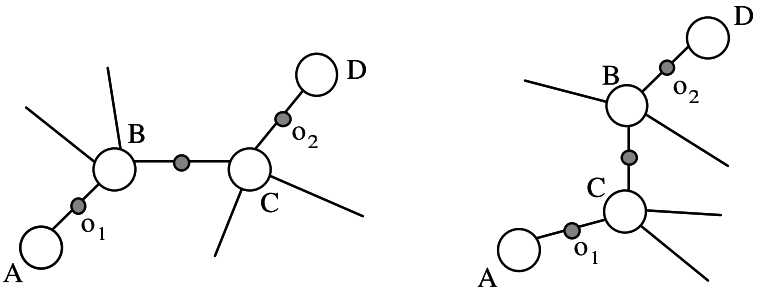

Figure 4.3: Extended bond transposition used for the generation of vitreous silica structures. Four silicon atoms $\{A, B, C, D\}$ and two oxygen atoms $\{o_1, o_2\}$ are selected following the geometry shown left. Next, bonds $B-o_1$ and $C-o_2$ are broken and two new bonds $B-o_2$ and $C-o_1$ are created to obtain the geometry shown right.

4.5 Extension to silica

The scalable WWW algorithm is easily modified to generate networks of vitreous silica. In this case, the CRN consists of N silicon atoms and $2N$ oxygen atoms. In the list of bonds, each silicon atom is bonded to four oxygen atoms, and each oxygen atom to two silicon atoms. The evolution of the network consists of extended bond transpositions illustrated in Figure 4.3.

Energy and forces can be calculated using a simple potential like the one by Tu and Tersoff [65]. Similar to the Keating potential [22] for silicon, the Tu-Tersoff potential also requires an explicit list of bonds. The functional form of the potential is given by:

$$E = \frac{1}{2}\sum_i k_b(b_i - b_0)^2 + \frac{1}{2}\sum_{i,j} k_\theta(\cos\theta_{ij} - \cos\theta_0)^2, \tag{4.4}$$

where the summation is on all silicon-oxygen bonds Si-O in the list of bonds. Here, i represents the i-th bond and b_i its length; θ_{ij} is the angle between bonds i and j to a common atom. The potential parameters for the two-body Si-O interaction are given by $k_b = 27.0$ eV and $b_0 = 1.60$ Å. For the three-body O-Si-O interaction common values are $k_\theta = 4.32$ eV and $\cos\theta_0 = -1/3$; for Si-O-Si interactions these values are $k_\theta = 0.75$ eV and $\cos\theta_0 = -1$.

The local energy of a single atom is defined in the usual way by dividing the energy due to two-body interactions equally between the two participating atoms and to assign the energy of three-body interactions to the central atom of the corresponding

triple. For the Tu-Tersoff potential the analogue of Eq. (4.1) thus becomes:

$$\epsilon_i \equiv \sum_{j=1}^{n_i} \left[\frac{1}{4} k_b (b_j - b_0)^2 + \sum_{k=j+1}^{n_i} \frac{k_i}{2} (\cos\theta_{jk} - \cos\theta_i)^2 \right], \tag{4.5}$$

where the summation is on all bonds involving atom i. For silicon atoms $n_i = 4$, $k_i = 4.32$ eV and $\cos\theta_i = -1/3$; for oxygen atoms $n_i = 2$, $k_i = 0.75$ eV and $\cos\theta_i = -1$.

We have developed code to generate structures of vitreous silica using the extended bond transposition of Figure 4.3, the Tu-Tersoff potential and all the optimizations of the scalable WWW algorithm. This code can generate silica structures containing as many as 60,000 atoms. Starting configurations are easily obtained from any amorphous silicon structure by placing one oxygen atom on each Si-Si bond.

4.6 Results

We have used the scalable WWW algorithm to generate structures of amorphous silicon and vitreous silica. Here we discuss the properties of these structures.

4.6.1 amorphous silicon

We have generated one 10,000-atom amorphous silicon network and one 20,000-atom network. In Table 4.1, we compare our configurations relaxed with the Keating potential with those of Djordjević, Thorpe, and Wooten [39] and with models generated by Barkema and Mousseau using the improved WWW algorithm [12]. We also provide irreducible ring statistics.

Table 4.1 shows that the strain per atom for the 10,000-atom and 20,000-atom models is significantly lower than that of the DTW models. Compared to the 1000-atom model prepared with the improved WWW algorithm (BM1000) we find that the strain per atom in the 10,000-atom and 20,000-atom models is only slightly higher, thus clearly demonstrating the efficiency of the scalable WWW approach.

An important quantity that can be compared with experiment is the width of the bond angle distribution $\Delta\theta$. Experimentally, this quantity can be extracted from the RDF [3, 4] or the Raman spectrum [66, 67]. The most recent measurement, obtained from the RDF, yields 10.45 degrees for as-implanted samples and 9.63 degrees for annealed samples [4]. The bond angle distributions of the 10,000-atom and 20,000-atom models generated by us are in good agreement with these experimental values.

Although the Keating potential already produces high-quality networks by itself, it is important to check the stability of these networks when relaxed with a more realistic interaction potential that does not require a pre-set list of neighbors. For this

Table 4.1: Energetic and structural properties of models relaxed with the Keating potential. The first two models, DTW4096a and DTW4096b, are the 4096-atom models described in Ref. [39] and refer, respectively, to a model with and without four-membered rings. Configuration BM1000 is a 1000-atom configuration prepared by Barkema and Mousseau using the improved WWW algorithm and BM4096 is a 4096-atom model prepared in the same way [12]. Configurations '10k' and '20k' represent, respectively, 10,000-atom and 20,000-atom models prepared using the scalable WWW algorithm described in the text. The ring statistics are for irreducible rings only and ρ_0 is based on $d = 2.35$ Å.

	DTW4096a	DTW4096b	BM1000	BM4096	10k	20k
E (eV/atom)	0.336	0.367	0.267	0.304	0.301	0.286
ρ/ρ_0	1.000	1.000	1.043	1.051	1.054	1.042
$\langle r \rangle / d$	0.996	0.997	0.982	0.980	0.980	0.981
$\langle \theta \rangle$	109.24	109.25	109.30	109.28	109.28	109.25
$\Delta\theta$	10.51	11.02	9.21	9.89	9.88	9.63
rings/atom						
4	0.015	0.000	0.000	0.000	0.000	0.020
5	0.491	0.523	0.472	0.490	0.480	0.456
6	0.698	0.676	0.761	0.739	0.742	0.759
7	0.484	0.462	0.507	0.467	0.512	0.501
8	0.156	0.164	0.125	0.148	0.142	0.149
9			0.034	0.035	0.034	0.039

Table 4.2: Structural properties of configurations after relaxation with the modified Stillinger-Weber (mSW) potential. The total ring number per atom (including reducible rings) is also reported, as well as the energy after relaxation with the original Stillinger-Weber (SW) potential.

	BM1000	BM4096	10k	20k
E (eV/atom, mSW)	-4.026	-3.990	-3.994	-4.008
E (eV/atom, SW)	-4.126	-4.106	-4.109	-4.116
ρ/ρ_0	0.947	0.936	0.938	0.933
$\langle r \rangle / d$	1.018	1.020	1.021	1.020
$\langle \theta \rangle$	109.25	109.20	109.19	109.20
$\Delta\theta$	9.77	10.51	10.54	10.18
rings/atom				
4	0.000	0.001	0.003	0.020
5	0.472	0.489	0.481	0.456
6	0.840	0.830	0.844	0.843
7	1.011	0.979	1.034	1.020
8	2.025	2.064	2.038	2.018

purpose we use the Stillinger-Weber (SW) potential [6] but with an enhanced angular force: the three-body term is increased by 50% with respect to the two-body term. This ad-hoc modification was shown to produce good structural properties for amorphous silicon [23, 25, 32, 68, 69] and has also been used in Chapter 3. The properties of the networks after relaxation with the (modified) SW potential are reported in Table 4.2. For all configurations, the bond angle distribution widens and the density decreases.

Figure 4.4 shows the pair correlation function for the 10,000-atom and 20,000-atom models compared to the experimental pair correlation function obtained by Laaziri *et al.* on annealed *a*-Si samples prepared by ion bombardment [4]. Agreement is excellent. However, configurations differing widely in topology can easily produce similar pair correlation functions. Agreement with the experimental pair correlation function must therefore be regarded as a minimum demand on a high-quality CRN.

A more stringent criterion that can be used to evaluate the quality of a model is the average coordination number of the atoms. Using the minimum of the pair correlation function between the first and second neighbor peak as the nearest neighbor cut-off distance (at $r \approx 3.10$ Å) and after relaxation with the modified Stillinger-Weber potential, the 10,000-atom model develops 1.08% of atoms with three or five neighbors. For the 20,000-atom model this percentage is 0.24%. The ratio of the number of three-fold coordinated atoms to the number of five-fold coordinated atoms

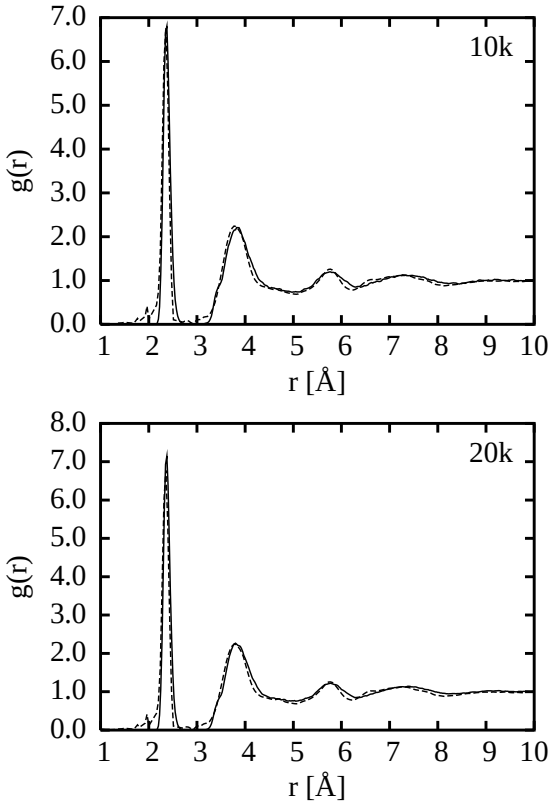

Figure 4.4: Pair correlation function for the 10,000-atom model (top) and the 20,000-atom model (bottom) after relaxation with the modified Stillinger-Weber potential (solid line). The dashed line shows the experimental result from Ref. [4]; distances are in Å.

is sensitive to the precise value of the nearest-neighbor cut-off; a smaller cut-off decreases the number of five-folds, while increasing the number of three-folds. With the cut-off used here, the 10,000-atom model contains 0.13% of three-fold coordinated atoms and 0.95% of five-fold coordinated atoms. For the 20,000-atom model these percentages are 0.07% and 0.17%, respectively.

While structural averages provide good insight into the overall quality of a model, they do not say much regarding local environments. It is therefore also important to look at the electronic properties of our models: even small densities of highly strained geometries or defects will be picked up as states in the gap of the electronic density of states (EDOS). In Figure 4.5 we show the EDOS of the 10,000-atom and 20,000-atom models. The *Fireball* local-basis ab-initio code [8] was used to obtain the EDOS. A remarkable feature of the state densities shown here is the absence of states in the gap, leading to a perfect gap of 1.3 eV for both models.

4.6.2 vitreous silica

We have also generated one 60,000-atom structure of vitreous silica using the silica-adapted WWW algorithm. As starting configuration we used the 20,000-atom amorphous silicon structure labeled '20k' from the previous section and placed oxygen atoms on the Si-Si bonds. We then scaled the simulation volume to obtain the experimental density of vitreous silica $\rho \approx 2.2$ g cm^{-3}. This configuration was evolved further with approximately one million attempted bond transpositions (using the Tu-Tersoff potential), after which the energy did not decrease significantly anymore. The resulting configuration was then quenched with the more realistic BKS potential [70] (including volume optimization) which is often used to model the atomic interactions in silica networks. The BKS potential contains a Coulomb term, an exponential term and a van der Waals term:

$$V = \sum_{i<j} \frac{q_i q_j}{r_{ij}} + A_{ij} \exp\left(-B_{ij} r_{ij}\right) - \frac{C_{ij}}{r_{ij}^6}, \tag{4.6}$$

where the sum is on all pairs of atoms in the system, r_{ij} is the distance between atoms i and j, and q_i is the charge of atom i. The values of the potential parameters A_{ij}, B_{ij} and C_{ij} are listed in Ref. [2]. The long-range Coulomb and van der Waals interactions were computed using the fast multipole code developed at Duke University [71]; the short-range exponential term was truncated and shifted at $r_c = 5.50$ Å. Using the above parameters, the BKS energy of the quenched network was found to be $E = -58.10$ eV per silicon atom. For comparison, the BKS energy of the silica β-cristobalite crystal structure is $E = -58.26$ eV per silicon atom.

Next, we investigate the structural properties of the quenched network. In Figure 4.6 we show the species-dependent RDFs. The Si-O RDF shown in the middle frame of Figure 4.6 has a well-defined peak at around $r = 1.60$ Å. Using a cut-off

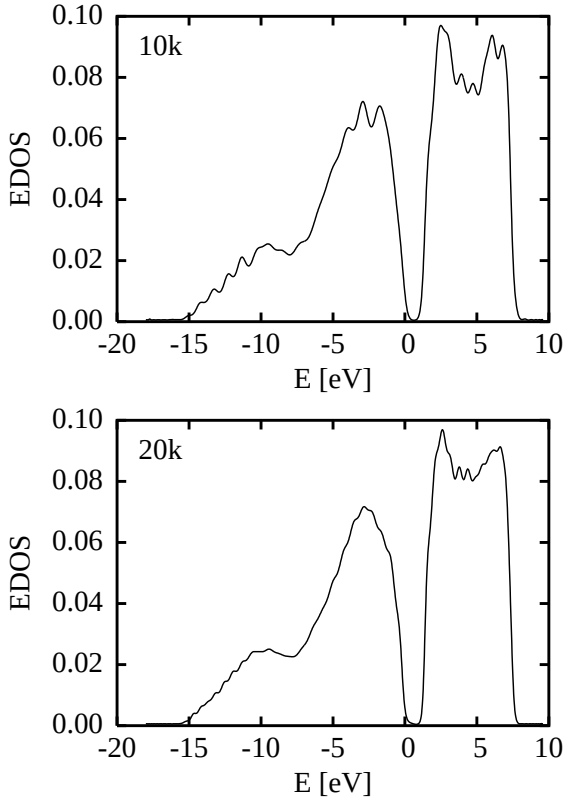

Figure 4.5: Amorphous silicon electronic density of states for the 10,000-atom model (top) and the 20,000-atom model (bottom) as obtained by Drabold with ab-initio tight-binding [8].

Table 4.3: Comparison of the 60,000-atom WWW prepared silica structure to MD and experiment. The MD data was taken from Ref. [2]. The number of atoms in each structure is given by N; ρ is the density in g cm^{-3}; the mean O-Si-O and Si-O-Si bond angles are given in degrees, with the full width at half maximum of the respective bond angle distribution in parentheses; z_4 is the percentage of perfectly coordinated silicon atoms; z_2 is the percentage of perfectly coordinated oxygen atoms.

	WWW	MD	Experiment
N	60000	1002	–
ρ	2.25	2.27-2.38	2.2
O-Si-O	109.4 (9.6)	108.3 (12.8)	109.4[a]
Si-O-Si	151.2 (33)	152 (35.7)	142 (26)[b]
z_4	100.00 %	99.8 %	–
z_2	100.00 %	99.8 %	–

[a] see Ref. [72]
[b] see Ref. [73]

$r_c = 1.80$ Å taken at the minimum between the first and second neighbor peaks in the Si-O RDF, we obtain bond angles as reported in Table 4.3. For comparison we also show results obtained with MD and in experiments, when these were available.

The properties of the WWW structure agree well with experiment. Compared to MD, the WWW structure is better relaxed (even though it is almost 60 times larger) as is evident from the smaller variations in the bond angles. Moreover, the WWW structure is almost defect free.

4.7 Summary and conclusion

We have presented here a scalable version of the WWW algorithm which allows for local atomic rearrangements to be tried with only $O(1)$ operations. The scalable performance of the algorithm has been demonstrated by the generation of one 10,000-atom and one 20,000-atom model of amorphous silicon and one 60,000-atom model of vitreous silica. Structural properties of these models are excellent and they compare well to experiments.

These high-quality models have the long term goal of accurately modeling devices such as solar cells. At this point, using periodic-boundary conditions in the two extended directions, we are able to simulate *a*-Si films with a thickness of about 1000 Å. Once such atomic configurations become available, the role of various structural and electronic defects can be studied. In Chapter 7 we present a new technique

to determine the configurational entropy of the networks discussed here.

Acknowledgements

We thank David Drabold for communicating to us the EDOS of the 10,000-atom and 20,000-atom amorphous silicon models.

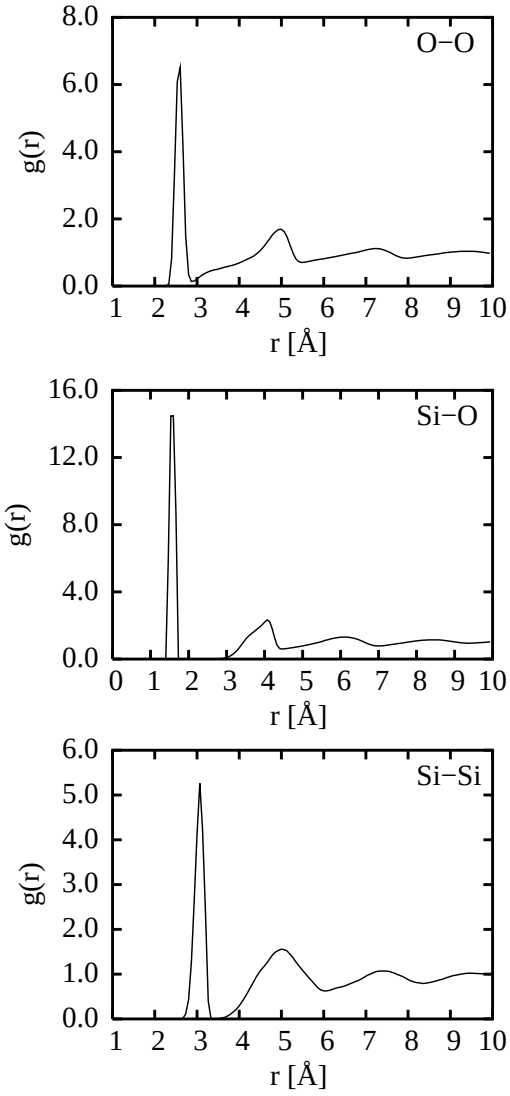

Figure 4.6: Species-dependent radial distribution function $g(r)$ for the 60,000-atom vitreous silica structure after relaxation with the BKS potential [70].

Chapter 5

Fitting the Stillinger-Weber Potential

In this chapter we describe a number of modifications to the Stillinger-Weber (SW) potential, an empirical interaction potential for silicon. The modifications are specifically intended to improve the description of the amorphous phase of silicon and are obtained by a direct fit to the amorphous structure. The potential is adjusted to reproduce the location of the transverse optic (TO) and transverse acoustic (TA) peaks of the vibrational density of states, properties insensitive to the details of experimental preparation. These modifications also lead to excellent agreement with structural properties. Comparison with other empirical potentials shows that amorphous silicon configurations generated with the modified potential have overall better vibrational and structural properties. In Chapter 6, we will use the modified SW potential presented here to model the Raman response of amorphous silicon.

This chapter is based on R.L.C. Vink, G.T. Barkema, W.F. van der Weg, and N. Mousseau, *Fitting the Stillinger-Weber potential to amorphous silicon*, J. Non-Cryst. Solids **282**, 248 (2001).

5.1 Introduction

In the past, various empirical potentials [6, 22, 38, 74–79] have been proposed to describe the different phases of silicon. A number of these empirical potentials [6,74, 75,77] were tested and compared to each other and experiments in review articles [21, 31, 80]. The general conclusion of these reviews is that it is difficult to reproduce accurately with a single empirical potential the crystalline, amorphous and liquid phases of silicon. Since atomic configurations are readily obtained in the liquid and crystalline phases of silicon, their structural and electronic properties are typically used as input for fitting the parameters of the potential, with as consequence that the

amorphous phase is generally less well reproduced.

Recent advances in the method of simulation have made it possible to generate efficiently well-relaxed configurations of *a*-Si that are insensitive to their history of preparation [23]. This allows us to fit a potential directly to the amorphous phase.

In this chapter we present a new fitting procedure and use it to generate such an empirical potential. This potential should accurately reproduce the structural and elastic properties of the amorphous phase of silicon and serve as a basis for direct comparison to experiments. To this end, we start with the Stillinger-Weber potential [6] and modify some of its parameters in order to achieve good agreement with experimental data. More specifically, we concentrate on the location of the transverse acoustic (TA) and transverse optic (TO) peaks of the vibrational density of states (VDOS)—quantities that are found to be relatively insensitive to the experimental method of preparation—as well as on a number of structural properties such as the radial distribution function and the bond angle distribution. This approach is similar in spirit to the one followed by Ding and Andersen for the generation of an empirical potential for *a*-Ge [68]. As it turns out, within our fitting procedure, a correct description of the positions of the TA and TO peaks is sufficient to ensure good structural properties.

The approach we use is as follows. First, we present the Stillinger-Weber potential and outline the procedure followed in the preparation of the amorphous configurations. Based on these configurations, we adjust the parameters of the potential to obtain the experimental positions of the TA and TO peaks of the VDOS. Finally, the structural and elastic properties of amorphous silicon resulting from the modified potential are compared to experiment, and to those resulting from the standard SW potential and from the environment-dependent interaction potential (EDIP) of Bazant *et al.* [38, 78, 79].

5.2 The Stillinger-Weber potential

In 1985, Stillinger and Weber proposed a potential for silicon with a two and three-body part [6]. The functional form of this potential was already given in Chapter 2, see Eq. (2.2) and also Table 2.1 for the potential parameters. The parameters listed in Table 2.1 were obtained from fitting to the crystalline and liquid phases of silicon. For *a*-Si, these parameters lead to a high-density liquid-like structure which is characterized by a shoulder on the second-neighbor peak of the radial distribution function (RDF) and a large fraction of overcoordinated atoms [23, 69], not observed in experiments. A common ad-hoc modification to alleviate these problems is to boost the three-body term by 50% to 100%, see for instance Refs. [23, 69]. This modification yields samples with a RDF in agreement with experiments.

5.3 Generating amorphous structures

To generate amorphous configurations, we proceed using the activation-relaxation technique (ART) as in Refs. [23,32,33] and a Stillinger-Weber potential with a three-body interaction enhanced by 50%. This follows a common ad-hoc prescription to avoid the large number of over-coordinated atoms produced by the standard SW potential: boosting the three-body term by 50% to 100% generally yields samples with structural properties in good agreement with experiment [23, 69]. The overall procedure is as follows:

1. Initially, 1000 atoms are placed at random positions in cubic cell with periodic boundary conditions. The configuration is then brought to a local energy minimum at zero pressure.

2. The configurational energy is lowered further using ART. One ART move consists of two steps: (1) the sample is brought from a local energy minimum to a nearby saddle-point (activation), and (2) then relaxed to a new minimum with a local energy minimization scheme including volume optimization, at zero pressure. The new minimum is accepted with a Metropolis probability at a ficticious temperature $T = 0.25$ eV. The relaxation phase is stopped after approximately five ART moves per atom, when the energy has reached a plateau.

3. We continue to apply ART, storing one sample every 250 ART moves, collecting a total of 20 configurations.

This procedure is repeated seven times, generating seven statistically independent sets of 20 correlated configurations. As was shown in previous studies [23, 32], this approach yields structures in good agreement with experiment: the models display a low density of coordination defects, a narrow bond angle distribution and an excellent overlap with experimental RDF. With this set of models, it is now possible to refit the Stillinger-Weber parameters to the amorphous phase.

5.4 The modified potential

Many properties of the interaction between silicon atoms are already captured by existing empirical potentials such as the SW potential. It should therefore be possible to optimize these potentials to the amorphous phase with only minor modifications.

Information on structural and elastic properties of amorphous silicon can be obtained from a wide variety of experiments, such as neutron and x-ray scattering, Raman scattering, electron-spin resonance, and x-ray photo-absorption. Extracting a detailed picture of the atomic interactions from these experiments, however, is not

straightforward. Most of these measurements do not provide direct microscopic information but rather properties averaged over a large number of atomic environments; others are highly sensitive to the details of the sample preparation, and can thus not be used, since the experimental sample preparation cannot be directly simulated.

A convenient quantity for our purpose is the VDOS, especially the locations of the TA and TO peaks, which are not sensitive to experimental details and yet are highly sensitive to properties of the potential used since they relate to higher terms in the elasticity. In contrast to their positions, the amplitudes of these peaks vary between experiments [81].

To first order, vibrational modes located in the TA band correspond to bond bending modes while those in the TO regime are associated with bond stretching vibrations [82]. Due to the disordered nature of these materials, a significant amount of mixing makes the details of the contributions to these peak more subtle in reality.

In the SW potential, the amount of energy required to stretch a bond is determined by the strength of the two-body term, i.e. by ϵA in Eq. (2.2). The energy of bond bending is determined by the strength of the three-body term, i.e. by $\epsilon\lambda$ in Eq. (2.2). By adjusting the two prefactors ϵA and $\epsilon\lambda$, we can fit the locations of both the TA and TO peak in the calculated VDOS to experimental values. Of the three parameters A, ϵ, and λ, one is redundant; it is sufficient to vary λ to set the relative three-body strength and to choose ϵ to set the overall energy scale.

Our first aim is to adjust the ratio of the locations of the TA and TO peaks by tuning λ. For $\lambda/\lambda_0 = 1.00, 1.25, 1.50, 1.75$ and 2.00, with $\lambda_0 \equiv 21.0$, we follow the following procedure:

1. Each sample is brought to a local energy minimum at zero pressure using the SW potential with the above value for λ and the original values for the other parameters.

2. For each sample, the hessian matrix is calculated and diagonalized, resulting in the VDOS. The hessian is calculated using the SW potential with the above value for λ and the original values for the other parameters. The positions of the TA and TO peaks are recorded.

Figures 5.1a and 5.1b show the location of the TA and TO peak, respectively, as a function of λ/λ_0. While the location of the TA peak is highly sensitive to changes in λ, the location of the TO peak changes less than 2%.

Neutron scattering experiments [83] on *a*-Si yield TA and TO peaks at $\omega_{TA} = 184.8$ cm^{-1} and $\omega_{TO} = 467.6$ cm^{-1}, respectively, which gives a ratio $\omega_{TO}/\omega_{TA} = 2.53$. Figure 5.1c shows this ratio for the computer simulation, as a function of λ/λ_0. The dashed line is the experimental value. From Figure 5.1c, we see that the choice $\lambda/\lambda_0 = 1.5$ provides a fit with the experimental result and that the original choice $\lambda/\lambda_0 = 1.0$ does not reproduce experiments, as expected from earlier reports [23,69].

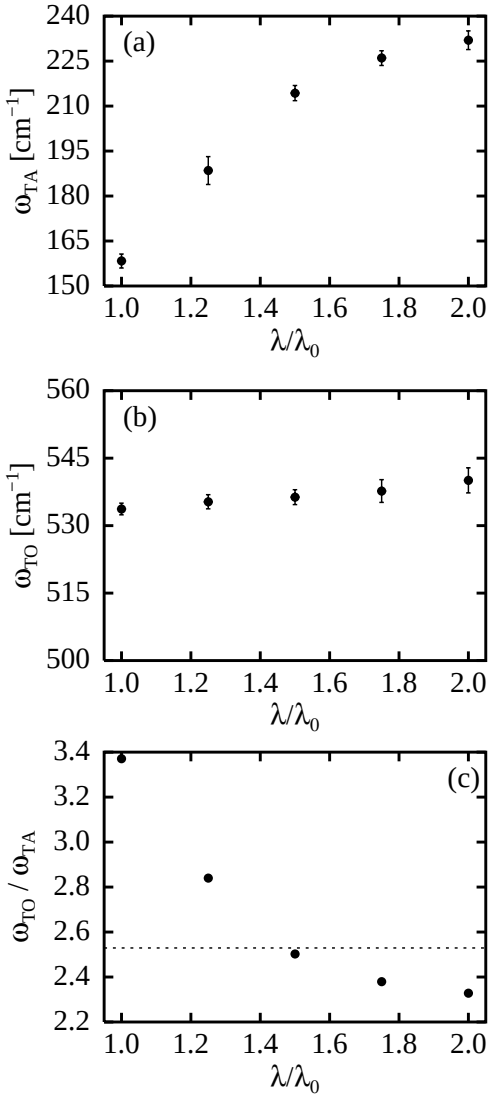

Figure 5.1: The TA peak position ω_{TA} (top) and the TO peak position ω_{TO} (middle), both in cm^{-1}, as a function of λ/λ_0. The bottom figure shows the ratio ω_{TO}/ω_{TA} as a function of λ/λ_0 obtained by computer simulation. The dashed line is the experimental value [83]. The best agreement with experiment occurs for $\lambda/\lambda_0 = 1.5$.

Table 5.1: Values of the parameters in the standard SW and the modified SW potentials.

	standard SW	modified SW
ϵ (eV)	2.16826	1.64833
A	7.049556277	7.049556277
B	0.6022245584	0.6022245584
σ (Å)	2.0951	2.0951
p	4	4
a	1.80	1.80
λ	21.0	31.5
γ	1.20	1.20

We can follow this procedure because of the overall insensitivity of the peak location to the detail of the local structure, i.e., the value of λ used in the initial relaxation of the seven independent sets of samples does not influence the curve of Figure 5.1. Using a set of samples generated with values of $\lambda = 1.40\lambda_0$ and $\lambda = 2.00\lambda_0$, we found results identical to those presented in Figure 5.1. This confirms once more the independence of the ratio of the positions of the peaks to the structural details of the models.

After fitting the three-body parameter λ, we set the overall energy scale parameter ϵ in Eq. (2.2) as follows: Figure 5.1b shows that, for $\lambda/\lambda_0 = 1.5$, $\omega_{TO} = 536.3$ cm^{-1}. The experimental value is $\omega_{TO} = 467.6$ cm^{-1}, a factor 0.87 lower. To obtain agreement with experiment, the parameter ϵ is therefore multiplied by $0.87^2 = 0.76$. The square appears because the frequencies in the VDOS are proportional to the square-root of the eigenvalues of the hessian. Thus, we have scaled the strength of the three-body interactions, governed by $\epsilon\lambda$, by a factor of 1.14, and the two-body interactions, governed by ϵA, by a factor of 0.76.

The set of parameters that we thus propose for amorphous silicon is presented in Table 5.1; for comparison the original potential parameters are also shown. As mentioned above, the 50% increase in the ratio of the three-body to the two-body term has already been proposed earlier for *a*-Ge by Ding and Andersen [68] and by many others as an ad-hoc way to obtain a realistic structure. We obtain a similar ratio following a different route: by fitting the vibrational properties of the model to experiments.

Table 5.2: Comparison of energetic and structural properties of *a*-Si obtained using SW, modified SW and EDIP. Also given are experimental values [84–88], when available. Shown are the density ρ in atoms per Å^3, the energy per atom E in eV, the mean $\langle r \rangle$ of the first neighbor distance in Å, the mean θ and the standard deviation $\Delta\theta$ of the first neighbor bond angle in degrees. Also given are the coordination defects in % and the average coordination number $\bar{Z}$.

	experiment	SW	modified SW	EDIP
ρ	0.044-0.054	0.049	0.047	0.049
E	–	-4.137	-3.072	-4.451
$\langle r \rangle$	2.34-2.36	2.38	2.37	2.37
$\langle \theta \rangle$	108.6	107.99	109.16	108.57
$\Delta\theta$	9.4-11.0	15.08	10.02	13.68
3-fold	–	0.00	0.50	0.20
4-fold	–	83.50	98.00	91.90
5-fold	–	15.60	1.50	7.80
6-fold	–	0.90	0.00	0.10
$\bar{Z}$	3.90-3.97	4.17	4.03	4.08

5.5 Measurements and comparison

We now compare the structural and elastic properties of configurations generated with the modified Stillinger-Weber potential with experiment, as well as with those of the standard version of this potential and that of the environment dependent interatomic potential (EDIP) of Bazant *et al.* [38, 78, 79], the best empirical potential now for the crystalline and liquid phase. The properties of other empirical potentials, such as Biswas-Hamann [77] and Tersoff [74], have been reviewed elsewhere [31] and shown to reproduce poorly the experimental properties of amorphous silicon.

To test these potentials, we generate a new, 1000-atom configuration following the method outlined in section 5.3 and using modified SW interactions. The structural properties of this sample are reported in Table 5.2 and Figure 5.2 and are found to be in agreement with experiment. In order to offer a better comparison to the elastic and vibrational properties of the three potentials, we use the final configuration presented here as a seed for ART using standard SW and EDIP. With each of these potentials, an additional 5000 ART moves are generated; this allows the configuration to evolve significantly away from its starting point and yields a structure optimized for that potential.

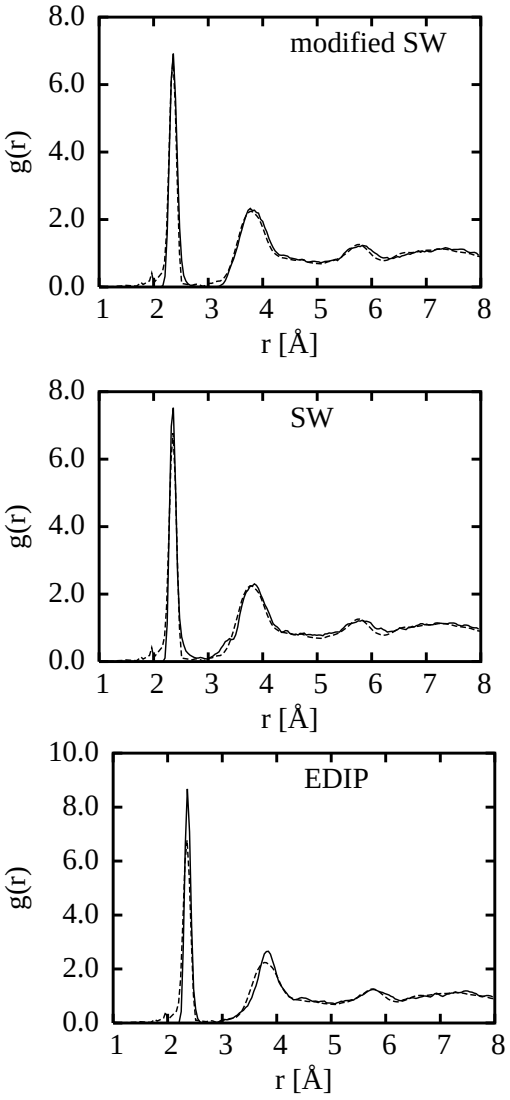

Figure 5.2: Radial distribution functions of *a*-Si. The solid curves in the above graphs show the RDF obtained in computer simulations using modified SW (top), standard SW (middle), and EDIP (bottom). In each of the graphs, the dashed curve represents the experimentally obtained RDF [3, 4]; distances are in Å.

Table 5.2 lists energetic and structural properties of these three samples. The list of nearest-neighbors is obtained by setting the cutoff distance at the minimum between the first- and second-neighbor peaks in the radial distribution function.

It is clear from this table that modified SW generates the best structure, followed by EDIP, which leads to a wider bond angle distribution and a higher number of defects (mostly over-coordinated atoms). These two factors are important, since the width of the bond angle distribution is considered a fine measure of the quality of a model and experiments have shown no indication of overcoordination in *a*-Si.

The top graph of Figure 5.2 shows the RDF for the configuration generated using modified SW interactions, together with the experimental RDF obtained from high quality *a*-Si samples prepared by ion bombardment [3, 4]. To our knowledge, this experimental RDF has the highest resolution to date. The middle and bottom graphs show the RDF obtained using standard SW and EDIP interactions, respectively.

The RDF generated with standard SW shows a shoulder on the left side of the second neighbor peak and thus fails to reproduce experiment; this shortcoming of standard SW is well-known. EDIP reproduces the experimental RDF fairly well, though not as well as modified SW does: there are substantial discrepancies with experiment in the heights of the first and second neighbor peaks. The RDF generated with modified SW interactions has the best overall experimental agreement: it reproduces the experimental first and second neighbor peak-heights and does not produce a shoulder on the second neighbor peak. It does, however, fall below the experimental curve on the left of the second neighbor peak.

As an additional check, we determine the area between the calculated and experimental RDF curves. In case of perfect experimental agreement, this area should be zero. We consider the interval from $r = 2.0$ to $r = 8.0$ Å since the fluctuations in the experimental RDF for $r < 2.0$ Å are finite-size artefacts [3, 4]. For modified SW, standard SW and EDIP, we find areas of 0.63, 0.67 and 0.84, respectively, showing that modified SW is indeed closest to experiment.

Figure 5.3 compares the experimentally obtained VDOS for *a*-Si to vibrational state densities obtained using modified SW (top), standard SW (middle) and EDIP (bottom). While standard SW and EDIP correctly reproduce the experimental TA peak frequency, the TO peak frequency exceeds the experimental value. Naturally, the modified SW potential does not suffer from this shortcoming, as it was explicitly fitted to reproduce the experimental values.

Figure 5.3 also shows that none of the potentials capture the experimental shape of the VDOS. In particular, there is large discrepancy between simulation and experiment in the TA and TO peak amplitudes. However, several studies [67, 81] have shown that the TA and TO peak amplitudes depend on defect concentration and on the degree of relaxation in the *a*-Si samples. One possible explanation for this discrepancy is therefore that the degree of relaxation in the experimental sample differs

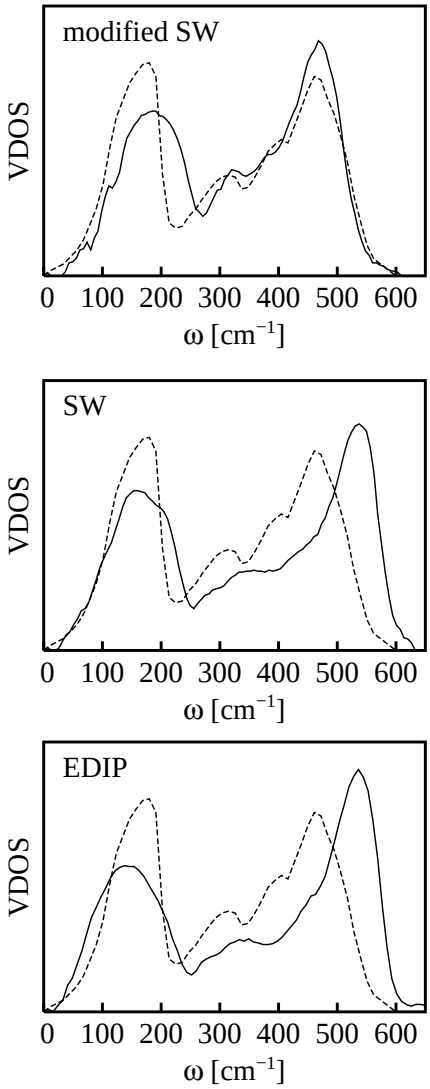

Figure 5.3: Vibrational state densities for *a*-Si. The solid curves in the above graphs show the VDOS obtained in computer simulations using modified SW (top), standard SW (middle), and EDIP (bottom). In each of the graphs, the dashed curve represents the experimentally obtained VDOS [83]. Frequencies are in cm^{-1}, the area of the VDOS is normalized.

from that of the computer generated samples used in our simulation.

As a final test, we calculate the elastic constants of *a*-Si using the various potentials. The results are summarized and compared to experiment in Table 5.3. The experimental value for the bulk modulus B is obtained from sound velocity measurements [89], where the relation $B = \rho v^2/(3(1-2\nu))$ was used, with Poisson's ratio $\nu = 0.22$, sound velocity v and density ρ. To our knowledge, no experimental values for the constants C_{ij} for *a*-Si exist. The bulk modulus for modified SW is significantly lower than for the other two potentials, in better agreement with experiment.

5.6 Conclusions

In this chapter we have presented a new set of parameters for the Stillinger-Weber potential, obtained by directly fitting to the amorphous phase, and compared the structural, elastic and vibrational properties of configurations obtained with this potential to those generated using the standard SW potential and the environment-dependent interaction potential (EDIP), two common empirical potentials.

The modified SW potential was fitted to reproduce the locations of the TA and TO peak of the experimental vibrational density of states, quantities independent of the method of preparation. This is achieved by scaling λ and ϵ by factors of 1.5 and 0.76, respectively, while keeping all other parameters fixed. Thus, we have scaled the strength of the three-body interactions, governed by $\epsilon\lambda$, by a factor of 1.14, and the two-body interactions, governed by ϵA, by a factor of 0.76.

Without any additional fitting, the modified SW potential gives structures for *a*-Si in excellent agreement with experimental results: the RDF is correctly reproduced, and the number of coordination defects and angular deviations of the generated structures are in agreement with experiment. Both the structural properties and the bulk modulus obtained with this potential are in better agreement with experiment than those generated using EDIP or the standard SW.

The modified SW potential presented here is designed to accurately describe the vibrational, as well as the structural and elastic properties of *a*-Si. This makes the potential particularly useful to model Raman and neutron scattering experiments. In Chapter 6, we will use it to study the relation between structural properties of amorphous silicon and features of the Raman spectrum, such as the narrowing of the TO peak width during relaxation, and to investigate the relation between Raman and neutron-scattering spectra.

Table 5.3: Elastic constants for *a*-Si (in Mbar) calculated using various potentials. *B* is the bulk modulus, whose experimental value was taken from Ref. [89].

	experiment	SW	modified SW	EDIP
C_{11}	–	1.31	1.23	1.30
C_{12}	–	0.71	0.47	0.81
C_{44}	–	0.32	0.48	0.56
B	0.6	0.94	0.73	0.97

Chapter 6

Raman Spectra of Amorphous Silicon

In 1985, Beeman, Tsu and Thorpe established an almost linear relation between the Raman transverse-optic (TO) peak width Γ and the spread in mean bond angle $\Delta\theta$ in amorphous silicon [66]. This relation is often used to estimate the latter quantity in experiments. In the last decade, there has been significant progress in the computer generation of amorphous silicon structures. Exploiting this progress, we present a more accurate determination of the relation between Γ and $\Delta\theta$ using 1000-atom configurations. Also investigated are the TO peak frequency ω_{TO} as a function of $\Delta\theta$, and the ratio of the intensities of the transverse-acoustic (TA) and TO peak I as a function of $\Delta\theta$. We find that, as $\Delta\theta$ decreases, the TA/TO intensity ratio decreases and the TO peak frequency increases. These relations offer additional ways to obtain structural information on amorphous silicon from Raman measurements.

The work presented in this chapter is based on R.L.C. Vink, G.T. Barkema, and W.F. van der Weg, *Raman spectra and structure of amorphous silicon*, Phys. Rev. B **63**, 115210 (2001).

6.1 Introduction

Many structural properties of amorphous silicon, such as defect concentration and variation in mean bond angle, are difficult to determine experimentally. This is because it is impossible to measure directly the coordinates of the atoms. However, important information on the structure of amorphous silicon can be obtained indirectly through a number of experimental techniques. These techniques include neutron, x-ray and Raman scattering, electron-spin resonance, and x-ray photo-absorption. We focus here on Raman measurements, which are relatively easy to perform and frequently used [90–93].

The Raman spectrum of amorphous silicon consists of two distinct bands, at about 150 cm^{-1} and 480 cm^{-1}, associated with transverse acoustic (TA) and transverse optic (TO) vibrational modes, respectively. A number of features in the Raman spectrum are highly sensitive to the structural properties of the amorphous silicon sample. For example, the width of the TO band is related to the rms Si-Si-Si bond angle variation $\Delta\theta$ [94].

In several computational studies [66, 95, 96], the relation between Γ and $\Delta\theta$ was quantified. All studies indicate a broadening of the TO peak with increasing $\Delta\theta$. Beeman's linear relation, $\Gamma = 15 + 6\Delta\theta$, which dates back to 1985, is often used by experimentalists to determine $\Delta\theta$ from Raman measurements. Here, Γ is in cm^{-1} and $\Delta\theta$ is in degrees.

Beeman derived his relation using nine structural models of amorphous silicon. Of these models, five were generated from the same 238-atom, hand-built model by Connell and Temkin [97], which contains even-membered rings only. In contrast, all simulations on amorphous silicon find an abundance of five- and seven-fold rings. Moreover, the Connell-Temkin models do not impose periodic boundary conditions and consequently contain a large fraction of surface atoms. Experimental values of $\Delta\theta$, based on the radial distribution function obtained in neutron-diffraction studies, range from 9.9 to 11.0 degrees [87]. Of the nine structural models used by Beeman, only three exhibit values of $\Delta\theta$ in this range. New techniques to generate amorphous silicon structures, such as ART [23, 24, 33], as well as more powerful computers, have made it possible to generate larger and more realistic amorphous structures via computer simulation.

Since 1985, the description of the Raman scattering process has also improved. Beeman used the bond polarizability model proposed by Alben *et al.* [98], which dates back to 1975. Characteristic for this model is the inclusion of three weighting parameters, whose values must be set somewhat arbitrarily. Several studies have indicated that the values originally proposed by Alben yield an incorrect value for the depolarization ratio [92, 93]. These studies therefore propose different weights. Since then, other polarizability models have been proposed, for example by Marinov and Zotov [82].

In this chapter we re-investigate the relation between Γ and $\Delta\theta$ via computer simulation. This simulation is based on a large number of 1000-atom configurations obeying periodic boundary conditions, with structural properties that are in excellent agreement with experiment. Furthermore, recent advances in neutron scattering techniques have made it possible to directly compare the bond polarizability models to experiment [99]; such a comparison will also be included. Additionally, we present two other methods to obtain structural information from the Raman spectrum. The TA/TO intensity ratio [90] and the location of the TO-peak [81] are both believed to be directly related to $\Delta\theta$; these relations will be quantified.

6.2 Method

To calculate Raman spectra the following ingredients are required: a potential to describe the atomic interactions in the sample, a realistic structure (i.e. a set of atomic coordinates) of amorphous silicon and a model to assign Raman activities to the vibrational eigenmodes of this structure.

In the present work, we use the modified version of the Stillinger-Weber potential described in Chapter 5 for all calculations. This potential has the same functional form as the original SW potential [6], but with different parameters fitted specifically to the amorphous phase of silicon [25].

6.2.1 Sample generation

To study the effect of $\Delta\theta$ on the Raman spectrum, we need a number of amorphous silicon structures with a range of values for $\Delta\theta$. These configurations were generated using the activation-relaxation technique (ART) [23, 24, 33]. As was shown in previous studies [23, 24], ART yields structures in good agreement with experiment. They display a low density of coordination defects, a narrow bond angle distribution and an excellent overlap with the experimental radial distribution function (RDF). The amorphous structures used here were generated as follows:

1. Initially, 1000 atoms are placed at random positions in a cubic cell with periodic boundary conditions. The configuration is then brought to a local energy minimum at zero pressure using the method of conjugate gradients.

2. The energy of the configuration is minimized further using ART. One ART move consists of two steps: (1) the sample is brought from a local energy minimum to a nearby saddle-point (activation), and (2) then relaxed to a new minimum with a local energy minimization scheme including volume optimization, at zero pressure. The new minimum is accepted with the Metropolis probability at temperature $T = 0.25$ eV.

3. Every 50 ART moves, up to approximately five ART moves per atom, the configuration is stored. For 1000-atom samples, this procedure yields a set containing 100 samples.

This procedure is repeated nine times, generating nine statistically independent sets of 100 correlated configurations each. For each set, we found that $\Delta\theta$ ranges from approximately 10 degrees for the well-relaxed configurations, to approximately 14 degrees for the poorly annealed configurations.

6.2.2 Calculation of Raman spectra

We focus on the reduced Raman spectrum $I(\omega)$, with thermal and harmonic oscillator factors removed. This spectrum is a function of frequency ω and of the form:

$$I(\omega) = C(\omega)g(\omega), \tag{6.1}$$

where $g(\omega)$ is the vibrational density of states (VDOS) and $C(\omega)$ a coupling parameter, which depends on frequency and on the polarization: horizontal-horizontal (HH) or horizontal-vertical (HV) of the incident and scattered light.

To calculate the VDOS, the hessian (matrix of second-derivatives of the potential energy with respect to the atomic positions) is calculated. Diagonalization of the hessian gives the frequencies of the vibrational modes, from which the VDOS is obtained. The function $C(\omega)$ is obtained from the polarizability tensor $\alpha(\omega)$. In terms of $\alpha(\omega)$, the coupling parameter for HH and HV Raman scattering becomes $C_{HH}(\omega_p) = 7G^2 + 45A^2$ and $C_{HV}(\omega_p) = 6G^2$, respectively, with A and G^2 given by the tensor invariants:

$$A = \frac{1}{3}\left[\alpha_{11} + \alpha_{22} + \alpha_{33}\right], \tag{6.2}$$

and:

$$\begin{aligned} G^2 &= 3\left[\alpha_{12}^2 + \alpha_{23}^2 + \alpha_{31}^2\right] \\ &+ \frac{1}{2}\left[(\alpha_{11} - \alpha_{22})^2 + (\alpha_{22} - \alpha_{33})^2 + (\alpha_{33} - \alpha_{11})^2\right], \end{aligned} \tag{6.3}$$

see for instance Ref. [100].

The form of the polarizability tensor $\alpha(\omega)$ still needs to be specified; this is the most uncertain part of the calculation. Several models have been proposed, amongst which the commonly used model of Alben *et al.* [98] and the more recent model of Marinov and Zotov [82].

In the model of Alben, a cylindrical symmetry of the individual bonds is assumed and each bond is treated independently as a homopolar, diatomic molecule. Three different forms for the bond polarizability tensor are introduced:

$$\alpha_1(\omega_p) = \sum_{l,\Delta} \vec{u}_l \cdot \vec{r}_\Delta \left[\vec{r}_\Delta \vec{r}_\Delta - \frac{1}{3}\mathbf{I}\right], \tag{6.4}$$

$$\alpha_2(\omega_p) = \sum_{l,\Delta} \vec{u}_l \cdot \vec{r}_\Delta \left[\frac{1}{2}\left(\vec{r}_\Delta \vec{u}_l + \vec{u}_l \vec{r}_\Delta\right) - \frac{1}{3}\mathbf{I}\right], \tag{6.5}$$

$$\alpha_3(\omega_p) = \sum_{l,\Delta} (\vec{u}_l \cdot \vec{r}_\Delta)\mathbf{I}. \tag{6.6}$$

Here, the summation runs over all atoms l in the sample and their nearest neighbors Δ, $\vec{r}_\Delta$ is the unit vector from the equilibrium position of atom l to the nearest neighbor

Δ, $\vec{u}_l$ is the displacement vector of atom l when it is vibrating in mode p and $\mathbf{I}$ is the unit dyadic. The total polarizability tensor α is a weighted sum of the three terms, i.e. $\alpha = B_1\alpha_1 + B_2\alpha_2 + B_3\alpha_3$. As was stated in the introduction, the precise choice of the weights B_i is somewhat arbitrary and this is the major shortcoming of the model. Several studies have indicated that mechanisms 1 and 3 provide the main contribution to the Raman scattering process; these propose to use $B_1 : B_2 : B_3$ proportional to $2 : 0 : 1$, respectively [92, 93]. In the remainder of this chapter we will use the above set of weights.

The model of Marinov and Zotov (MZ) has no free parameters. In this model, the bond polarizability is expressed as a sum of three components; two components parallel to the bond arising from bonding and non-bonding electrons and a third component perpendicular to the bond, see Ref [82]. Under these assumptions, the polarizability tensor takes the form:

$$\alpha(\omega_p) = \sum_m r_m^3 \left[\left(\vec{b}_m \cdot \vec{r}_m \right) \vec{r}_m \vec{r}_m + \frac{1}{2} \left(\vec{b}_m \vec{r}_m + \vec{r}_m \vec{b}_m \right) \right]. \tag{6.7}$$

Here, the summation runs over all bonds m in the sample, $\vec{r}_m$ is a unit vector parallel to the bond, r_m is the bond length and $\vec{b}_m$ is defined as $\vec{u}_j - \vec{u}_i$; where $\vec{u}_i$ and $\vec{u}_j$ are the displacement vectors of atoms i and j constituting the mth bond, when vibrating in mode p. For a more detailed discussion on the differences between the two polarizability models, see Ref. [82].

The coupling parameter for *a*-Si has also been determined experimentally [99] through neutron scattering methods. According to this experiment, the coupling parameter is a slowly increasing function of frequency. We will use this experimental result to test the validity of both polarizability models.

6.3 Results

First, in section 6.3.1, we compare the polarizability models of Alben and Marinov and Zotov to experiment. In the subsequent sections, we investigate the relation between the variation in the mean bond angle $\Delta\theta$ and the:

1. Raman TO peak width Γ,
2. Raman TO peak position ω_{TO},
3. Raman TO/TA intensity ratio I.

We show results for HV polarized light only; this is the usual experimental situation. Results for HH polarized light have also been obtained and are available upon request.

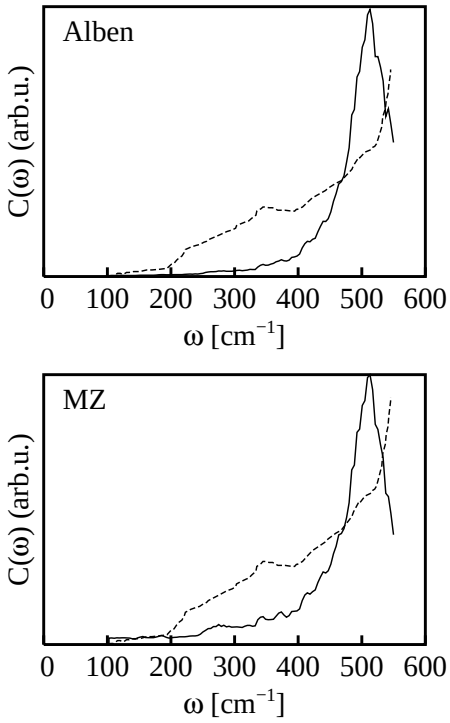

Figure 6.1: HV Raman Coupling parameter for *a*-Si calculated using the model of Alben model (top) and the MZ model (bottom). The dashed line is the experimental result taken from Ref. [99]. Frequency is in cm^{-1} and all curves are area-normalized.

6.3.1 Raman coupling parameter

The solid curves in Figure 6.1 show the HV Raman coupling parameter for *a*-Si calculated using the model of Alben (top) and the MZ model (bottom) for the bond polarizability. The experimental result of Ref. [99] is also shown (dashed). For this calculation, we used a well-annealed, 1000-atom configuration with $\Delta\theta = 10.0°$, since this will most closely resemble the experimental sample. We have checked that the general features of the curves in Figure 6.1 do not depend on the details of the configuration used: a number of other, well-annealed, configurations, with $\Delta\theta$ ranging from 10.0° to 11.0°, gave similar results.

Figure 6.1 shows that both models yield an increasing coupling parameter for frequencies up to around 500 cm^{-1}. This is in qualitative agreement with experiment. For higher frequencies, the model calculations predict a sharp decrease in the

coupling parameter. This is not confirmed by experiment.

The quantitative agreement with experiment is rather poor, especially in the low-frequency regime; both models provide substantially less activity in this regime than observed in experiment. For this reason, Raman spectra calculated using either of the two models yield TA intensities far below experimental values. This, in our opinion, is their major shortcoming.

This point is further illustrated in the top graph of Figure 6.2, where we show the Raman spectrum calculated using the MZ model (solid) and an experimental spectrum (dashed) taken from Ref. [101]. The experimental spectrum was obtained from ion-implanted *a*-Si which had been annealed at 500°C for two hours. Agreement between model and experiment, particularly in the low-frequency regime, is poor.

Given the overall poor performance of the model of Alben and the MZ model, we also investigate a semi-experimental approach in which a computer generated *a*-Si sample is used to calculate the VDOS and experimental data is used to describe the coupling parameter. This approach is justified because several studies have indicated that changes in the Raman spectrum of amorphous silicon are due to changes in the VDOS and to a lesser degree to changes in the coupling parameter [101, 102].

It is important to recognize the limitations of this approach. The coupling parameter does to some extend depend on the structure of the sample. For example, in the limit of crystalline materials, the coupling becomes exactly zero for all frequencies, except for those in the TO band. However, no forbidden transitions arise in the disordered phase which justifies the semi-experimental approach used here.

The results of the semi-experimental approach are illustrated in the bottom graph of Figure 6.2. Here, we show the Raman spectrum obtained by multiplying a computer generated VDOS with experimental coupling parameter data (solid). To calculate the VDOS, we used a well-annealed *a*-Si sample with $\Delta\theta = 10.0°$; the experimental coupling parameter was taken from Ref. [99]. The dashed line shows again the experimental Raman spectrum taken from Ref. [101]. Agreement with experiment has improved substantially.

Of the two models considered here, the MZ model provides slightly more activity in the low-frequency regime than the model of Alben; comparison with experiment would therefore favor the MZ model. However, given the overall poor performance of both models, results obtained with the semi-experimental approach will also be provided.

6.3.2 Raman TO peak width and $\Delta\theta$

The intensity of the Raman TO peak decreases abruptly on the high frequency side, but not on the low frequency side. Beeman therefore defines Γ as twice the half-width at half the maximum height on the high frequency side of the TO peak, as a meaningful parameter to specify the TO peak width [66]. In this chapter the same

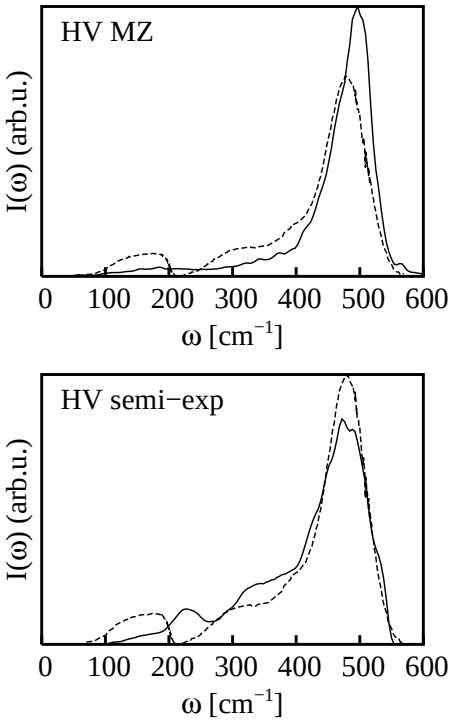

Figure 6.2: **top:** Reduced HV Raman spectrum for *a*-Si calculated using the MZ model (solid). **bottom:** Reduced HV Raman spectrum calculated using the semi-experimental approach; the VDOS is obtained by simulation, the coupling parameter is taken from Ref. [99]. The dashed line in both graphs shows an experimental reduced Raman spectrum taken from Ref. [101]. Frequency is in cm^{-1} and all spectra are area-normalized.

definition is used.

The solid lines in Figure 6.3 show the relation between Γ and $\Delta\theta$ for HV polarized light, derived using the model of Alben (top), the MZ model (middle) and the semi-experimental approach (bottom). Also shown is the result obtained by Beeman (dashed).

The model of Alben and the MZ model produce similar results; linear least square fits yield the equations $\Gamma/2 = 3.0\Delta\theta - 6.5$ and $\Gamma/2 = 3.7\Delta\theta - 13.3$, respectively. Compared to the result of Beeman, $\Gamma/2 = 3.0\Delta\theta + 7.5$, we see agreement on the sensitivity (i.e. slope of the lines) of Γ to $\Delta\theta$, but not on the overall offset (i.e. intercepts of the lines). The same holds for the result obtained in the semi-experimental approach; least square fitting yields $\Gamma/2 = 3.3\Delta\theta + 9.2$ in that case.

6.3.3 Raman TO peak position and $\Delta\theta$

As another way to obtain structural information on *a*-Si from its Raman spectrum, we investigate the relation between the TO peak frequency (ω_{TO}) and $\Delta\theta$. Figure 6.4 shows the relation between ω_{TO} and $\Delta\theta$ for HV polarized light, derived using the model of Alben (top), the MZ model (middle) and the semi-experimental approach (bottom).

According to Figure 6.4, the TO peak shifts to higher frequency as $\Delta\theta$ decreases. However, agreement with experiment for both the model of Alben and the MZ model is poor. The TO peak position as observed in experiments is around 480 cm^{-1} [101]. In well-annealed amorphous silicon samples, where $\Delta\theta$ is approximately 10 degrees, the models exceed the experimental value by around 20 cm^{-1}. The semi-experimental approach is in much better agreement with experiment; a linear fit yields the equation $\omega_{TO} = -2.5\Delta\theta + 505.5$ which for $\Delta\theta = 10.0^\circ$ predicts $\omega_{TO} = 480.5$ cm^{-1}. The reason is that in the model of Alben and the MZ model, ω_{TO} is determined by the peak in the coupling parameter, whereas in the semi-experimental approach, it is determined by the VDOS.

6.3.4 Raman TA/TO intensity ratio and $\Delta\theta$

Next, we confirm that the TA/TO intensity ratio I is directly related to $\Delta\theta$. Figure 6.5 shows I as a function of $\Delta\theta$ for HV polarized light using the model of Alben (top), the MZ model (middle) and the semi-experimental approach (bottom).

We observe an approximately linear increase of the intensity ratio I with increasing $\Delta\theta$ for all three methods. Experimentally, the intensity ratio is around $I = 0.11$, see Ref. [101]. Both the model of Alben and the MZ model predict a much smaller intensity ratio of order $I = 10^{-2}$. This finding is consistent with the earlier observation that these models underestimate the Raman activity in the low-frequency end

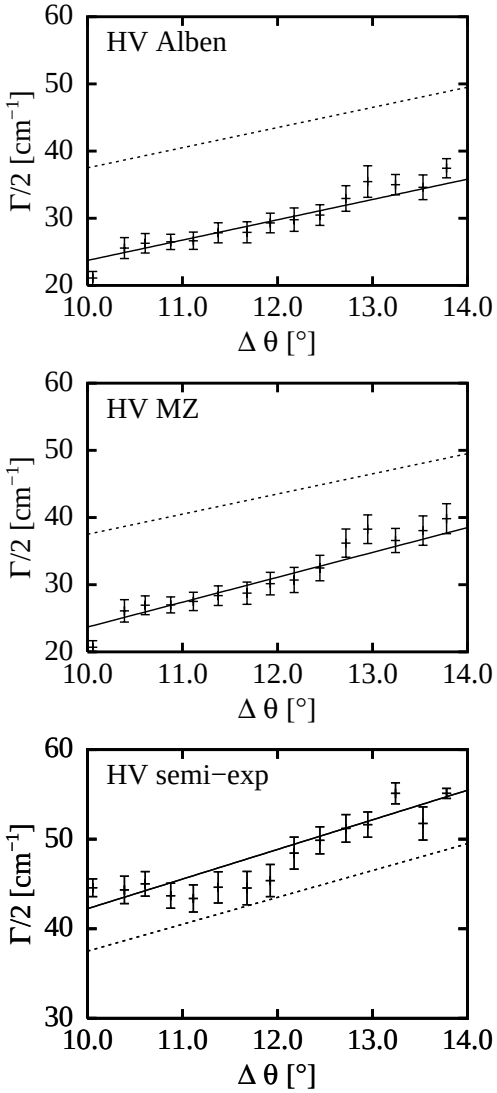

Figure 6.3: HV Raman TO peak width $\Gamma/2$ as a function of $\Delta\theta$, calculated using the model of Alben (top), the MZ model (middle) and the semi-experimental approach (bottom). The solid lines are linear least-squares fits; the dashed line is the result of Beeman: $\Gamma/2 = 7.5 + 3\Delta\theta$. The units of $\Gamma/2$ and $\Delta\theta$ are cm^{-1} and degrees, respectively.

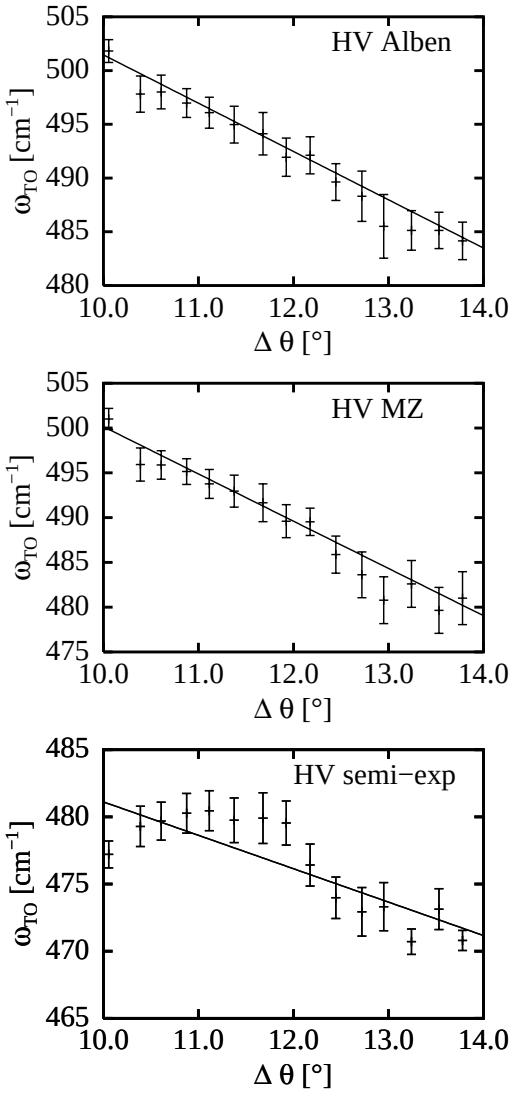

Figure 6.4: Reduced HV Raman TO peak position as a function of $\Delta\theta$ for *a*-Si, calculated using the model of Alben (top), the MZ model (middle) and the semi-experimental approach (bottom). The peak position and $\Delta\theta$ are given in cm^{-1} and degrees, respectively. The solid lines are least-squares fits through the points.

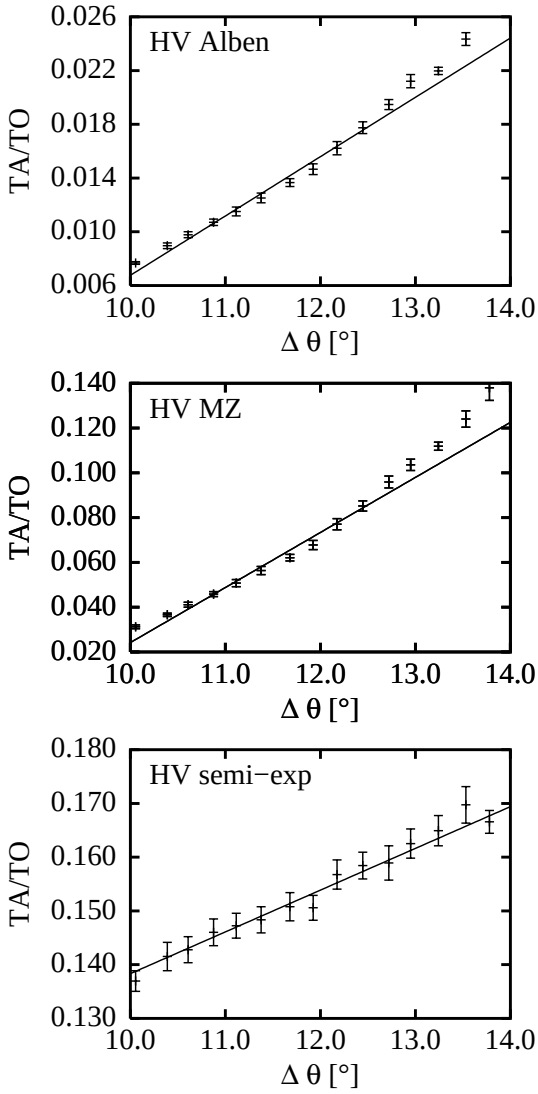

Figure 6.5: HV Raman TA/TO intensity ratio as a function of $\Delta\theta$ for *a*-Si, calculated using the model of Alben (top), the MZ model (middle) and the semi-experimental approach (bottom). The solid lines are least-squares fits; $\Delta\theta$ is in degrees.

of the spectrum. The semi-experimental approach yields a ratio of $I = 0.14$ (for $\Delta\theta = 10.0°$), which is in better agreement with experiment.

6.4 Conclusions

We have generated nine independent sets of 1000-atom samples of *a*-Si that display a variety of short-range order; the spread in nearest-neighbor bond angles ranges from 10 to 14 degrees. For these samples, the HV Raman spectra are calculated. To describe the Raman scattering process, we have used the earlier bond polarizability model of Alben *et al.*, the more recent model of Marinov and Zotov as well as experimental data taken from Ref. [99].

Comparison to experiment shows that both the model of Alben and the MZ model greatly underestimate the Raman activity in the low-frequency regime of the spectrum. This makes these models less suitable to describe low-frequency features of the Raman spectrum, for instance the TA peak. Of the two models considered here, the MZ model is closer to experiment. However, for a more accurate calculation of Raman spectra, we propose a semi-experimental approach. In this approach, the VDOS is obtained in computer simulations and experimental data is used to describe the coupling parameter.

As ways to obtain structural information on amorphous silicon from its Raman spectrum, we obtained the following relations:

- $\Gamma/2 = 3.3\Delta\theta + 9.2$,
- $\omega_{TO} = -2.5\Delta\theta + 505.5$,
- $I = 0.0078\Delta\theta + 0.0606$,

where the polarization is HV and where the semi-experimental approach was used. Here, $\Gamma/2$ is the half-width of the TO peak in inverse cm, ω_{TO} is the TO peak frequency in inverse cm, $\Delta\theta$ is the variation in the mean bond angle in degrees and I is the ratio of the TA to TO peak intensity.

Compared to the result of Beeman: $\Gamma/2 = 3\Delta\theta + 7.5$, we find that our result is similar. However, our results also indicate that a strict linear relation may not be appropriate. We also observe that ω_{TO} shifts towards higher frequency, as $\Delta\theta$ decreases. Using the above equation, the shift is approximately 7.5 inverse cm, going from unannealed amorphous silicon ($\Delta\theta \approx 13°$) to annealed amorphous silicon ($\Delta\theta \approx 10°$). This is in quantitative agreement with experiment [101]. Again we observe that a strict linear relation may not be appropriate. Finally, we have shown that the Raman TA/TO intensity ratio is directly related to $\Delta\theta$; the relation is approximately linear.

Chapter 7

Configurational Entropy

In this chapter we present a computationally efficient method to calculate the configurational entropy of network-forming materials. The method requires only the atomic coordinates and bonds of a single well-relaxed configuration. This is in contrast to the multiple simulations that are required for other methods to determine entropy, such as thermodynamic integration. We use our method to obtain the configurational entropy of well-relaxed networks of amorphous silicon and vitreous silica. For these materials we find configurational entropies of $0.93k_B$ and $0.88k_B$ per silicon atom, respectively.

The work presented in this chapter is based on R.L.C. Vink and G.T. Barkema, *Configurational entropy of network-forming materials*, Phys. Rev. Lett. **89**, 076405 (2002).

7.1 Introduction

In materials such as vitreous silica, amorphous silicon or vitreous ice, the structure is determined by the set of bonds (covalent or hydrogen) between particles. From here on, we will refer to these materials as *network-forming materials*. While the local environment of each particle is usually governed by strict rules, the bonded network can show a wide variety of different topologies. The focus of this chapter is to present a method to estimate the number of topologies that a network-forming material can take, or more precisely, its configurational entropy.

The common computational procedure to estimate the entropy S at temperature T_2 is to measure the average energy E as a function of temperature at constant volume and then to integrate from a temperature T_1 at which the entropy is known:

$$S(T_2) - S(T_1) = \int_{T_1}^{T_2} \frac{1}{T} \frac{\partial E}{\partial T} dT. \tag{7.1}$$

This requires sampling a large number of different configurations and can therefore only be applied to systems with fast dynamics. We present a completely different approach to estimate the entropy, based on information theory [103], and related to the work of Schlijper *et al.* who determined the entropy of the Ising and three-states Potts models [104].

7.2 Information theory

One important concept in information theory is the Shannon entropy. It is commonly explained in the context of a string of n bits. In this case, the Shannon entropy $H(n)$ is defined as:

$$H(n) = -\sum_i p(i) \log_2 p(i), \tag{7.2}$$

where the index i runs over all possible bit sequences of length n and $p(i)$ is the probability of sequence i occurring. A related concept is the entropy density s of a large string of N bits:

$$s = \lim_{n\to\infty} [H(n+1) - H(n)]. \tag{7.3}$$

A practical procedure to estimate s for such a long string is to extract from it a large number of m sub-sequences, each containing n bits with $n \ll N$. An estimate for the probabilities $p(i)$ is then given by:

$$p(i) \approx \frac{f_i}{m}, \tag{7.4}$$

where f_i equals the number of times sub-sequence i was observed. The estimates for $p(i)$ in combination with Eq. (7.2) yield $H(n)$. The entropy density s is then obtained by using Eq. (7.3). Usually, s converges rapidly in the limit $n \to \infty$ and even moderate values of n are sufficient to predict s accurately.

For systems in equilibrium it is easily shown that the Shannon entropy and the thermodynamic entropy of Eq. (7.1) are equivalent, apart from a factor of $k_b \ln(2)$. In this case, the probabilities $p(i)$ are simply given by the Boltzmann weights: $p(i) = \exp(-\beta E_i)/Z$, where $k_B\beta$ is the inverse temperature, Z the partition function and E_i the energy of state i. In the present work we show how information theory can also be used to obtain the configurational entropy of network forming materials. The method we present can be applied to any network provided (1) the atomic coordinates are known and (2) a list of bonds is supplied or can be constructed—for instance based on a distance criterion—which uniquely determines the network.

7.3 Network forming materials

We have generalized the application of information theory to network forming materials. To determine the configurational entropy of such a material we choose a large number m of random positions in the simulation cell. For each position we find the nearest n particles and identify the graph formed by the bonds connecting these particles.

When we identify a graph, we consider only its topology (determined by the bonds) and not the atomic coordinates. This point is illustrated further in Figure 7.1 where we show two topologically equivalent graphs. Even though the displayed graphs differ in shape, it is possible to continuously deform one graph into the other: the graphs are thus topologically equivalent. The topology of a graph is usually specified in terms of a list of bonds. In what follows, a bond between two particles a and b is denoted by $a-b$; the graph topology is specified by listing all the bonds it contains. For graph (a) this yields: $\{1-11; 1-22; 3-9; 3-11; 3-23; 4-23; 4-55; 9-22; 9-55\}$, while for graph (b) we obtain: $\{2-34; 2-75; 4-13; 4-32; 4-34; 8-26; 8-32; 13-26; 32-75\}$. The fact that graphs (a) and (b) are topologically equivalent is not at all obvious from a first glance at the list of bonds. We use the graph automorphism to transform a given list of bonds into a standard form such that two topologically equivalent graphs yield identical lists; for implementation details see Ref. [105].

We count the number of times a graph is observed and use Eq. (7.4) to estimate its corresponding probability of occurrence. These probabilities are fed into Eq. (7.2) to obtain $H(n)$. This procedure is illustrated in Figure 7.2 for a two-dimensional threefold coordinated network. In this example, we calculate $H(n)$ for $n=8$. We choose $m=6$ random positions in the network and for each position we determine the graph formed by the closest $n=8$ atoms: these graphs are marked with circles in the upper frame of Figure 7.2. The frequency of occurrence for each graph is summarized in the lower frame of Figure 7.2. The reader can check that the left graph was observed three times, the middle graph twice and the right graph once. Based on these $m=6$ random positions, the estimates for the occurrence probabilities thus become $(3/6)$, $(2/6)$ and $(1/6)$, respectively. Feeding these probabilities into Eq. (7.2) yields:

$$H(8) = -(3/6)\ln(3/6) - (2/6)\ln(2/6) - (1/6)\ln(1/6) \approx 1.0114. \qquad (7.5)$$

One side-effect of choosing random positions is that a small displacement of one of these random positions will usually result in exactly the same list of n nearest particles and thus the same graph. Consequently, there is an upper bound to the number m of random positions that one should choose in a simulation cell containing N particles. An estimate of this upper bound is obtained from the typical distance over which a random position can be displaced without altering the selected graph.

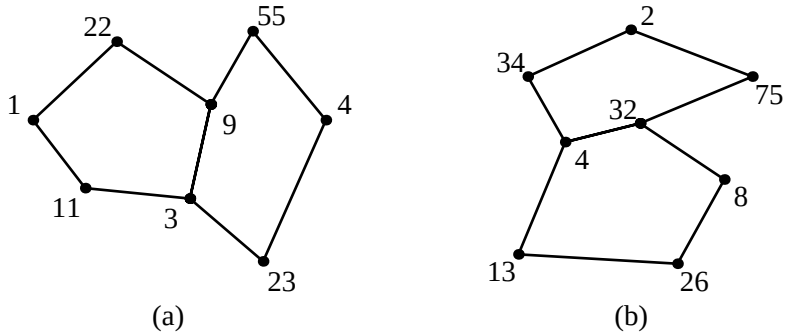

Figure 7.1: Diagram showing two topologically equivalent graphs (a) and (b) containing $n = 8$ particles. Even though the above graphs differ in shape, it is possible to continuously deform one graph into the other.

From this we obtained as upper bounds $m = 1.6nN$ and $m = 3.4n^2N$ for two-dimensional and three-dimensional networks, respectively.

A related side-effect of choosing random positions is that the number of different graphs observed gets multiplied with a factor proportional to n^{d-1}. Up to a constant, this results in a correction to $H(n)$ of the form $g(n) = (d-1)\ln(n)$, with d the spatial dimension of the network. The latter can be verified in crystalline networks where the configurational entropy is zero.

Graphs with a probability $p(i)$ smaller than $1/m$ will likely be observed only once, if at all. This finite-size effect grows with n, when the selected graphs become very complex. To monitor the impact of this effect, we record the quantity $H_1(n)$, defined as the contribution to $H(n)$ of the topologies observed once. We reject the measurements for which $H_1(n)$ exceeds one percent of $H(n)$. Furthermore, we observed that the quantity $H(n)+c\cdot H_1(n)/H(n)$ converges much faster with increasing m than $H(n)$ itself, with a suitable choice of c. We therefore use this extrapolated value as our best estimate for $H(n)$.

In Figure 7.3 we show the typical behavior of the corrected Shannon entropy $H_c(n) \equiv H(n) - g(n)$ as a function of graphsize n. The entropy follows from Eq. (7.3). The rapid convergence of the limit is demonstrated by the linear behavior of $H_c(n)$ for intermediate n shown in Figure 7.3 by the dashed line. The entropy per atom equals the slope of this line. In Figure 7.3 we have marked with circles the points for which $H_1(n)$ exceeds one percent of $H(n)$. These points suffer from finite-size effects and should not be used.

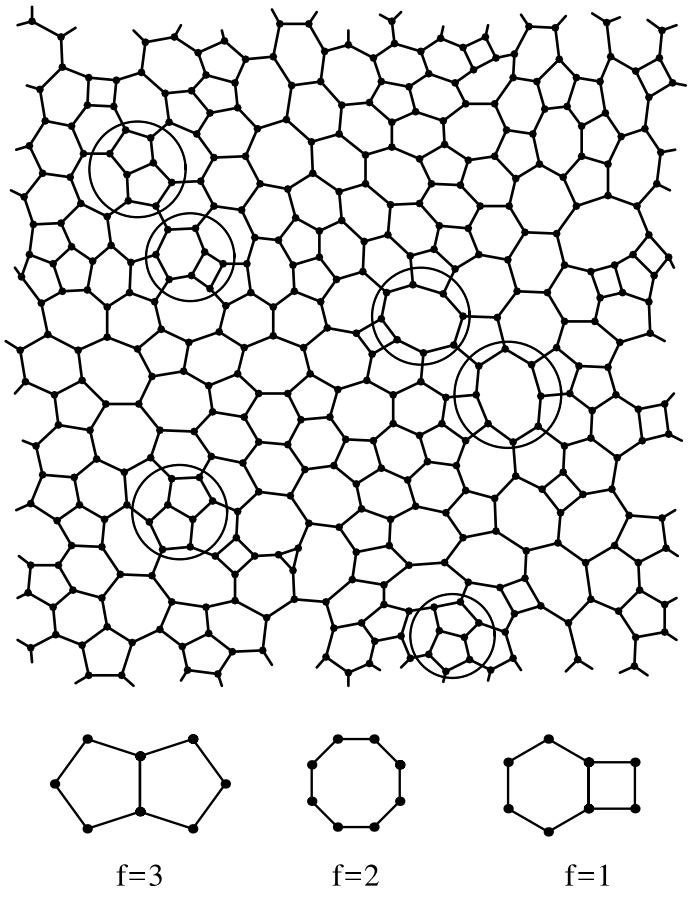

Figure 7.2: Evaluation of the Shannon entropy $H(n)$ for $n = 8$. The upper frame shows a three-fold coordinated network in which $m = 6$ random positions have been selected. For each random position, the graph formed by the closest $n = 8$ particles is marked with a circle. The lower frame shows the frequency of occurrence f for each of the observed graphs; see also details in text.

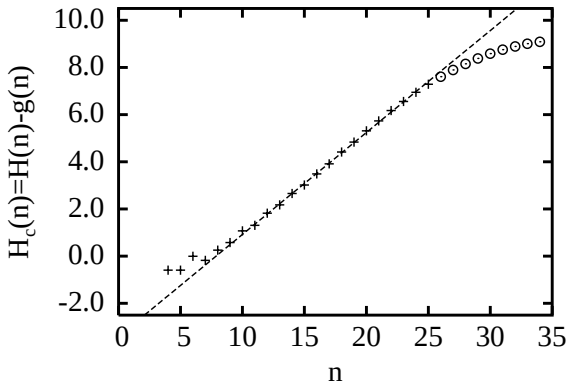

Figure 7.3: Typical behavior of the corrected Shannon entropy $H_c(n)$ in units of k_B as a function of graph size n; crosses (circles) mark measurements for which $H_1(n)$ contributes less (more) than one percent to $H(n)$. The dashed line is a straight-line fit to the crosses, starting from $n = 10$. The slope of this line is our estimate for the configurational entropy per atom s. These data are obtained from a two-dimensional sillium configuration containing 20,000 atoms described in Chapter 4.

7.4 Results

To test the usefulness of the above procedure, we apply it to the *sillium* model [18], one of the prototype models to study network-forming materials. In this model, tuned for amorphous silicon, an explicit list of covalent bonds between pairs of Si atoms is kept, with the property that each Si atom is bonded to four neighboring atoms. The energy is described by the Keating potential, which contains a quadratic penalty for bond length deviations from the crystalline distance of 2.35 Å, and a quadratic penalty for bond angle deviations from the tetrahedral angle $\Theta_0 = \arccos(-1/3)$. The list of bonds determines the atomic positions uniquely, since in this model the energy is minimized at all times. As a result, the phase space of this model is limited to a finite number of $3N$-dimensional points. The evolution of the network consists of a large number of random bond transpositions, each accepted with the Metropolis probability:

$$P = \min\left[1, \exp\left(\frac{E_b - E_f}{k_B T}\right)\right], \tag{7.6}$$

where T is the temperature and E_b and E_f are the total (minimized) energies of the system before and after the proposed bond transposition. A typical sillium network is shown in Figure 7.4. Our networks are generated as described in Chapter 4 and Refs. [7, 12]; in which a number of algorithmic improvements have been proposed as

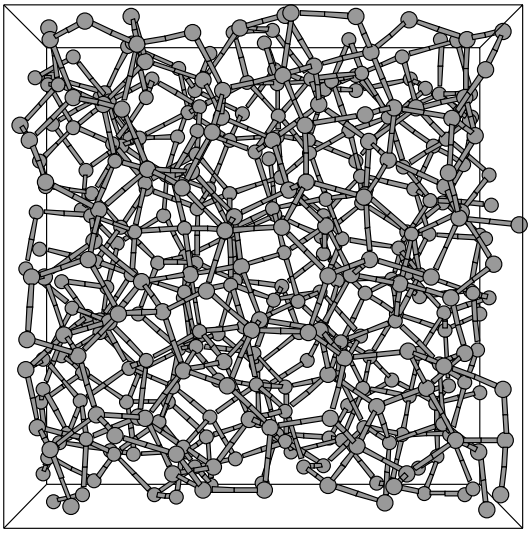

Figure 7.4: A three-dimensional sillium network. Each particle is four-fold coordinated but no long-range order exists.

compared to the original algorithm of Wooten, Winer and Weaire.

7.4.1 Comparison

To verify the validity of the information theory approach we first turn to a two-dimensional version of the sillium model. Contrary to the three-dimensional sillium model, the dynamics here does not lead to glassy states. This allows us to determine the entropy in equilibrium using both the standard approach—via Eq. (7.1)—and information theory. In this two-dimensional model, atoms are three-fold coordinated and the ideal bond angle is 120 degrees; a typical configuration is shown in Figure 7.5.

We simulate a two-dimensional sillium network containing 1008 atoms for a number of (physically interesting) temperatures ranging from $k_BT = 0.15$ eV to $k_BT = 0.60$ eV using periodic boundary conditions in both directions. At each temperature we bring the system to equilibrium with 100 attempted bond transpositions per atom. Next, 20 snapshots of the network are stored; each separated by five attempted bond transpositions per atom. From these snapshots the average energy and the Shannon entropy are obtained. In determining the Shannon entropy we draw clusters from each snapshot simultaneously. After the simulation has covered the entire temperature range, the entropy is also obtained from the average energy measurements and Eq. (7.1).

Figure 7.6 shows the configurational entropy as a function of temperature where

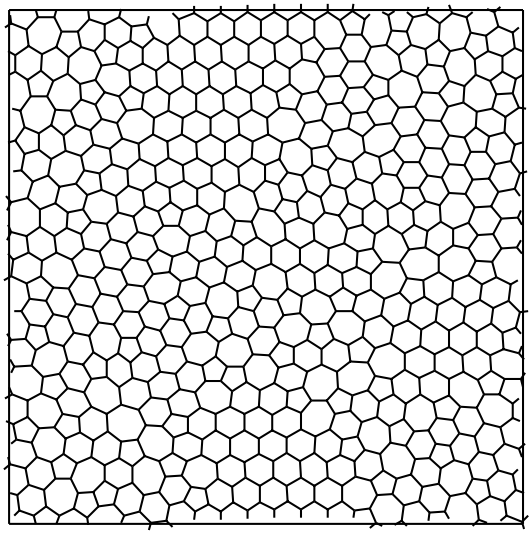

Figure 7.5: A two-dimensional sillium network. Each particle is three-fold coordinated, with a preferred bond angle of 120 degrees.

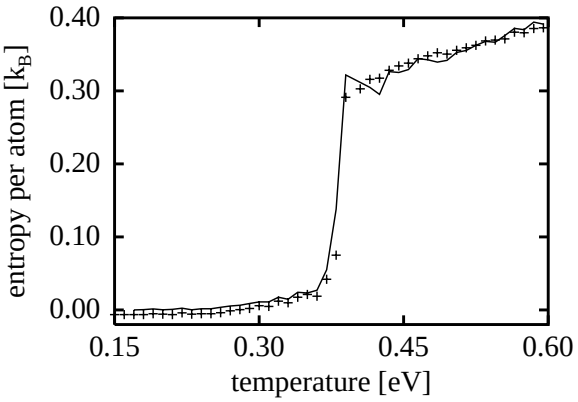

Figure 7.6: Diagram showing the configurational entropy per atom in units of k_B as a function of temperature in eV for a two-dimensional sillium network consisting of 1008 atoms. The solid curve shows the entropy per atom as obtained using the standard thermodynamic approach; crosses show the entropy per atom obtained using information theory.

the standard thermodynamic approach is compared to information theory. There appears to be a phase transition near $k_B T = 0.37$ eV shown by the sudden jump in entropy. The remarkable feature of the displayed results is the overall good agreement between the two methods, even near the phase transition. This is in agreement with related work on the Ising model [104], in which also surprisingly few numerical problems were encountered close to the critical point.

7.4.2 Amorphous silicon

Next, we use information theory to determine the configurational entropy of a well-relaxed three-dimensional sillium network containing 20,000 atoms. This network was generated with the improved Wooten, Winer and Weaire algorithm [7, 12]. The Keating energy of this network is 0.286 eV per atom; the standard deviation in the mean bond angle is 9.63 degrees. Structural and electronic properties of this network are reported in Chapter 4 and are in excellent agreement with experiments [7]. Applying our method to this model, we obtain a configurational entropy of $0.93 k_B$ per atom.

By construction, *sillium* networks do not contain coordination defects. To study the effect of defects, we generated a number of networks in which coordination defects were introduced by removing from the explicit list of bonds the longest ones. The method works equally well for such networks in which the atomic coordination number varies significantly. We observed that, as long as less than 2% of the atoms are undercoordinated, the configurational entropy does not change significantly.

The (classical) vibrational entropy is obtained from the eigenvalues of the dynamical matrix and for this network was found to be $3.07 k_B$ per atom. In the crystalline phase there is only vibrational entropy contributes to the entropy; in this case $3.18 k_B$ per atom. The difference in entropy between the crystalline and amorphous phases of silicon is therefore estimated to be $0.82 k_B$ per atom.

The energy difference between the crystalline and amorphous phases of silicon was recently determined by Biswas [106] using tight-binding, who found an energy difference of 0.18 eV per atom which is in good agreement with values reported in Ref. [107].

With the above estimates for the differences in energy and entropy we can calculate the transition temperature T_c, defined as the temperature where the free energy difference between the crystalline phase and the amorphous phase changes sign. It is given by:

$$T_c = \frac{\Delta E}{\Delta S}, \tag{7.7}$$

where ΔE and ΔS are the energy difference and the entropy difference between the crystalline and the amorphous phase, respectively. Substitution of our estimates for

ΔE and ΔS into Eq. (7.7) yields $T_c \approx 2547$ K. This temperature compares remarkably well with the value of $T_c \approx 2500$ K as inferred from calorimetric experiments on the amorphous phase of silicon [94], and is well above the melting point of silicon. It confirms that the amorphous phase is not thermodynamically stable at any temperature.

7.4.3 Vitreous silica

As a final application of our method we determine the configurational entropy of vitreous silica. The structure of this material is formed by covalent bonds between silicon atoms and oxygen atoms. Barring rare defects, each silicon atom is bonded to four oxygen atoms and each oxygen atom is bonded to two silicon atoms. We generate a silica network containing 3000 atoms (with periodic boundary conditions) using the method described in Chapter 4. The resulting network is then quenched with the BKS potential [70] following the same approach as in Chapter 4. The BKS energy per silicon atom of the quenched network was found to be $E = 0.16$ eV above that of the β-cristobalite structure. For comparison, samples prepared by molecular dynamics typically yield a much larger energy difference of $E = 0.30$ eV. This clearly demonstrates that our network is well relaxed. After quenching with the BKS potential, the atoms remain perfectly coordinated: the silicon-oxygen bonds are easily reconstructed from a distance criterion and the silicon-oxygen radial distribution function. For our network, the average O-Si-O bond angle is 109.43 degrees with a standard deviation of 4.39 degrees; the average Si-O-Si bond angle was found to be 150.77 degrees with a standard deviation of 12.11 degrees.

To estimate the configurational entropy per silicon atom in well-relaxed vitreous silica, we used the above network and replaced each oxygen atom plus its two bonds by a single silicon-silicon bond. Next, we applied the information-theoretic method described earlier on this network and found for the configurational entropy $0.88k_B$ per silicon atom. Given the limited size of this sample we estimate that the actual entropy might be up to 10% larger. Ignoring the difference in vibrational entropy, as well as the entropy contribution of possible multiple oxygen positions, we obtain for the transition temperature of vitreous silica $T_c \approx 1700$ K. This temperature is significantly lower than the melting temperature $T_m = 2003$ K of silica [1].

7.5 Conclusions

In summary, we have developed a computationally efficient method to determine the configurational entropy of network forming materials. For well-relaxed samples of amorphous silicon and vitreous silica, we find for the entropy per silicon atom $0.93k_B$ and $0.88k_B$, respectively. In future research, we hope to extend the appli-

cability of this method to other disordered materials such as colloidal systems and metallic glasses.

Acknowledgements

We thank Henk van Beijeren and Normand Mousseau for stimulating discussion, and Normand Mousseau also for the computation of the BKS energies.

Bibliography

[1] S. R. Elliott, *Physics of Amorphous Materials* (Longman Group Limited, United Kingdom, 1984).

[2] K. Vollmayr, W. Kob, and K. Binder, Phys. Rev. B **54**, 15808 (1996).

[3] K. Laaziri, S. Kycia, S. Roorda, M. Chicoine, J. L. Robertson, J. Wang, and S. C. Moss, Phys. Rev. Lett. **82**, 3460 (1999).

[4] K. Laaziri, S. Kycia, S. Roorda, M. Chicoine, J. L. Robertson, J. Wang, and S. C. Moss, Phys. Rev. B **60**, 13520 (1999).

[5] C. Kittel, *Introduction to Solid State Physics* (John Wiley & Sons, Inc., New York, 1953).

[6] F. H. Stillinger and T. A. Weber, Phys. Rev. B **31**, 5262 (1985).

[7] R. L. C. Vink, G. T. Barkema, M. A. Stijnman, and R. H. Bisseling, Phys. Rev. B **64**, 245214 (2001).

[8] O. F. Sankey, D. A. Drabold, and G. B. Adams, Bull. Am. Phys. Soc. **36**, 924 (1991).

[9] A. J. M. Berntsen, *Structural Disorder in Pure and Hydrogenated Amorphous Silicon*, Ph.D. thesis, Faculty of Physics and Astronomy, Utrecht University (1993).

[10] M. Watanabe, S. Juodkazis, H. Sun, S. Matsuo, and H. Misawa, Appl. Phys. Lett. **77**, 13 (2000).

[11] W. H. Zachariasen, J. Am. Chem. Soc. **54**, 3841 (1932).

[12] G. T. Barkema and N. Mousseau, Phys. Rev. B **62**, 4985 (2000).

[13] R. J. Bell and P. Dean, Nature (London) **212**, 1354 (1966).

[14] D. E. Polk, J. Non-cryst. Solids **5**, 365 (1971).

[15] M. E. J. Newman and G. T. Barkema, *Monte Carlo Methods in Statistical Physics* (Clarendon Press, Oxford, 1999).

[16] F. Wooten and D. Weaire, Solid State Physics **40**, 1 (1987).

[17] R. Schropp (2002), private communication.

[18] F. Wooten, K. Winer, and D. Weaire, Phys. Rev. Lett. **54**, 1392 (1985).

[19] B. H. Bransden and C. J. Joachain, *Quantum Mechanics* (Longman Scientific & Technical, Harlow, 1989).

[20] D. Frenkel and B. Smit, *Understanding Molecular Simulation* (Academic Press, Inc., San Diego, 1996).

[21] E. R. Cowley, Phys. Rev. Lett. **60**, 2379 (1988).

[22] P. N. Keating, Phys. Rev. **145**, 637 (1966).

[23] G. T. Barkema and N. Mousseau, Phys. Rev. Lett. **77**, 4358 (1996).

[24] G. T. Barkema and N. Mousseau, Phys. Rev. Lett. **81**, 1865 (1998).

[25] R. L. C. Vink, G. T. Barkema, W. F. van der Weg, and N. Mousseau, J. Non-Cryst. Solids **282**, 248 (2001).

[26] M. C. Payne, M. P. Teter, D. C. Allan, T. A. Arias, and J. D. Joannopoulos, Rev. Mod. Phys. **64**, 1045 (1992).

[27] W. C. Swope, H. C. Andersen, P. Berens, and K. Wilson, J. Chem. Phys. **76**, 637 (1982).

[28] M. P. Allen and D. J. Tildesley, *Computer Simulation of Liquids* (Clarendon Press, Oxford, 1987).

[29] R. Biswas, G. S. Grest, and C. M. Soukoulis, Phys. Rev. B **36**, 7437 (1987).

[30] W. D. Luetdke and U. Landman, Phys. Rev. B **37**, 4656 (1988).

[31] S. J. Cook and P. Clancy, Phys. Rev. B **47**, 7686 (1993).

[32] N. Mousseau and G. T. Barkema, Phys. Rev. E **57**, 2419 (1998).

[33] N. Mousseau and G. T. Barkema, Comput. Sci. Eng. **1**, 74 (1999).

[34] R. Malek and N. Mousseau, Phys. Rev. E **62**, 7723 (2000).

[35] N. Mousseau, P. Derreumaux, G. T. Barkema, and R. Malek, J. Mol. Graph. and Modelling **19**, 78 (2001).

[36] T. Pang, *Computational Physics* (Cambridge University Press, New York, 1997).

[37] N. Metropolis, A. W. Rosenbluth, M. N. Rosenbluth, A. H. Teller, and E. Teller, J. Chem. Phys. **21**, 1087 (1953).

[38] J. F. Justo, M. Z. Bazant, E. Kaxiras, V. V. Bulatov, and S. Yip, Phys. Rev. B **58**, 2539 (1998).

[39] B. R. Djordjević, M. F. Thorpe, and F. Wooten, Phys. Rev. B **52**, 5685 (1995).

[40] L. Brus, J. Phys. Chem **98**, 3575 (1994).

[41] R. West, in E. Abe, F. G. A. Stone, and G. Wilkinson, eds., *Comprehensive Organometallic Chemistry II* (Pergamon, Oxford, 1995), vol. 2, p. 77.

[42] R. D. Miller and J. Michl, Chem. Rev. **89**, 1359 (1989).

[43] R. G. Jones and R. E. Benfield, Macromolecules **26**, 4878 (1993).

[44] P. A. Bianconi and T. W. Weidman, J. Am. Chem. Soc. **110**, 2342 (1988).

[45] P. A. Bianconi, F. C. Schilling, and T. W. Weidman, Macromolecules **22**, 1697 (1989).

[46] K. Furukawa, M. Fujino, and N. Matsumoto, Macromolecules **22**, 3423 (1990).

[47] W. L. Wilson and T. W. Weidman, J. Phys. Chem. **95**, 4568 (1991).

[48] J. Maxka, J. Chrusciel, M. Sasaki, and K. Matyjaszewski, Macromol. Symp. **77**, 79 (1994).

[49] T. J. Cleij, S. K. Y. Tsang, and L. W. Jenneskens, Macromolecules **32**, 3286 (1999).

[50] C. A. van Walree, T. J. Cleij, L. W. Jenneskens, E. J. Vlietstra, G. P. van der Laan, M. P. de Haas, and E. T. G. Lutz, Macromolecules **29**, 7362 (1996).

[51] J. B. Lambert, J. L. Pflug, and C. L. Stern, Angew. Chem. Int. Ed. Engl. **34**, 98 (1995).

[52] H. Suzuki, Y. Kimata, S. Satoh, and A. Kuriyama, Chem. Lett. **293** (1995).

[53] G. T. Barkema, M. J. Howard, and J. L. Cardy, Phys. Rev. E **53**, 2017 (1996).

[54] J. M. Zeigler, Polym. Prepr. **27**, 109 (1986).

[55] L. F. Brough and R. West, J. Am. Chem. Soc. **103**, 3049 (1981).

[56] S. M. Chen, A. Katti, A. Blinka, and R. West, Synthesis p. 684 (1985).

[57] W. Uhlig, Z. Naturforsch. **50b**, 1674 (1995).

[58] N. Casarini, L. Lunazzi, and A. Mazzanti, J. Org. Chem. **63**, 9125 (1998).

[59] K. Devlin, *Mathematics, the new golden age* (Penguin, UK, 1990).

[60] S. Kugler, L. Pusztai, L. Rosta, P. Chieux, and R. Bellissent, Phys. Rev. B **48**, 7685 (1993).

[61] S. Nakhmanson, P. M. Voyles, N. Mousseau, G. T. Barkema, and D. A. Drabold, Phys. Rev. B **63**, 235207 (2001).

[62] R. C. Lindenbergh, *Limits of Voronoi Diagrams*, Ph.D. thesis, Department of Mathematics, Utrecht University (2002).

[63] J. R. Shewchuk, in M. C. Lin and D. Manocha, eds., *Applied Computational Geometry: Towards Geometric Engineering* (Springer-Verlag, 1996), vol. 1148 of *Lecture Notes in Computer Science*, pp. 203–222, from the First ACM Workshop on Applied Computational Geometry.

[64] C. B. Barber, D. P. Dobkin, and H. Huhdanpaa, ACM Transactions on Mathematical Software (TOMS) **22**(4), 469 (1996).

[65] Y. Tu and J. Tersoff, Phys. Rev. Lett. **84**, 4393 (2000).

[66] D. Beeman, R. Tsu, and M. F. Thorpe, Phys. Rev. B **32**, 874 (1985).

[67] R. L. C. Vink, G. T. Barkema, and W. F. van der Weg, Phys. Rev. B **63**, 115210 (2001).

[68] K. Ding and H. C. Andersen, Phys. Rev. B **34**, 6987 (1986).

[69] J. M. Holender and G. J. Morgan, J. Phys. : Condens. Matter **3**, 7241 (1991).

[70] B. W. H. van Beest, G. J. Kramer, and R. A. van Santen, Phys. Rev. Lett. **64**, 1955 (1990).

[71] W. T. Rankin and J. A. Board, Tech. Rep. 95-002, Department of Electrical Engineering, Duke University (1995).

[72] J. R. G. D. Silva, D. G. Pinatti, C. E. Anderson, and M. L. Rudee, Philos. Mag. **31**, 713 (1975).

[73] R. F. Pettifer, R. Dupree, I. Farnan, and U. Sternberg, J. Non-Cryst. Solids **106**, 408 (1988).

[74] J. Tersoff, Phys. Rev. B **38**, 9902 (1988).

[75] M. I. Baskes, J. S. Nelson, and A. F. Wright, Phys. Rev. B **40**, 6085 (1989).

[76] J. R. Chelikowsky, J. C. Philips, M. Kamal, and M. Strauss, Phys. Rev. Lett. **62**, 292 (1989).

[77] R. Biswas and D. R. Hamann, Phys. Rev. Lett. **55**, 2001 (1985).

[78] M. Z. Bazant and E. Kaxiras, Phys. Rev. Lett. **77**, 4370 (1996).

[79] M. Z. Bazant, E. Kaxiras, and J. F. Justo, Phys. Rev. B **56**, 8542 (1997).

[80] H. Balamane, T. Halicioglu, and W. A. Tiller, Phys. Rev. B **46**, 2250 (1992).

[81] N. Zotov, M. Marinov, N. Mousseau, and G. T. Barkema, J. phys. : Condens. Matter **11**, 9658 (1999).

[82] M. Marinov and N. Zotov, Phys. Rev. B **55**, 2938 (1997).

[83] W. A. Kamitakahara, C. M. Soukoulis, H. R. Shanks, U. Buchenau, and G. S. Grest, Phys. Rev. B **36**, 6539 (1987).

[84] I. Štich, R. Car, and M. Parinello, Phys. Rev. B **44**, 11092 (1991).

[85] R. Car and M. Parinello, Phys. Rev. Lett. **60**, 204 (1988).

[86] S. Kugler, G. Molinar, G. Petö, E. Zsoldos, L. Rosta, A. Menelle, and R. Bellissent, Phys. Rev. B **40**, 8030 (1989).

[87] J. Fortner and J. S. Lannin, Phys. Rev. B **39**, 5527 (1989).

[88] S. Roorda, W. C. Sinke, J. M. Poate, D. C. Jacobson, S. Dierker, B. S. Dennis, D. J. Eaglesham, F. Spaepen, and P. Fuoss, Phys. Rev. B **44**, 3702 (1991).

[89] F. Jansen, in *Properties of amorphous silicon*, INSPEC, London (1988), p. 471.

[90] N. Maley, D. Beeman, and J. S. Lannin, Phys. Rev. B **38**, 10611 (1988).

[91] J. E. Smith, M. H. Brodsky, B. L. Crowder, and M. I. Nathan, Phys. Rev. Lett. **26**, 642 (1971).

[92] D. Bermejo and M. Cardona, J. Non-Cryst. Solids **32**, 405 (1979).

[93] M. Ivanda, O. Gamulin, and W. Kiefer, J. Mol. Struct. **480-481**, 651 (1998).

[94] W. C. Sinke, S. Roorda, and F. W. Saris, J. Mater. Res. **3**, 1201 (1988).

[95] R. Tsu, J. G. Hernandez, and F. H. Pollak, J. Non-Cryst. Solids **66**, 109 (1984).

[96] C. K. Wong and G. Lucovsky, in D. Adler, Y. Hamakawa, and A. Madan, eds., *Materials Issues in Amorphous-Semiconductor Technology*, Materials Research Society, Pittsburgh (1986), p. 77.

[97] G. A. N. Connell and R. J. Temkin, Phys. Rev. B **9**, 5323 (1974).

[98] R. Alben, D. Weaire, J. E. Smith, and M. H. Brodsky, Phys. Rev. B **11**, 2271 (1975).

[99] F. Li and J. S. Lannin, Phys. Rev. B **39**, 6220 (1989).

[100] R. J. Bell and D. C. Hibbins-Butler, J. Phys. C: Solid State Phys. **9**, 2955 (1976).

[101] W. F. van der Weg, A. J. M. Berntsen, F. W. Saris, and A. Polman, Materials Chemistry and Physics **46**, 140 (1996).

[102] N. Maley and J. S. Lannin, Phys. Rev. B **35**, 2456 (1987).

[103] C. E. Shannon, The Bell System Technical Journal **27**, 379 (1948).

[104] A. G. Schlijper, A. R. D. van Bergen, and B. Smit, Phys. Rev. A **41**, 1175 (1990).

[105] B. D. McKay, *Nauty User's Guide (Version 1.5)*, Tech. Rep. TR-CS-90-02, Australian National University, Department of Computer Science (1990).

[106] P. Biswas (2001), private communication.

[107] E. Kim and Y. H. Lee, Phys. Rev. B **49**, 1743 (1994).

Samenvatting

Vaste stoffen komen voor in vormen die meer of minder geordend zijn. Kristallen zijn het meest geordend. In dit geval vormen de atomen een regelmatig patroon dat zich eindeloos herhaalt. In amorfe materialen is van een regelmatige structuur geen sprake: het materiaal bezit een zekere mate van wanorde.

Amorfe materialen kennen vele toepassingen, bijvoorbeeld in zonnecellen en kopieerapparaten. De productie van de amorfe vorm van een stof is vaak goedkoper dan de productie van de kristallijne vorm. Men wil daarom graag weten wanneer kristallijn materiaal vervangen kan worden door een amorfe variant. Hiervoor is het noodzakelijk de eigenschappen van amorfe materialen goed te begrijpen.

Ondanks uitgebreid experimenteel onderzoek zijn verscheidene vragen betreffende de structuur van amorfe materialen onbeantwoord. Experimentele technieken, zoals bijvoorbeeld Röntgen spectroscopie, die goed de structuur van kristallen kunnen bepalen, blijken voor amorfe materialen veel minder goed te werken.

Met behulp van computer simulaties is het mogelijk een aantal experimentele beperkingen te omzeilen. Zo kan men tijdens een simulatie bijvoorbeeld precies de positie van een atoom in de ruimte bijhouden, iets wat experimenteel nog niet kan. Als de posities van de atomen bekend zijn, is ook de structuur van het materiaal bepaald.

Een belangrijk aspect van een computer simulatie is hoe men de krachten tussen de atomen in het materiaal bepaald. Simulaties kunnen grofweg in twee groepen verdeeld worden. Aan de ene kant zijn er de *ab initio* simulaties. In dit soort simulaties worden de krachten tussen de atomen bepaald met de Schrödinger vergelijking. Deze methode heeft het voordeel dat de krachten zeer nauwkeurig bepaald kunnen worden en goed overeenstemmen met de realiteit. Het nadeel van deze methode is dat de kracht berekening zeer veel tijd in beslag neemt. In de praktijk kan men op deze manier slechts een klein aantal atomen in beschouwing nemen: maximaal enkele honderden. Dit aantal is niet voldoende om de bulk eigenschappen van een stof goed te beschrijven.

Aan de andere kant zijn er de zogenaamde *empirische* methodes. Deze methodes geven slechts een benadering van de kracht en zijn dus minder nauwkeurig dan *ab initio* methodes. Het grote voordeel van de *empirische* aanpak is dat een veel groter

aantal deeltjes in beschouwing kan worden genomen. In hoeverre de simulatie realistisch is zal moeten blijken uit vergelijking met experimenten.

In dit proefschrift zijn computer simulaties beschreven die de structuur van o.a. amorf silicium en silica nabootsen. Deze simulaties vormen het onderwerp van hoofdstuk 3 en hoofdstuk 4. Beide hoofdstukken zijn gebaseerd op de *empirische* aanpak zodat grote systemen onderzocht konden worden: tot wel 60.000 deeltjes. De computer gegenereerde structuren zijn vervolgens gebruikt om een aantal eigenschappen van amorf silicium en silica te voorspellen, welke goed in overeenstemming blijken te zijn met experimenten. In hoofdstuk 5 en hoofdstuk 6 laten we zien dat de mate van wanorde in amorf silicium direct van invloed is op de optische eigenschappen van dit materiaal. Tenslotte wordt in hoofdstuk 7 de entropie van amorf silicium en silica bepaald.

Acknowledgements

The work presented in this thesis was done in collaboration with many people. It is my pleasure to acknowledge their contributions.

First of all, I want to thank my advisor Gerard Barkema. I have learned a great deal from him, ranging from setting up a simple “makefile” to writing articles and responses to referee reports. I want to thank Normand Mousseau for a pleasant collaboration and for hosting me at Ohio University in the fall of 2000. I also thank David Drabold, Serge Nahkmanson and Rashid Malek for useful discussions during my stay in Ohio.

I would like to thank Werner van der Weg for a productive collaboration and for his help with the comparison of our simulations to experiments. I also thank Henk van Beijeren for his comments on the work presented in Chapter 7.

I want to thank Wim Lourens for proof-reading this thesis and Fons van Hees for stimulating discussions.

Finally, I want to thank my fellow graduate students, colleagues and secretaries for a nice working environment.

Curriculum Vitae

I was born on January 13 1975 in Portchester (NY) in the United States of America. I attended secondary school at the Christelijk College Stad en Lande in Huizen, the Netherlands and passed the Dutch VWO examination in 1993. In the same year I enrolled as a student at the Department of Physics and Astronomy, University of Utrecht and in 1994 passed the propaedeutic examination. During the next three years I attended the theoretical physics program of the University of Utrecht as well as a number of optional courses. I also participated in an exchange program with the University of Wyoming. After writing my Master thesis on the Bose-Einstein condensation of particles with attractive interaction, under the supervision of Prof. Dr. Ir. H.T.C. Stoof, I obtained my Master's degree in 1998.

In January 1999 I started my doctoral research in the field of computational physics at the Werkgroep Fysische Informatica of the University of Utrecht under the supervision of Dr. G.T. Barkema and Prof. Dr. Ir. W. Lourens. The results of this research are presented in this thesis. During this period I also attended a number of workshops, schools and conferences. In the fall of 2000 I visited the Condensed Matter and Surface Sciences Institute of Ohio University for a period of three months. Throughout my student life, I have supervised numerous classes and lectures, both in the Netherlands and in the United States.

Publications

1. R.L.C. Vink and G.T. Barkema, *Large well-relaxed models of vitreous silica*, to be published.

2. R.L.C. Vink and G.T. Barkema, *Configurational entropy of network-forming materials*, Phys. Rev. Lett. **89**, 076405 (2002).

3. R.L.C. Vink, G.T. Barkema, L.W. Jenneskens, and C.A. van Walree, *Simulation of polysilane and polysilyne formation and structure*, J. Chem. Phys. **116**, 854 (2002).

4. R.L.C. Vink, G.T. Barkema, R.H. Bisseling, and M.A. Stijnman, *Towards device-size atomistic models of amorphous silicon*, Phys. Rev. B **64**, 245214 (2001).

5. G. T. Barkema, N. Mousseau, R. L. C. Vink, and P. Biswas, *Basic mechanisms of structural relaxation and diffusion in amorphous silicon*, Mat. Res. Soc. Symp. Proc. **664**, A28.1.1 (2001).

6. R.L.C. Vink, G.T. Barkema, and W.F. van der Weg, *Raman spectra and structure of amorphous silicon*, Phys. Rev. B **63**, 115210 (2001).

7. R.L.C. Vink, G.T. Barkema, N. Mousseau, and W.F. van der Weg, *Fitting the Stillinger-Weber potential to amorphous silicon*, J. Non-Cryst. Solids **282**, 248 (2001).